

Joulean Heating and Lorentz Force Effects
on Gaseous Detonation Flow Fields

by

Edelbert G. Plett

B.A.Sc. University of British Columbia
(1962)

S.M. Massachusetts Institute of Technology
(1964)

Submitted in Partial Fulfillment
of the Requirements for the
Degree of Doctor of Science

at the

Massachusetts Institute of Technology

September, 1966

Signature of Author
Department of Mechanical Engineering
September 12, 1966

Certified by
Thesis Supervisor

Accepted by
Chairman, Departmental Committee on Graduate
Students

Joulean Heating and Lorentz Force Effects
on Gaseous Detonation Flow Fields

by

Edelbert G. Plett

Submitted to the Department of Mechanical Engineering on September 12, 1966 in partial fulfillment of the requirements for the degree of Doctor of Science.

ABSTRACT

The flow field of gaseous detonation waves is studied to determine how heat addition and momentum changes brought about by the application of electromagnetic fields will affect such properties as pressure, temperature and particle velocity. An analysis based on a one-dimensional nonsteady model for the flow field, coupled to a one-dimensional quasi-steady model for the wave front is presented. Results of numerical solutions, using electric field values and current distributions obtained from experimental measurements, for cases with electric fields only and for electric fields plus both positive and negative Lorentz forces are presented. Solutions simulating energy losses by assuming that the $\vec{E} \cdot \vec{j}$ enthalpy addition is just balanced by heat loss are also presented.

Quartz crystal pressure transducers were used in experiments to test theoretical predictions of pressure changes, and the wave speed was monitored to determine how it compared to theory. Pressure changes of as much as 20% were observed under the combined influence of Lorentz forces and electrical heating. These compared favorably with analytical solutions which allowed some heat loss to the wall. No change in wave speed was detected, which was also in agreement with theoretical predictions for these experiments.

Thesis Supervisor: T. Y. Toong

Title: Professor of Mechanical Engineering

To the Memory of My Father

John J. Plett

ACKNOWLEDGEMENTS

The author wishes to express his appreciation to his thesis supervisor, Professor T. Y. Toong, for the encouragement as well as the patient and critical appraisals with which he guided this work.

Professors J. A. Fay, J. R. Melcher and J. R. Kelly are responsible for many improvements in the quality of this work through their pointed and honest criticism, which has been appreciated by the author. Special thanks are due Jon Kelly for his help in this project even before he was a professor.

Professor Gerry Wilson has loaned several substantial pieces of electrical equipment as well as aided in the design of others used in the author's experiments, not to mention the frequent visits he made to diagnose and cure certain ailments of this equipment, all of which is very much appreciated by the author. Dr. Roger Lucheta deserves much credit for his contributions, especially in helping to get the computer program to work, and for later innovations which enabled extensive solutions to be obtained quite efficiently. Words of thanks go to Paul Wassmouth and his staff in the shop for their co-operation in making and repairing parts for experimental apparatus, as well as to Bob Silverstein and Steve Levin for their contributions in this area. Further thanks go to Bill Day for his help in reducing the data.

Out of school, the strength of character and words of encouragement of a young lady who will be identified here as simply Carolyn, did much to boost the author's moral.

Back in school, the author wishes to express his appreciation to Lotte, not only for typing this manuscript, which she so ably did, but also for adding some spirit to a group of sometimes too serious students.

The author wishes to thank the M.I.T. Computation Center programming and operating staff for their assistance in obtaining the numerical solutions described in this thesis. He acknowledges and appreciates the use of the facilities of the M.I.T. Computation Center, which includes the IBM 7094 computer, used for the numerical solutions.

This work was supported by the U.S. Army Research Office (Durham) AROD Project No. 3149-E, Grants DA-ARO(D)-31-124-G190 and DA-ARO(D)-31-124-G593 and the National Science Foundation Grant G-20880.

TABLE OF CONTENTS

	page
Abstract	ii
Dedication	iii
Acknowledgements	iv
Table of Contents	vi
List of Figures	viii
CHAPTER 1 Introduction	1
1.1 Physical Model	3
CHAPTER 2 Theoretical Analysis	8
2.1 Governing Equations	9
2.2 Wave Front Relations	9
2.3 Flow Field Relations	11
2.4 Physical Characteristics	13
2.5 State Characteristics	14
2.6 Solutions of the Equation	15
2.7 Numerical Solution Technique	16
2.8 Obtaining a General Point	17
2.9 The Wave Front	19
2.10 Rarefaction Wave	21
2.11 Order of Calculations	22
2.12 Grid Size	23
2.13 x-t Diagram	24
CHAPTER 3 Experimental Apparatus and Procedures	26
3.1 Experimental Apparatus	26
3.2 Test Section	27
3.3 Magnetic Field Supply	28
3.4 Electric Field Supply	28
3.5 Electric Current and Field Measurements	29
3.6 Pressure Measurements	30
3.7 Wave Speed Measurements	32
3.8 Seeding	33
3.9 Location of Observation Points	35
CHAPTER 4 Detonation Pressure, Electric Field and Conductivity Measurements	37
4.1 Wave Speed	37
4.2 Pressure Profiles	39

	page
4.3 Electric Fields	45
4.4 Electric Conductivity	47
CHAPTER 5 The Effect of Enthalpy Addition and Lorentz Forces on the Flow Field	53
5.1 Cases Studied	54
5.2 Trends of Theoretical Predictions	55
5.3 Detailed Results of Computations	63
5.4 Experimental Results	71
CHAPTER 6 Conclusions and Suggestions for Future Research	85
6.1 Conclusions	85
6.2 Suggestions for Future Research	90
APPENDIX 1 Sample Calculations	138
APPENDIX 2 Computer Program (Mad) Listings	142
APPENDIX 3 Experimental Procedures and Data Reduction	156
APPENDIX 4 Comparisons of Pressure Profile Measured in Experiments with Theory - No E-M Fields	163
APPENDIX 5 Tabulated Electric Field and Conductivity Distribution	168
APPENDIX 6 Electromagnetic Shock Interaction with Detonation Wave	169
APPENDIX 7 Energy Loss in the Plasma	179
REFERENCES	187
NOMENCLATURE	190
BIOGRAPHICAL SKETCH	193

LIST OF FIGURES

- Fig. 2-1 a,b,c,d Schematic Sketches
- Fig. 2-2 Wave Front Speed Change Calculated at 3 grid Sizes
- " 2-3 x-t Diagram for No E-M Fields
- " 3-1 Detonation Tube Schematic
- " 3-2 Test Section Schematic
- " 3-3 Magnetic Field Distribution (Experimental)
- " 3-4 Transducer Isolation Mount (Cut-Away View)
- " 4-1 Oscilloscope Traces for Electric Field Probe
- " 4-2 Typical Oscilloscope Traces for Pressure and Current Measurements
- " 4-3 p vs t Comparing Theory and Experiment for no Fields Applied
- " 4-4 Equal Potential Lines
- " 4-5 Electric Field in Gas as it varies with Time (1st Point)
- " 4-6 Electric Field in Gas as it Varies with Time (2nd Point)
- " 4-7 Electric Current vs Time to 1st Electrode
- " 4-8 Electrical Conductivity vs Time, case II
- " 5-1 p vs t, Case I, at sta (3) Theory and Experiment
- " 5-2 u and c vs t, Case I, sta (3), Theory
- " 5-3 p vs t, Case IV, sta (3), experiment
- " 5-4 p vs t, Case I, sta (4), Theory and Experiment
- " 5-5 u and c vs t, sta (4), Theory - Case I
- " 5-6 p vs t, Case IV, sta (4), Experiment
- " 5-7 p vs t, sta (1) Theory - Case VA, Experiment Case V
- " 5-8 u and c vs t, sta (1), Theory - Case VA

- Fig. 5-9 p vs t, sta (3), Theory - Case II and IIA
Experiment - Case II
- " 5-10 u and c vs t, sta (3) Theory for Case II and IIA
- " 5-11 p vs t, sta (3), Theory - Case VA, Experiment Case V
- " 5-12 u and c vs t, sta (3), Theory - Case VA
- " 5-13 p vs t, sta (4), Theory - Case II and IIA
Experiment - Case II
- " 5-14 u and c vs t, sta (4), Theory - Case II and IIA
- " 5-15 p vs t, sta (4), Theory Case VA, Experiment Case V
- " 5-16 u and c vs t, sta (4), Theory - Case VA
- " 5-17 p vs t, sta (3), Theory - Case III, IIIA,
Experiment Case III
- " 5-18 u and c vs t, sta (3) Theory - Case III, IIIA
- " 5-19 p vs t, sta (3), Theory - Case III, VIA
Experiment Case VI
- " 5-20 u and c vs t, sta (3), Theory Case III, VIA
- " 5-21 p vs t, sta (4), Theory - Case III, Experiment - Case III
- " 5-22 u and c vs t, sta (4), Theory - Case III
- " 5-23 p vs t, sta (4), Theory - Case III, Experiment Case VI
- " 5-24 x-t Diagram for Case I
- " 5-25 x-t Diagram for Case II
- " 5-26 x-t Diagram for Case III
- " A3-1 Maximum Deviation of Control Pressure from Averaged Control
- " A6-1 Schematic of Test Section Used to Generate Shock Waves
Behind Detonation Waves
- " A6-2 Locus of Shock Waves of Various Strength Overtaking a
C-J Detonation
- " A6-3 p vs t as Wave System Passes Transducer - Experimental
- " A6-4 Wave Front Velocity vs Position in Tube
- " A7-1 Boundary Layer in Tube

CHAPTER 1

INTRODUCTION

A detonation wave is a composite wave, made up of a compression and a combustion front. A centered rarefaction wave fans out behind the front whenever the wave motion is initiated at the closed end of a tube and is confined to one dimension thereafter. This combination produces an interesting problem in non-steady gasdynamics in the flow field, which can be further enhanced by the introduction of electro-magnetic effects. The author has composed a one-dimensional model to describe the flow field as it behaves under the influence of electric and magnetic fields and has experimentally observed pressure changes in the flow field which can be explained on the basis of this model.

The study of detonation phenomena in electromagnetic fields must be preceded by an understanding of some of its basic characteristics when these fields are absent. The early work of such men as Chapman, Jouguet, and Becker, using one-dimensional steady formulations to predict wave speed, and the later work of Zeldovich, Doring and von Neumann, who fit the composite wave model to the earlier successes in one-dimensional analysis, is presented by Lewis and von Elbe.¹ Discussion of the validity of the Chapman-Jouguet (hereafter referred to as C-J) criteria can be found in numerous research papers and texts.² Such phenomena as spin, detonation limits and turbulent reaction zones cannot be accounted for in a strictly one-dimensional analysis, but the 1-D analysis still provides a strong basic study from which departure to these other areas

can be made. Similar departures will be necessary for a full understanding of results presented in this thesis.

Using the 1-D steady model with a step change of electrical conductivity from zero to infinity at the wave front to represent a detonation wave in a magnetic field^{3, 4, 5, 6} has yielded some interesting solutions, but has not proved applicable to ordinary detonation phenomena. The parallel derivation for shock waves⁷ is verified in an electromagnetically driven shock tube⁸. It is possible that similar experiments in a combustible gas will characterize the frozen-flux solutions for detonations.

Using a quasi-steady, one dimensional analysis with typical values of flow variable variations through the reaction zone and reasonable values of electrical conductivity within the wave, Plett⁹ predicted very small effects on the wave speed. Kelly¹⁰ observed a reduction in wave speed (for currents ranging between 2 and 5 amps flowing in his tube) when the wave was acted upon by retarding Lorentz forces, and saw no effect for the opposite sense of magnetic field or when the current was outside this narrow range. He attributed the wave speed deficit to expected increases in the boundary layer thickness within the wave, an argument which is based on a departure from the usual 1-D model.

Having explored the possibilities of affecting the detonation front by electromagnetic means without considering its flow field, it is of further interest to examine the feasibility of changing the wave front through its flow field.

Although the hypothesis of Chapman (1899) and Jouguet (1905-6) has formed the basis of much study in explosives since their time, no one seems to have discussed the hydrodynamics of the burnt gas or the distribution of pressure behind the detonation front until the late 1940's.

Taylor¹¹ applies the progressive wave theory of Riemann to calculate pressure distributions behind plane and spherical detonation fronts. Kistiakowsky et al¹² obtained density profiles using X-ray absorption measurements in the flow field and compared their results with rarefaction wave theory. Their results show some scatter, but generally seem in better agreement with theory than the pressure measurements reported by Gordon¹³. The pressure measurements reported by Edwards et al¹⁴ are nearer to theoretical predictions than those reported by Gordon, for a tube larger in diameter than Gordon's, and farther from theory for a tube smaller in diameter. The implication that wall effects are the cause of the discrepancy will be discussed further in Chapter 4.

In addition to the hydrodynamic properties of the gaseous flow field, it is necessary to have information about its electrical properties in order to apply the model adopted by the author. Toong¹⁵ has contributed a thorough and critical review of the knowledge about ionization in detonations. The results reported by Basu and Fay,¹⁶ Basu,¹⁷ the more recent findings reported by Kelly¹⁰, and computations like those by Chinitz et al¹⁸ all indicate that it will be necessary to include seed material of low ionization potential in the gas mixture to increase its conductivity in order to allow electrical currents of several hundred amps to flow through the products. This last requirement is necessary before measureable effects can be expected on the basis of the model proposed by the author.

1.1 Physical Model

The model proposed is intended to include those aspects of the test apparatus which can be included within the framework of a one-dimensional

analysis. The wave, initiated at the closed end of a tube, is presumed to have reached the steady-state speed dictated by the C-J hypothesis before entering the test section. A rarefaction fan, consistent with the distance from the tube end wall, produces a non-steady flow field behind the wave front.

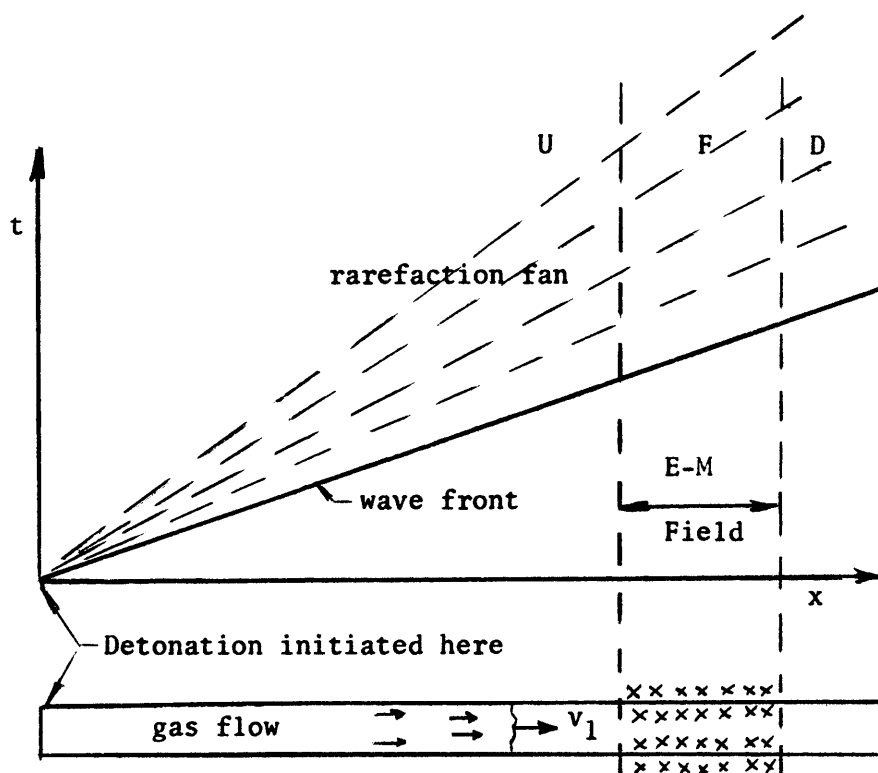


FIGURE 1-1 SCHEMATIC OF WAVE SYSTEM CONFINED TO ONE-DIMENSION IN THE TUBE

Fig. 1-1 illustrates the model. The wave front propagates down the tube, initiating gas flow everywhere in its wake. The rarefaction wave isentropically reduces the flow velocity, pressure, temperature and density behind the wave front.

Electric currents can flow through the gas in region F, but no electric currents flow in the region, U, upstream of the field or in the region D, downstream of the field. Magnetic fields are encountered only

in region F. When the detonation front reaches the test section, electric currents flow through the gas which is in the region F, between the electrodes, and behind the detonation front. When the detonation front leaves the field area, it no longer experiences effects of the field, but the gas which is in region F continues to be affected. Computations are carried out for regions U, F, and D to observe how the flow properties change as the wave system and gas motion it induces, enters and leaves the field region F.

The mathematical relations used to describe this situation are developed in Chapter 2. The wave front is treated as a discontinuity with known conditions upstream, the same chemical energy release per unit volume as though no electromagnetic fields were present, and conditions at the hot boundary specified by the flow field. This hot boundary has the conditions specified by the C-J hypothesis initially and is only disturbed from this steady-state by one of two conditions:

- 1) When a finite disturbance is created behind the wave so that it will propagate supersonically relative to the fluid, it has a chance of overtaking the wave. A few simplified calculations indicate that such a disturbance must be initiated very near the wave and also be of considerable strength in order to overtake the wave within a reasonably sized laboratory apparatus. (Appendix 6)

- 2) When energy is added to the gas in the flow field, the temperature will rise, and so small disturbances, now travelling at the new local sonic velocity, could overtake the wave front.

The method used in solving the system of equations was a linearized (with respect to wave motion) treatment in that all disturbances

propagated at the local sonic velocity relative to the fluid particle velocity. Thus the method effectively treats condition (1) above, the same as condition (2). For weak shocks, the errors introduced by linearization are very small. A shock wave of ten per cent pressure rise only travels about four per cent faster than a sound wave with correspondingly less difference for weaker shocks.¹⁹ The linearization method actually averages conditions before and after the pulse, so the error is even less than cited here.

The method of solution used by the author is a numerical technique programmed for the IBM 7094 computer. Approximate solution techniques^{20, 21} have been used to study effects on shock waves caused by changes in area in shock tubes. Rosciszewski et al²² have adapted such a technique to study the interaction of gasdynamic shocks with transverse electromagnetic fields. Their method is also valid only for small magnetic Reynolds numbers, (as is the method used by the author). Mirels et al²³ have applied an approximate method to study the problem of the flow of a piston-driven shock with and without magnetic interactions. The author has not attempted to compare his results with theirs as the flow field of a detonation is sufficiently different to render such a comparison of little value. The I characteristics in a shock-driven flow invariably intersect the wave front^{20, 21} and the type II characteristics bend forward rather than back as they do for a C-J detonation. Consequently, much of the intrigue in the problem posed by the author does not exist with shock waves as interactions of small disturbances with the front will take place even without applying electromagnetic fields. Since the type I characteristics behind a steady-state C-J detonation do not

terminate in the wave front, the same sized disturbance which can cause changes in a shock wave may never even reach the detonation front if it occurred in a detonation flow field. So the possibility of such an interaction in detonations must be established, and the conditions under which it will occur specified.

The theoretical development indicates that such interactions are possible but that little effect will be noted at the wave front for the conditions obtained in experiments by the author. The general trend of experimental results agrees with the trend predicted in theory with several distinct features of experiments establishing these trends. The predictions of the theoretical solutions are found to be in general agreement with experimental observations when appropriate allowance is granted for heat loss to the tube walls in the computations.

Experiments with electromagnetically produced shock waves in the flow field demonstrate that very large changes in pressure can be generated by this means. Large changes in detonation wave speed were obtained as a result of the interaction of these shock waves with the detonation wave front. (Appendix 6)

CHAPTER 2

THEORETICAL ANALYSIS

For the purpose of analysis, the problem can be divided into two parts, the wave front, and the flow field behind the wave front. The wave front will be treated as though it were momentarily in a steady state and one dimensional so that the steady-state 1-D, "jump relations" are applicable. The usual C-J criteria holds at the hot boundary only when the flow field is dominated by a rarefaction which will not allow small disturbances to overtake the wave and change these conditions. In the solutions obtained here, there are possible situations for which disturbances can reach the wave. When this happens, the hot boundary condition is modified by the disturbance. In this way, the wave speed can be affected by the flow field even when the "jump conditions" apply. These jump conditions will be unchanged as long as the changes to the hot boundary are slow compared with changes taking place across the wave.

The flow field will be treated as having changes in time and one dimension with uniform conditions in the other two dimensions. This condition of unidimensionality may be difficult to realize in practice, but the approximation can be used to good advantage. It will further be assumed that chemical reactions occur only in the wave front, with frozen conditions in the flow field. Heat transfer and friction will also be neglected in the derivation, but will be simulated by various solutions. The electrical conductivity is finite everywhere and zero ahead of the wave.

2.1 Governing Equations

The general equations appropriate to this formulation are the one-dimensional equations of change.

$$\frac{\partial \rho}{\partial t} + \frac{\partial}{\partial x}(\rho u) = - \frac{\rho u}{A_c} \frac{\partial A_c}{\partial x} \quad (2.1)$$

$$\rho \frac{\partial u}{\partial t} + \rho u \frac{\partial u}{\partial x} + \frac{\partial p}{\partial x} = \bar{j} \times \bar{B} - F\rho \quad (2.2)$$

$$\rho \frac{\partial}{\partial t} \left(C_p T + \frac{u^2}{2} \right) + \rho u \frac{\partial}{\partial x} \left(C_p T + \frac{u^2}{2} \right) - \frac{\partial p}{\partial t} = \bar{j} \cdot \bar{E} + \rho \dot{q}_{\text{chem}} \quad (2.3)$$

$$p = \rho RT \quad (2.4)$$

In the reduction which follows, it is assumed that the specific heat, C_p , is a constant and that the ratio of specific heats, $C_p/C_v = k$, is also a constant. It is also assumed that the electric field is only in the y direction, the magnetic field only in the z direction, and the velocity field only in the x direction (Fig. 2-1a).

The generalized Ohm's Law for this system is

$$j = \sigma(E - uB) \quad (2.5)$$

2.2 Wave Front Relations

For a wave of finite thickness, it can be shown⁹ that for a finite electrical conductivity there will be a small contribution made by the electromagnetic terms. To determine this contribution, further assumptions must be made about the structure of the wave, all of which becomes very uncertain and involved. It was demonstrated⁹ that this contribution is

negligibly small for the range of conditions which would be obtained in the experiments of interest to the author. Taking all these factors into account then, the non-steady terms drop out of equations (2.1) through (2.3) as do the electromagnetic terms. It will further be considered to be in a constant area channel where wall friction and heat transfer are unimportant. Heat loss can easily be introduced in a qualitative way as will be seen later. Eq. (2.1) through (2.3) become then, when integrated across the discontinuity

$$\rho_1 V_1 = \rho_2 V_2 \quad (2.6)$$

$$\rho_1 V_1^2 + p_1 = \rho_2 V_2^2 + p_2 \quad (2.7)$$

$$C_p T_1 + \frac{V_1^2}{2} + Q = C_p T_2 + \frac{V_2^2}{2} \quad (2.8)$$

These can then be reduced to the jump relations

$$\frac{p_2}{p_1} = \frac{1 + kM_1^2}{1 + kM_2^2} \quad (2.9)$$

$$\left(\frac{T_2}{T_1} \right) = \left(\frac{1 + kM_1^2}{1 + kM_2^2} \frac{M_2}{M_1} \right)^2 \quad (2.10)$$

$$\left(\frac{M_2}{M_1} \frac{1 + kM_1^2}{1 + kM_2^2} \right)^2 \left(1 + \frac{k-1}{2} M_2^2 \right) = 1 + \frac{k-1}{2} M_1^2 + \frac{Q}{C_p T_1} \quad (2.11)$$

Where use is made of the equation of state (2.4) the definition of k and the relation

$$M_{(1),(2)} = \frac{V_{(1),(2)}}{\sqrt{kRT_{(1),(2)}}} \quad (2.12)$$

Discussion of how the solution is carried out in conjunction with the flow field will be reserved until the equations of change in the flow field are derived.

2.3 Flow Field Relations

The derivation of these relations is done in ref. 9 but will be included here for the sake of completeness.

Putting (2.4) into (2.3) and using (2.5) yields

$$\left(\rho \frac{\partial}{\partial t} + \rho u \frac{\partial}{\partial x}\right) \left(\frac{k}{k-1} \frac{p}{\rho} + \frac{u^2}{2}\right) - \frac{\partial p}{\partial t} = \sigma E(E-uB)$$

when only electrical energy addition is considered. Expanding the left side, grouping terms and using the relation $c^2 = kp/\rho$, results in

$$\frac{1}{k-1} \frac{\partial p}{\partial t} + \frac{uk}{k-1} \frac{\partial p}{\partial x} - \frac{c^2}{k-1} \left(\frac{\partial \rho}{\partial t} + u \frac{\partial \rho}{\partial x}\right) + u \left(\rho \frac{\partial u}{\partial t} + \rho u \frac{\partial u}{\partial x}\right) = \sigma E(E-uB) \quad (2.13)$$

Making use of equation (2.2) converts this equation to the form

$$\frac{\partial p}{\partial t} + u \frac{\partial p}{\partial x} - c^2 \left(\frac{\partial \rho}{\partial t} + u \frac{\partial \rho}{\partial x}\right) = \sigma(E-uB)^2 (k-1) \quad (2.14)$$

All the gas properties (i.e., u , p , ρ) must vary continuously with x and t giving three additional relations, the six basic relations being written, (in the absence of area change, heat transfer or friction)

$$dx \frac{\partial u}{\partial x} + dt \frac{\partial u}{\partial t} = du$$

$$dx \frac{\partial p}{\partial x} + dt \frac{\partial p}{\partial t} = dp$$

$$dx \frac{\partial \rho}{\partial x} + dt \frac{\partial \rho}{\partial t} = d\rho$$

$$\rho \frac{\partial u}{\partial x} + u \frac{\partial \rho}{\partial x} + \frac{\partial \rho}{\partial t} = 0$$

$$u \frac{\partial u}{\partial x} + \frac{\partial u}{\partial t} + \frac{1}{\rho} \frac{\partial p}{\partial x} = \frac{cB}{\rho} (E-uB)$$

$$u \frac{\partial p}{\partial x} + \frac{\partial p}{\partial t} - uc \frac{2\partial \rho}{\partial x} - c^2 \frac{2\partial \rho}{\partial t} = (k-1) \sigma (E-uB)^2$$

These equations are now in the form used by Shapiro¹⁹. The method of characteristic curves can now be applied to study the behavior of the solutions. Solving for $\partial u/\partial x$ in determinant notation

$$\frac{\partial u}{\partial x} = \frac{\begin{array}{cccccc} du & dt & 0 & 0 & 0 & 0 \\ dp & 0 & dx & dt & 0 & 0 \\ d\rho & 0 & 0 & 0 & dx & dt \\ 0 & 0 & 0 & 0 & u & 1 \\ \frac{\sigma B}{\rho} (E-uB) & 1 & 1/\rho & 0 & 0 & 0 \\ (k-1) \sigma (E-uB)^2 & 0 & u & 1 & -uc^2 & -c^2 \end{array}}{\begin{array}{cccccc} dx & dt & 0 & 0 & 0 & 0 \\ 0 & 0 & dx & dt & 0 & 0 \\ 0 & 0 & 0 & 0 & dx & dt \\ \rho & 0 & 0 & 0 & u & 1 \\ u & 1 & 1/\rho & 0 & 0 & 0 \\ 0 & 0 & u & 1 & -uc^2 & -c^2 \end{array}} \quad (2.15)$$

2.4 Physical Characteristics

The condition that $\partial u/\partial x$ be indeterminate is that the denominator of equation (2.15) be equal to zero. Since $\partial u/\partial x$ is in general finite, it is necessary that the numerator also be equal to zero. By setting the two determinants of equation (2.15) equal to zero, the differential equation of the characteristic curves is obtained.

Setting the denominator equal to zero, and simplifying yields the roots

$$\left(\frac{dx}{dt}\right)_{I,II} = u \pm c \quad (\text{Mach Lines}) \quad (2.16)$$

$$\left(\frac{dx}{dt}\right) = u \quad (\text{Path Lines}) \quad (2.17)$$

Equation 2.16 signifies that discontinuities in the derivatives may occur on lines which travel either rightward or leftward with the local speed of sound relative to the fluid. This is the same as saying that the disturbances are propagated on such lines.

Equation 2.17 indicates that the trajectories of the fluid particles themselves may be the loci of discontinuities. Physically, this means that the fluid particles can behave individually in a nonsteady motion so that the path lines are characteristic curves on which the entropy or temperature gradients may have discontinuities.

It may be of interest to note that the equations of the characteristic curves are identical to those found in ordinary gas dynamics, with no new terms introduced by the electro-magnetic field. The reason for this follows from the method of setting up the governing equations. Implicit in the reduction of the governing equations is the assumption that \bar{B} is

a fixed, constant quantity. This allows the magnetic field to affect the fluid dynamic problem as here developed, but does not allow the fluid to affect the magnetic field. Thus no electromagnetic, or hydromagnetic wave phenomena are considered. This assumption is valid as long as the Magnetic Reynolds number, $R_m = \mu_0 \sigma L u$ is much less than 1, so that the velocity field and magnetic field are not strongly coupled. In experiments and solutions considered here, R_m is typically of order 10^{-2} . (Appendix 1).

2.5 State Characteristics

Setting the numerator of equation 2.15 equal to zero, expanding the determinant and eliminating dx by means of equation 2.16, the following differential equation of the Mach lines in terms of the state coordinates p and u is obtained

$$(du)_{I, II} = - \frac{(dp)_{I, II}}{\rho c} + \frac{M}{\rho c} (dt)_{I, II} + N(dt)_{I, II} \quad (2.18)$$

where $M = (k-1)\sigma(E-uB)^2$

$$N = \frac{\sigma B}{\rho} (E-uB)$$

Solving for $\frac{\partial p}{\partial x}$ in the same way, and eliminating dx by means of equation 2.17 yields

$$(dp)_{\text{path}} = \frac{2}{k-1} \frac{p}{c} (dc)_{\text{path}} - \frac{M}{k-1} (dt)_{\text{path}} \quad (2.19)$$

This result can also be obtained another way as derived by Shapiro¹⁹ and Plett⁹.

Using equation 2.19 as well as the additional two relations

$$\left(\frac{dp}{dt}\right)_{I, II} = \left(\frac{dp}{dt}\right)_{\text{path}} + c \frac{\partial p}{\partial x}$$

$$\left(\frac{dc}{dt}\right)_{I, II} = \left(\frac{dc}{dt}\right)_{\text{path}} + c \frac{\partial c}{\partial x}$$

it can be shown that

$$\left(\frac{dp}{dt}\right)_{I, II} = \frac{2k}{k-1} \frac{p}{c} \left(\frac{dc}{dt}\right)_{I, II} + pc \frac{\partial}{\partial x} \left(\ln \frac{c^{\frac{2k}{k-1}}}{p}\right) - \frac{M}{k-1} \quad (2.20)$$

Insertion of equation 2.20 into 2.18, after simplification, yields

$$\left(\frac{du}{dt}\right)_{I, II} = + \frac{2}{k-1} (dc)_{I, II} + \left[\frac{c^2}{k} \frac{\partial}{\partial x} \left(\ln \frac{c^{\frac{2k}{k-1}}}{p}\right) + \frac{kEN}{Bc} + N \left(1 + \frac{ku}{c}\right) \right] (dt)_{I, II} \quad (2.21)$$

For computation sake, it is convenient to expand the first term in the bracket, so that

$$\frac{c^2}{k} \frac{\partial}{\partial x} \left(\ln \frac{c^{\frac{2k}{k-1}}}{p}\right) = \frac{2c}{k-1} \frac{\partial c}{\partial x} - \frac{c^2}{kp} \frac{\partial p}{\partial x} \quad (2.22)$$

2.6 Solution of the Equations

Since the equation to be solved (2.21) contains terms which depend upon t and x as well as c and u , it is not possible to integrate the state characteristics in general form. Instead, the net of state characteristics is different for each physical problem, and it must be constructed simultaneously with the physical Mach net by means of a stepwise iterative procedure. At the same time that the physical and state characteristics

nets are under construction, it is necessary to integrate equation 2.19 stepwise along the path lines. This not only provides useful information concerning the pressure at each value of x and t but also leads to the determination of equation 2.22 which is necessary for the solution of 2.21.

In addition, this nonsteady solution must be matched with the quasi-steady solution of the jump conditions at the wave front.

Solutions for a limited number of points by a semi-graphical technique were obtained in ref. 9. The solutions to be reported here are the result of a more refined numerical technique, capable of handling a wide variety of initial conditions which was tested and improved over a period of time. In addition the wave front is allowed to have modified conditions as the solution dictates and solutions are obtained for a large flow field behind the wave front.

2.7 Numerical Solution Technique

The numerical technique used is basically a method of solving algebraic equations simultaneously to obtain intersections of lines as opposed to the semigraphical technique of laying out the lines on a graph to determine intersection points. The semigraphical procedure is useful for preliminary results, as it gives the investigator insight into trends of the solution quickly. The numerical technique, programmed for a computer, is the practical way of obtaining detailed, extensive solutions of greater accuracy than is possible by graphic technique. Appendix 2 is the printout of the MAD program used to obtain the solutions on the computer. A description of the solution of a general point in the flow field will be followed by a description of how the solution was begun.

2.8 Obtaining a General Point

The basic step in the solution is to determine properties at a point in the $x-t$ plane given the properties at two other points along the I and II characteristics, and given enough information to calculate the properties at some point on the path line as well as the changes along these characteristic directions.

The general case is illustrated in Fig. 2-1b. Given the location and properties at points A, B, C and D, to find the location of, and properties at point F. The lines BF and DF are straight lines. Consequently the solution of two simultaneous, linear equations in two variables along these lines yields the solution at F. Since the location of F determines the change in properties from B and D to F, and these resultant properties at F in turn help determine its location, it is necessary to use an iteration scheme to solve for both the properties and the location of the new point.

Equation 2.21 can be written in finite difference form, which for the I characteristic becomes

$$(\Delta u)_I = -\frac{2}{k-1} (\Delta c)_I + (\Delta u_{EM})_I \quad (2.23)$$

where $(\Delta u_{EM})_I$ represents the change in particle velocity and sound speed along the I characteristic due to electric and magnetic fields.

Expanding 2.23,

$$u_F - u_B = -\left(\frac{2}{k-1}\right) (c_F - c_B) + (\Delta u_{EM})_I \quad (2.24)$$

Writing the corresponding equation for DF and solving for the unknowns results in,

$$c_F = \frac{c_B + c_D}{2} + \frac{k-1}{4} [(u_B + (\Delta u_{EM})_I) - (u_D + (\Delta u_{EM})_{II})] \quad (2.25)$$

$$u_F = \frac{c_B - c_D}{k-1} + \frac{1}{2} [u_B + (\Delta u_{EM})_I + u_D + (\Delta u_{EM})_{II}] \quad (2.26)$$

A first approximation to c_F and u_F is obtained by setting Δu_{EM} equal to zero. Now with this approximation of c_F and u_F , it is possible to get the x and t location of F .

$$x_F = \left[\frac{x_B}{(u+c)_{BF}} - \frac{x_D}{(u-c)_{DF}} + t_D - t_B \right] \left(\frac{1}{\frac{1}{(u+c)_{BF}} - \frac{1}{(u-c)_{DF}}} \right) \quad (2.27)$$

where $(u+c)_{BF}$ is the average $(u+c)$ between B and F , and

$(u-c)_{DF}$ is the average $(u-c)$ between D and F .

Then,

$$t_F = (x_D - t_D(u-c)_{DF} - x_B + t_B(u+c)_{BF}) \left(\frac{1}{(u+c)_{BF} - (u-c)_{DF}} \right) \quad (2.28)$$

Next, the pressure at point F is determined. To determine p_F it is necessary to integrate equation 2.19 along the path line and to do this, properties at another point on the path line are required. To obtain these, the path line is projected back from point F until it intersects either line AB or AD at PP . The properties at PP are determined by linear interpolation between A and B if it falls on AB or between A and D if it falls on AD . In order to obtain the intersection point, PP , accurately, it is necessary to use an average velocity between PP and F which can only be obtained by iterative procedures. When this iteration has converged and the properties at PP are known, the pressure at F can be determined by the relations

$$\Delta_p = \frac{2k}{k-1} \left(\frac{p}{c}\right)_{PP-F} (c_F - c_{PP}) - \sigma(E-uB)^2 (t_F - t_{PP}) \quad (2.29)$$

$$p_F = p_{PP} + \Delta_p$$

where quantities in equation 2.29 are averages between PP and F. Since p appears in the calculation of Δ_p , it is again necessary to use an iteration loop to calculate an accurate value of p_F .

Now that the pressure at point F has been determined, the pressure gradients can be determined. These are needed to evaluate the first term in the bracket of equation 2.21. The gradients of p and c are evaluated along lines of constant time which necessitates more interpolation but no iteration loops. The other terms in the bracket of equation 2.21 can also be determined for mean values of the variables along lines BF and DF. Combining these terms, the first approximation to (Δu_{EM}) is obtained along the I and II characteristics.

Now using these values of $(\Delta u_{EM})_{I, II}$, we return to equation 2.25 and go through the entire procedure again. This is repeated until satisfactory convergence is obtained. These final values of u , c , x , t , p are the ones assigned to F and stored for subsequent calculations.

2.9 The Wave Front

Since the flow field behind the detonation wave was created by the wave, and any small modification of the character of the wave front will strongly modify the flow field, it is important to treat the analysis at the front correctly. Some assumptions are necessary to render the problem solvable, however, and the following procedure was used.

The first assumption was that the wave is thin so that any contribution by electromagnetic action in the direction of the type II characteristic or along the path line through the reaction zone is neglected. The type I characteristic lies parallel to the wave front at the hot boundary, so it is conceivable that the flow could be modified there by the electromagnetic fields. Since it was assumed that the chemical energy contribution is unaffected by the fields, the only tie between the flow field and the wave front is along the I characteristic.

The usual jump conditions, equations 2.9, 2.10, and 2.11 apply here. Rather than setting the hot boundary at the C-J condition, this point is allowed to be determined by the changes brought about along the I characteristic, the only restriction being that M_2 cannot be greater than 1, since the author disallows weak detonations².

The solution begins well upstream of the electromagnetic field, so a well established flow field is present, prior to disturbances changing conditions.

To determine the new, hot boundary conditions, equation 2.24 can be rewritten for the new situation.

$$c_H = c_A + \frac{k-1}{2} ((\Delta u)_I - (u_H - u_A)) \quad (2.31)$$

Fig. 2-1c here assumes the wave is already overdriven, otherwise points A and B would coincide. The first approximation to the point H in the x-t plane is obtained by projecting the wave speed from the last calculated point on the wave front, point B in Fig. 2-1c. Using this information, $(\Delta u)_I$ is obtained. The first approximation to u_H is taken as the value it had at B, and now a value of c_H is obtained. With this,

a new value of M_2 at H is obtained, and used in equation 2.11 to obtain a value for M_1 . This allows a new value of u_H to be calculated by writing

$$u_H = V_1 - c_H \cdot M_2 \quad (2.32)$$

where V_1 is the wave front velocity corresponding to the new value of M_1 . Now using this value of u_H and a better value for $(\Delta u)_I$ based on the new location and properties at H, returning to equation 2.31, a new value for c_H is obtained. This loop is continued until satisfactory convergence is obtained.

2.10 Rarefaction Wave

To bring the theoretical development a step nearer to the experimental observations, it is expedient to introduce a rarefaction wave in the flow field since such a phenomena occurs in experiments to which it will be compared. Taylor¹¹ has derived the relations which describe the rarefaction wave and are easily modified to suit the purpose here.

For a plane detonation, Taylor shows that the particle velocity decreases linearly behind the wave front for an isentropic expansion. This can be written as

$$\frac{u}{u_2} = 2.22 \frac{r}{R_c} - 1.22 \quad (2.33)$$

where u is the particle velocity at a point $\frac{r}{R_c}$ from the detonation front. (See Fig. 2-1d)

For an observer at a point in the tube, as the wave passes, the position r remains fixed, but the reference distance R_c changes. To this observer, the velocity changes as

$$\frac{u}{u_2} = (2.22 R_0) / (R_0 + V_{\text{NOT}} \cdot t) - 1.22 \quad (2.34)$$

where R_0 = distance from detonation ignition

V_{NOT} = Wave front speed

u_2 = particle velocity at hot boundary of wave

t = time after wave passes observer

Since the expansion is isentropic, it follows that

$$p = p_2 \left(1 - \frac{k-1}{2c_2} (u_2 - u) \right)^{\frac{2k}{k-1}} \quad (2.35)$$

$$c = c_2 - \left(\frac{k-1}{2} \right) (u_2 - u) \quad (2.36)$$

2.11 Order of Calculations

The unit operations used in the calculation of the flow field have now been described. The computer printout shows how it is all made to work together. In brief, the procedure is thus.

The appropriate data is read into storage and the conditions at the hot boundary calculated. Since the initial point is well upstream of the electromagnetic field region, the condition of the gas along the II characteristic originating here can be specified using the rarefaction wave results. This part is done in the main part of the program.

When the first column (the type II characteristics are referred to as columns) has been calculated, the next point on the detonation wave front is calculated. The program then switches to the subroutine PROVA, which proceeds with calculations of the next column. It in turn calls on GTPRK to calculate the pressure at the new point, and GTUSR to

calculate the gradients in the flow field. When this column is completed, it returns to the main program where the next point on the wave front is obtained, and the cycle goes on.

The electromagnetic field introduces changes only over a specified range. Disturbances caused by the field can be propagated to points outside the field however, along the characteristic directions.

2.12 Grid Size

Before results of a numerical solution using a "grid" of arbitrary size are acceptable, it is necessary to determine how the grid size has affected the solution. If increasing or decreasing the grid size by a factor of four does not substantially alter the solution, the grid size is adequate.

Early returns from the computer showed that the region where grid size had the greatest influence on the solution was at the wave front. The most critical evaluation comes from examining the solution at the wave front for affects of grid size. Fig. 2-2 is a plot showing wave front speed as it changes through the 1 meter long test section as calculated by three grid sizes, keeping all other parameters the same. The grid shape used was an approximate parallelogram such that at the beginning of the solution, the path line was approximately the one diagonal. This shape would become somewhat distorted during the course of a solution, but it was, in this sense, approximately equal sided to start with. By doubling the grid size, both sides would be doubled so the area would be increased by about four times. The "grid area" noted on Fig. 2-2, is simply the product of the projected x-direction length multiplied by the projected length of the other side on the t-axis, and is not the

exact area of the grid. The three sizes used are noted on the figure. The agreement is seen to be very good as there is no divergence anywhere, but instead, the agreement gets better as the solution progresses. Slight discrepancies arise between the solutions but the method appears to be self-compensating so errors do not accumulate. The agreement at the wave front is indicative of the accuracy of the values of other properties, i.e., u , c , p , since these are determined by the wave speed or help determine the wave speed. The solutions reported in Chapter 5 are all obtained using the middle grid size tested here.

2.13 x - t Diagram

Fig. 2-3 shows a plot of the detonation wave and its flow field on the $x-t$ plane. Both types of characteristics are sketched in for the control solution, with a path line also shown to give its approximate direction. Close examination reveals the curvature of the type II characteristics and the fan-like expansion of the type I characteristics due to the rarefaction wave.

The grid area shown here is 64 times as large as that actually used in computations as only every eighth row and every eighth column was plotted here.

Following the type II characteristics, along which disturbances propagate, will give insight to the reader as to how field effects can change conditions at sta (1) and how downstream effects will influence conditions at sta (3) after a time.

This evenly spaced grid becomes distorted by electromagnetic interactions. Rarefactions generally cause the characteristics to spread

further apart while compressions have the opposite effect. A decrease in particle velocity, u , and an increase in sound speed, c , causes the type II characteristic to bend backward more and vice versa. An increase in both u and c causes the type I characteristic to bend toward the wave, a decrease in both bends it away. Intermediate effects depend on the relative magnitudes in changes to u and c .

CHAPTER 3

EXPERIMENTAL APPARATUS AND PROCEDURES

3.1 Experimental Apparatus

A schematic diagram of the main parts of the experimental apparatus is shown in Fig. 3-1 and 3-2. A horizontal rotating steel cylinder with a steel pipe inside provides the necessary agitation to insure mixing of the combustible gases before admitting them to the shock tube. The gases are admitted to the mixing tank in the proper proportions by using a manometer and the method of partial pressures.

The tube consists of 2" square, 85-15 brass tubing with stainless steel flanges and O-ring seals. A driver section which can be isolated with a diaphragm is provided, but is not used as such in the experiments. Ignition of the combustible mixture is accomplished by discharging a $1/4 \mu\text{f}$ capacitor, charged to 5000 volts, across a spark gap at the end wall of the tube. Since there was some speculation that a large discharge could produce overdriven waves, a porous diaphragm was placed at the end of the driver section. This diaphragm had eight, $1/8$ " dia. holes equally spaced on a 1" dia. circle, allowing the flame to pass through and initiate a new detonation, and so eliminating any possibility of an overdriven wave downstream. No significant difference was noted in the pressure history downstream as a result of this addition, but it was left in, nevertheless, to suppress any speculation that the wave may be overdriven initially.

A provision was added to allow continuous purging, or through-flow, while the experiment was being performed. With just a simple connection through a metering valve between the tube and mixing tank, ignition of the gas in the tube would cause a flash-back and explosion of the remaining mix in the mixing tank, if the metering valve were the least bit open. Since this is both wasteful of mixture and potentially dangerous, a quenching filter was put in the line between the mixing tank and shock tube. This consisted of a 1 ft. length of 1/2" copper tubing, tightly packed with steel wool. This allowed the high pressure gas from the mixing tank to seep into the tube, but quenched any flashback, thus safeguarding the mixing tank. A similar filter, less tightly packed, was inserted between the tube and vacuum pump to safeguard the pump. A by-pass line to the pump was added to permit the tube to be evacuated to lower pressures between runs. This by-pass was then clamped off and the pressure stabilized at the desired test pressure while continuously purging, prior to igniting the mixture for the experiment. A liquid nitrogen cold trap cooled the gas before entering the pump.

3.2 Test Section

The test section consists of four equi-length sections for a total of 2 meters. Each section has a 3/8" thick brass electrode, extending across the entire width of the tube on the top and bottom, with windows fitted, one on either side, held in by screws and sealed with O-rings. The sections are connected by a phenolic divider which insulates each electrode section from the adjacent one. The two end sections have an additional division in the electrode, to allow visual or optical observations of the behavior of the wave as it first enters or when it leaves the electric field.

The two center sections, which were used as the electric and magnetic field region, were fitted with plexiglass windows. It was found advantageous to have metal windows in which to mount the pressure transducers as they were more rigid, therefore transmitting less vibration to the transducer. Consequently the two end sections were fitted with aluminum windows on one side for this purpose. The windows are all of identical size so that they could be interchanged.

3.3 Magnetic Field Supply

The pulsed magnetic field is provided by a 1 meter long, saddle-wound coil, of No. 8 square copper wire. Power is supplied by discharging a 740 μf capacitor bank through the coil. The power supply is triggered when the wave passes an ionization gap upstream of the test section, and "crowbars" when the current begins to reverse in the coil, preventing a ringing in the coil. The basic unit is described by Wilson²⁴ with a modified crowbarring circuit described by Thomas²⁵.

The resulting distribution of magnetic field strength along the axis of the test-section and in time are shown in Fig. 3-3.

3.4 Electric Field Supply

For the proposed experiments, the electric field supply was required to supply current of the order of a thousand amps for a duration of up to 600-800 μsec , and not start at such a high voltage that breakdown ahead of the wave or arcing behind the wave would result. These requirements are met by a large capacitor bank with small load impedance to control the energy release while not dissipating too much energy in itself. Each of the

two electrodes in the field region was energized separately. Fig. 3-2 shows schematically how this was done, listing the values used for capacitors, inductors and resistors.

3.5 Electric Current and Field Measurements

The electric current flowing to each electrode was measured using a Rogowski coil plus an integrator. Silverstein²⁶ describes the construction and calibration of one of these coil-integrator combinations. A similar one was used for the second electrode. This method of measuring current proved far superior to measuring the voltage drop across a known resistor since floating potentials inherent in the latter technique soon become a problem when large currents are being drawn.

The author was not satisfied with using the voltage drop between the electrodes as a measure of the electric field in the gas. Consequently, a simple means of measuring potentials at intermediate points was devised. The insert of Fig. 3-2 shows a schematic of the circuitry used.

Small wires were made to pass through the plexiglass window of the test section in vertical rows at three points along the electrode. The wires protruded into the test section approximately 1/8 inch at spacings of 0.1, 0.5, 1.0, 1.5 and 1.9 inches from the cathode, which was separated from the anode by 2 inches.

A battery was used to float the wires at a potential above ground, equal to the battery potential. Large resistors were used to limit currents to micro-amps, and a tap was taken off each resistor and its voltage displayed on the oscilloscope.

Consider a single wire, for simplicity, used in this manner. When

the conducting slug passes, if the potential in the plasma in the vicinity of the probe is lower than the battery voltage, current will flow from the probe into the gas and a negative voltage is displayed on the scope. When the plasma potential is higher than the battery voltage, current flows from the plasma into the probe and a positive deflection is observed. When the two are at equal potentials, no current flows and there is zero deflection on the scope. (In actual fact, zero current corresponds to a probe potential of about 0.3 volt or less below plasma potential due to the electron space charge for the typical conditions in these experiments. See Appendix 1²⁷) If the gas conductivity is zero, the current also would be zero, but when the trace crosses distinctly from positive to negative deflections, the cross-over point corresponds to the point where probe and plasma were at equal potential. An asymptotic approach to zero was interpreted as resulting from the conductivity gradually reducing.

Plotting the points where the various probe traces crossed zero at a given battery voltage yielded an equal potential line. By changing the battery voltage for identical runs, different potential lines were obtained and the potential map was plotted. Identical battery voltage and identical detonation, electric-field and magnetic-field conditions yielded good reproducibility in mapping the potentials. The current drawn by each probe was micro amps compared to hundreds of amps flowing into the electrodes so the distortion of the electric field by these probes would be negligible.

3.6 Pressure Measurements

The pressure pickups were two nominally-identical Kistler 603A, non-magnetic, acceleration compensated quartz crystal transducers. The charge

amplifiers were model 565, also by Kistler to correspond with the transducers. The ringing frequency of the first was between 160 and 200 Kc, while the second one was around 500 Kc. A 100 Kc low pass filter was used on the output of the charge amplifier to eliminate this high frequency ring, leaving a relatively clean signal.

Several problems were encountered in the use of the pressure pickup. Measurements first made with the transducer securely mounted in the tube wall had a curious sinusoid superposed on a signal which resembled the expected pressure history. This sinusoidal signal was identified with the ringing frequency of the window, and was obtained even when the transducer was mounted on the outside of the window, not in contact with the gas, since it was caused by the acceleration of the window and hence the transducer mount. Increasing the effective mass of the window improved conditions somewhat but did not solve the problem. The acceleration effect was eventually reduced to a negligible amount by mounting the transducer in a separate piece of metal and connecting this assembly to the tube wall by a flexible diaphragm. A cut-away schematic of the mount is shown in Fig. 3-4. The one disadvantage of such a mount is that it is difficult to keep the transducer face flush with the inside wall of the tube. In most cases, the transducer was slightly recessed in the wall, which may account for part of the sudden drop in pressure after the wave front passed. This will be discussed in a later section.

Another major difficulty experienced was due to the temperature sensitivity of the transducer. Stresses set up in the diaphragm caused a negative deflection when the temperature was suddenly raised. This effect was nullified by coating the transducer with an ablative covering.²⁸

General Electric RTV 580 applied over a primer coat of GE, SS-4004 was found to shield the transducer adequately. This coating also provided an electrically insulating shield which allowed the transducer to be mounted inside the electric field without being bothered by stray currents seeking ground through the transducer mount, thus putting extra noise and distortion on the signal.

Calibration was accomplished while the transducer was mounted in the tube. The tube was evacuated to some known vacuum, and the pump line clamped. The output of the charge amplifier, set on long-time-constant, was displayed on the oscilloscope, now set on a slow sweep rate. The line was disconnected from the pump, the shutter on the scope camera opened and after triggering the scope, the clamp was removed from the line to allow air to rush into the tube. The pressure rise took approximately 1/2 second, which is slow by shock-tube time scales but comparable to other methods of static calibration. A good check would have been to calibrate it with shock waves of known strength but since the detonation tube was not suited to producing shock waves, this check was never made.

The charge amplifier's amplification was checked separately from time to time. A square wave from the scope was fed into the cal. input side and the output waveform monitored. It is noteworthy that the output waveform had a very clean amplified square wave reproduction of the input signal when no filter was on the output. A maximum overshoot of about 4-5% was seen when the filter was added.

3.7 Wave Speed Measurements

The detonation wave speed, although measurable by many techniques under ordinary conditions, is not easily measured when the experiment

includes passing large electric currents through the product gas. Kelly¹⁰ used the Knight and Duff²⁹ circuit with ionization gages and obtained good accuracy, although he did experience some noise on his signals from the currents in the gas. The experiments done here involve currents several orders of magnitude larger, so the noise obliterates the desired signal. Attempts to raise the signal level to overcome this difficulty led to other related difficulties, but no solution.

Various optical techniques failed due to the intense light emitted when large currents flow in the product gases. Perhaps good measurements could be obtained by streak photography.

Since pressure changes would reflect small changes in the flow field much more emphatically than would the wave speed changes, it was decided to concentrate on making careful pressure measurements and merely monitor the wave speed to note if it was approximately consistent with expectations. This monitoring was accomplished by feeding the signals from both pressure transducers, spaced by a known distance along the tube, into a single beam on the oscilloscope. The resulting trace had two sharp rises, separated by the time interval that it took the wave front to pass between the two transducers. Deviations of less than 3% could not be reliably detected by this means, but it served as a check for larger changes.

3.8 Seeding

The electrical conductivity of a clean detonation wave and its products is not high enough to observe the effects sought by the author^{10,14}. Attempts to break down the gas and produce large electron concentrations

were successful to a degree but results were generally difficult to reproduce and currents did not appear to be distributed over the flow field with any degree of homogeneity so that attempts to relate results to the theory described in Chapter 2 seemed futile. One interesting experiment was accomplished this way however and is reported in Appendix 6.

A desirable solution to this situation would be one allowing some control on the conductivity while increasing it by several order of magnitude. Some controlled method of seeding appeared to be the answer.

Basu¹⁷ had accomplished this in detonation waves by sprinkling alkali salt into a vertical tube at the proper instant before firing the mixture. The results seemed reasonably well controlled, but the thought of constructing a vertical tube was not a pleasant one. Louis³⁰ reported method of seeding with cesium vapor in a horizontal tube seemed very attractive, but his method had been tried only in shock waves with argon. Using the cesium vapor in oxygen may result in oxides forming which result in larger particles which would settle faster resulting in poorer performance. This technique warrants further development but in this program the author did not want to undertake such a task if not necessary.

Toong³¹ suggested sprinkling a little alkali salt in the tube to see if this could produce the desired effect. Reagent quality KCl powder was sprinkled in the tube with a modified vegetable duster. The particles of KCl varied in size but Barak³² estimated most to be about 15 microns in dia., although some were as large as 200 microns in dia. The apparent conductivity with no electric fields applied to the electrodes was not greatly affected. When the electric fields were applied and currents began

to flow, the action of the currents seemed to increase the conductivity by several orders of magnitude.

When the powder was newly sprinkled in the tube it was not as evenly distributed as was desired. After firing a few detonations, however, the powder seemed to be replaced by a film throughout the inside walls of the test-section. When this state was reached, experiments measuring electric current and the electric field distribution were very reproducible so thoughts of improving the seeding technique were set aside. It may still be a worthwhile extension of this work to improve upon seeding methods to see how this will affect results.

The results reported in Chapter 5 as well as the electric fields and conductivities reported in Chapter 4 were all obtained with this seed material in the tube. During the course of a set of experiments no new seed was added as the supply did not seem to be quickly depleted once a substantial layer was deposited on the walls.

One disadvantage of this method of seeding is the fact that the transparent windows become coated with a white layer making them entirely useless for visual or schlieren studies.

3.9 Location of Observation Points

Provision for mounting the pressure transducers was made at four locations along the tube, and designated as sta (1), ... sta (4). These points are shown on Fig. 3-2. Sta (1) was approximately in the middle of the first electrode and 0.28 meters upstream of the field. Pressure of the detonation wave before it entered the field region was measured here serving as a reference to the other transducer further downstream.

Sta (2) was located 12.5 cm downstream of sta (1) but was never used in experiments. Sta (3) was located 1.05 meters downstream of sta (1) which was in the middle of the 3rd electrode of the test section, or about $3/4$ of the way through the field region. Sta (4) was located 20 cm downstream of the field or 1.48 meters downstream of sta (1). The computer program printed out values of p , u and c at these same four locations to serve as a convenient comparison between theory and experiment.

CHAPTER 4

DETONATION PRESSURE, ELECTRIC FIELD AND CONDUCTIVITY MEASUREMENTS

This section will be devoted to discussing pressure measurements made without fields as well as measurements of electric field and conductivity used to explain the pressure changes observed when fields were applied.

Wave speed measurements serve as one indication whether the experimental conditions are consistent with "theoretical model" conditions. Since the pressure of the flow field is more sensitive to change than is the wave speed, however, more emphasis was placed on pressure measurements, which show large changes when the wave speed remains apparently unaffected, within experimental accuracy.

4.1 Wave Speed

The method used to measure wave speed by noting the time taken for the wave to travel between the two transducers was not sensitive to small changes taking place in the interval. The measurement is an average velocity over the range, so even if the velocity changed by ten per cent over 1/3 of the length, this would register as an average change of about three per cent, by this measurement, which falls within the measurable accuracy for the wave speed measurements. Control runs taken using the same mixture on the same day, with all other variables stationary resulted in measurements well within this 3% margin.

Several variables were found to affect the wave speed. After the mixture had been in the mixing tank for several days, it would give slower detonations than when it was first mixed. This was observed by Kelly¹⁰ as well.

Another variable had an even larger effect on the wave speed. When fresh KCl powder was introduced to the tube, the wave speed was observed to increase by as much as 5%. Some of the high frequency "hash" observed on the pressure traces in the first 100 μ sec was also lost, giving a cleaner signal. After several runs, however, the loose powder seemed to disappear, leaving only a film on the tube walls. When this happened, the wave speed would stabilize to a value with very small (less than 3%) deviations from this value during a series of experiments. The pressure trace would also become very reproducible for control runs.

The value at which it stabilized may have been a function of the thickness of material on the wall, since from one day to another, this value was changed, again only of the order of 3%. In the data presented on Fig. 4-2, the runs shown (f) through (m) were all from one day's runs. The control run (f) shows a velocity of 2210 m/sec and the only other record of wave speed at that pressure, (j), also shows 2210 m/sec. The record shown as (e) on this figure was from a set of runs at a later date, after having added more KCl to the tube. The wave speed shown here is 2280 m/sec which is only about 3% higher than (f) and (j) but the author wishes to point out that all runs made at this later date which measured wave speed gave readings in the vicinity of 2280 ± 15 m/sec. So what appears, from the information presented on Fig. 4-2, to be an increase in wave speed for case IV is actually not, when all the data are examined.

The author was very careful to compare results with and without fields only for a series of runs which showed no appreciable variation in the control measurements made before, during and after a series of experiments. By so doing, any random error due to the unexplained effect of the fresh KCl powder was eliminated.

For the purposes of calculations in the computer program, a wave speed of 2200 m/sec for an initial pressure of 40 mm Hg. was used, to correspond approximately with experiments. This value is a little lower than theoretically predicted³³ but within about 3% of such predictions.

4.2 Pressure Profiles

Sample oscilloscope traces are shown in Fig. 4-2 illustrating pressure, current and voltage measurements. Fig. 4-2a shows the control pressure histories at sta (1) and (3) which will be compared to whatever changes appear on traces from field runs shown on (b), (c) and (d) of this figure. Fig. 4-2 (f) and (g) shows two control runs at sta(1) and (4) which are from the sequence which includes (h), (i) and (j). Fig. 4-2(k) shows a control pressure for 20 mm Hg. initial pressure at sta (1) and (4) to be compared with the runs (1) and (m).

These control runs will now be examined and compared with theory as well as to pressure measurements reported by other investigators.

The theoretical pressure-time profile as the detonation wave passes a point was obtained from the computer program with electric and magnetic fields set to zero. The values used to calculate the detonation jump conditions are noted on Fig. 4-3. This figure illustrates the difference between the calculated and observed pressure profile when no fields are applied.

Gordon¹³ has measured pressure profiles in hydrogen-oxygen detonations and noted similar discrepancy between the predicted pressure profile, with the rarefaction following the wave front, and the observed pressure. He used a crystal submerged in an oil bath to obtain his measurements, and Riemann theory of a progressive wave to predict the rarefaction following the detonation. Appendix 4 has tabulated results as published by Gordon compared with those measured by the author. The percentage drop he reports below the predicted value is very nearly what has been observed in the experiments reported here.

Consider first the initial peak in these experiments. As already mentioned in Chapter 3, the amplifier together with the filter had an overshoot of between 4 and 5% for a square wave input. This could account for part of the sharp peak observed in the pressure measurement. Another possible contribution to the pressure in excess of the C-J pressure could be that the point of complete combustion was far enough behind the wave front to permit the transducer to register a higher pressure indicative of the higher pressure in the reaction zone. Gordon¹³ has shown that the point of 90% reaction on the Hugoniot curve corresponds to a pressure 24% above the C-J pressure. The numbers noted here are more like 10% above C-J, so the transducer face, 0.218 inches in diameter, may be subjected to the higher pressures prior to complete reaction long enough to register a pressure above the C-J pressure. Edwards et al¹⁴ attribute a similar peak to a partial response of the gage to the von Neumann peak pressure within the detonation wave. Their argument was strengthened by noting that shock waves did not produce a similar peak and sudden drop at the wave front.

The shock reflected from the end of the tube was observed in the author's measurements at sta (4). These exhibited a small overshoot at the initial rise, somewhat like the detonation wave, although perhaps a little less pronounced. Compare for example the reflected shock shown on the bottom traces of Fig. 4-2 (f), (g), (h), (i) and (j) with the step change at the detonation wave for (k) which has approximately the same magnitude of change. (Comparing the overshoot for different sizes of pressure steps is not as meaningful as the transducer oscillation would ring more violently as a result of a 1 atm. pressure step than for a 1/2 atm. pressure step.) The shock profile which is closely followed by a rarefaction is somewhat similar to the detonation profile, as seen in (f), (g) and (h) of Fig. 4-2. In (i) and (j), the shock profiles look somewhat different, as the pressure changes behind the detonation wave have provided a different pressure field ahead of the shock, consequently leaving a different pressure field behind it. This illustrates another point. The reflected shocks here normally propagate into a non-uniform, decaying pressure field which results in a stronger rarefaction behind them. Shocks propagating into a uniform pressure field, as used by Edwards will look differently, so his conclusions about the different nature of profiles obtained from shocks and detonations are probably valid. At any rate, the author is in no position to disprove them, based on these reflected shock profiles. Examining Fig. 4-3, a significant drop of the observed pressure below the calculated pressure is observed during the first 100 μ sec after the detonation wave passes. Thereafter the lines become more nearly parallel. Appendix 4 tabulates this result and compares it to data taken from a figure by Gordon. It further goes

on to illustrate that this amount of pressure drop can be qualitatively explained by heat transfer alone. The mechanism of heat loss and pressure drop can be understood as follows. The gas in the vicinity of the wall is cooled and recombines causing the pressure to fall near the wall. This pressure drop is propagated into the free stream as a rarefaction wave, at the acoustic velocity of the hot gases. Kistiakowsky et al³⁴ attribute some reduction of wave speed to energy losses to the walls of the tube taking effect within the reaction zone. The time for crossing of such a wave in a 2 in. tube would be about 40 μ sec, which allows time for several wave crossings during the first 100 μ sec.

The concept that wall effects are responsible for the sudden drop in pressure can be verified by noting the effect of tube diameter on the pressure history. Edwards and Williams³⁵ made such a study and concluded that the energy losses to the tube wall were significant in determining the pressure profile. Their later measurements¹⁴ bear this out further as they observed that for a 10 cm diameter tube, the pressure falls off very gradually in some mixtures, and even increases for some mixtures during the first 100 μ sec after passage of the wave. With a 1.6 cm diameter tube, on the other hand, they observe a consistent drop ranging from 20 to 40 per cent during the first 100 μ sec. Gordon's results were obtained in a 4 cm diameter tube and the author used a 2 inch square tube. It is therefore also consistent that the pressure drop observed by the author and Gordon agree very closely, and fall in the range between the results obtained by Edwards for the 10 cm diameter and the 1.6 cm diameter tube.

The results of Edwards et al¹⁴ were obtained using a driver section

as opposed to the spark initiation used by Gordon and this author. Wolfson³⁶ used a 1.5 inch I.D. tube, spark ignition and had a distance of 13 3/4 feet from the ignitor to the pressure tap. He was primarily interested in checking the C-J pressure and did not attempt to correlate the pressure history with theory. The pressure data that he shows only spans the first 100 μ sec, but even from these data it is possible to note up to 30% or more decrease in pressure during the first 100 μ sec.

A quantitative argument is presented in Appendix 4 to illustrate that heat loss to the tube wall could easily account for the pressure falling below the level calculated by assuming no such loss. Measurements of heat transfer rates by Cutting³⁷ to a wire in the free stream of a detonation tube were much in excess of that required to explain the present discrepancy. Since it is expected that heat transfer rates to the wall will be lower, this does not discount the mechanism.

Further quantitative estimates based on the two dimensional model of flow expansion proposed by Fay³⁸ to explain wave speed deficits also predicted a large pressure drop. The discrepancy was so large however, that the model did not seem applicable in the region this far behind the wave.

Some of the pressure data presented in Chapter 5 was obtained at sta (3) which is located inside the field which necessitated attaching the transducer to a plexiglass window. A very regular oscillation was superposed on these measurements at a frequency agreeing with the time of traverse of a sound wave across the tube. See Fig. 4-2 (a). Edwards et al³⁵ report a similar observation, and confirmed the relationship

further by employing mixtures with different acoustic velocities. They smoothed out the oscillations for the published report, so comparison of amplitude is not possible. The natural frequency of vibration of the plexiglass window is around 4000 cps and the frequency noted here is around 17,500 cps so it is not a simple vibration of the window. At this location the transducer was held in place by a rubber bond rather than the diaphragm and ring combinations, as used in the aluminum windows. The author has concluded that these oscillations come about as a result of this mounting. The diaphragm-ring combination was first used at sta (3) and no such oscillation observed. Due to electrical interference during field experiments, presumably due to the metal ring being in contact with the gas or so near the electrode, the mounting was changed. This new mounting had no possible metal contact with the gas or electrode, so the electrical interference was eliminated, but a regular oscillation was now superposed in the pressure trace. It is believed that this flexible rubber bond together with the heavy piece of metal in which the transducer was mounted formed a spring-mass system which oscillated when given a "push" by the sudden pressure rise passing the transducer face. The author will have to treat the envelope of these oscillations as the error flag as he does not fully understand why they change in character when the gases are being acted upon by the electromagnetic fields.

The oscillations are not likely simple acoustic oscillations as they were not ever observed at sta (1) or (4), and the tube cross-section is essentially the same there.

Fig. 4-3 shows a lower pressure measured at sta (4) than at sta (1) contrary to the trend of a progressive rarefaction wave. This experimental trend was verified by interchanging the transducers . Invariably, the one downstream registered a lower pressure far behind the wave than the one upstream, although the initial peak agreed quite well. The reason for this is not quite clear but may be the result of higher rates of energy loss to the walls in the test section than in the tube upstream. Due to imperfect construction, the test section is a little irregular inside which may give rise to more turbulence with a higher rate of energy loss to the walls. The plexiglass windows may have heat transfer properties differing somewhat from the brass walls and so influence heat loss too.

4.3 Electric Fields

A description of the technique used in measuring the electric field in the gas was given in Chapter 3. Figs. 4-4 through 4-6 show some typical results of these measurements.

The upper plot in Fig. 4-4 show how the equal-potential lines cut diagonally across the tube in time at a fixed location in the tube. The lower one is a scaled schematic with the vertical distance the same scale as the horizontal distance behind the detonation front. If one were to plot current paths perpendicular to the equal potential lines, the lower one would illustrate that the current path is almost perpendicular to the tube axis, and not actually at the angle suggested by the upper plot. So the theoretical model of current only in the y direction is very nearly satisfied. Hall effects would still cause currents to flow somewhat more diagonally however.

It is interesting to note that the equal potential lines near the detonation front are not greatly affected by the magnetic field. The result of the Lorentz forces pushing on the gas (case III) is to shift the lines up, farther from the wave. For the Lorentz forces retarding the gas motion (case II) the lines are shifted in the opposite direction.

Fig. 4-4 was obtained from measurements made near the front of the electrode. A similar plot is obtained from measurements at the center of the electrode or at the point near the end.

Figs. 4-5 and 4-6 are typical plots used to determine the actual voltage drop across the free stream. The upper line on the plot is the voltage on the anode, the second is the potential at the point 0.10 in. from the anode as obtained from a plot like Fig. 4-4. The bottom line is the corresponding potential 0.10 inches from the cathode. The line in between is obtained by taking the difference of potentials between the second line and the bottom line, and it represents the potential drop between the two probes nearest the electrodes. To facilitate use of this information in computations a relation was needed to place in the computer program. The form of equation chosen for each location was

$$f_i(x) = f_1 + f_2 x + f_3 x^2 \quad (4.1)$$

where the constants f_1 , f_2 and f_3 were evaluated by using three values of $f_i(V)$ from a plot like Fig. 4-5. This was done at two locations along the electrode to obtain x' dependence. Linear interpolation was used to get the voltage at a general location, or

$$f(V) = \frac{f_{ii}(V) (x' - x_i) - f_i(V) (x' - x_{ii})}{x_{ii} - x_i} \quad (4.2)$$

This expression was then divided by the distance between the two outer points of the electric field probe to get the electric field as a function of τ and x' , where x' here is measured from the front of the electrode. The resulting expression was of the form

$$E(\tau, x') = e_1 + e_2 x' + e_3 \tau x' + e_4 \tau^2 x' + e_5 \tau + e_6 \tau^2 \quad (4.3)$$

where the values of the e 's were obtained from use of equations 4.1 and 4.2 and the other described operations.

Equation 4.3 is valid for one electrode of length 0.5 meters and good only for $\tau \leq 600 \mu\text{sec}$ by the way it was derived. The second electrode was assumed to behave as the first, so the same expression was used there with x' beginning from zero at its beginning.

4.4 Electric Conductivity

Efforts to measure the electric conductivity of the gas directly by means of a d-c probe proved futile. The results of these attempts were unreliable for several reasons.

First, the conductivity level was too high for good measurements by this technique. Using a circuit such as Kelly¹⁰ used was unsatisfactory because the output signal was strongly dependent on the battery voltage. To operate correctly, the probe should apply a constant voltage across the gas thereby allowing the current across a load resistor to serve as a direct indication of gas conductance. To attain this condition, the load resistance must be much smaller than the resistance offered by the gas. The simple model to interpret results of this probe is valid only for small currents, so the range of necessary conditions restricted one

to using a small battery, and a small load resistance. With these conditions the noise level often caused the signal to go negative, leaving little confidence in the validity of such a record.

Secondly, such a probe used in the presence of other large electric fields introduced many uncertainties so that it could only be used outside the field. Indications of those measurements obtained, were that the conductivity increased due to the action of the currents, and one was not certain how a measurement downstream of the field could be related to the values inside the field.

Other measurement techniques may have accomplished what was needed, but for the purposes of correlation of theory and experiment, it would suffice to know the current distribution since the total current was easily measured by the Rogowski coil. The needed information was therefore obtained in the following way.

It was assumed that there was a conductivity distribution convecting along behind the wave which had no x dependence but could be expressed as a function of τ only, or

$$\sigma(\tau) = s_1 + s_2 \tau + s_3 \tau^2 + s_4 \tau^3 \quad (4.4)$$

The total electric field is,

$$E^* = E(\tau, x') - \overline{uB} \quad (4.5)$$

where \overline{uB} was taken as an average product of u and B .

If we take this expression for the electric field, multiply it by the conductivity and integrate over the conducting slug which is between the electrodes, this sum at any time should equal the total

current flowing to the electrode at that time.

$$I(t') = \int_{x'=0}^{S-B} \sigma(\tau) E^* dx' \quad (4.6)$$

where S-B is the slug boundary. When the wave is partly through this electrode region, integration is over the distance from the front end of the electrode to the wave front, since no currents flow upstream of the wave. Once the wave is beyond the electrode, integration is over the entire length of electrode, in which case the slug-boundary is $x' = 0.5$ meters.

To perform the integration, use is made of the relation

$$\tau = t' - V_{NOT} \cdot x' \quad (4.7)$$

where t' is the time after the wave front enters this electrode region

x' is the distance the wave front has progressed beyond the front edge of the electrode.

The total current, $I(t')$ is obtained from experiments where a Rogowski coil is used to measure the total current to the first electrode. The current traces corresponding to pressure traces are shown in Fig. 4-2 for each run represented. It may be observed that the total current traces look somewhat different for different cases. For each case studied in detail, the electric field distribution was obtained, multiplied by the assumed conductivity distribution and integrated over x' . The $I(t')$ for each was obtained from a typical current trace for that case. These current traces were found to be quite reproducible on a given day, but when fresh KCl was added, they would take on a different appearance. The major part of the data reported was obtained

on two days, separated by several weeks, and an addition of KCl. The runs with combined electric and magnetic fields for simultaneous pressure measurements at sta (1) and (4) and simultaneous electric field measurements were obtained on one day. These are typified by (f) through (m) of Fig. 4-2. The runs for electric field only, sta (1) and (4) and all the simultaneous runs at sta (1) and (3) were obtained in a second two-day span typified by (a) through (e) of Fig. 4-2. The total current traces for the second series are a little different than for the first series, for apparently equivalent initial conditions. Electric field measurements used in the computations were only obtained the first day, except for case I which was mapped the second day. Some of the discrepancy between theory and experiments may be traced to the change of electrical properties between these sets of runs.

A typical $I(t')$ plot is shown in Fig. 4-7. This one is for case II. The resulting $\sigma(\tau)$ for this case is shown plotted in Fig. 4-8. Perhaps Eqn. 4.4 is a little too restrictive an assumption on σ , as the tail on $\sigma(\tau)$ for τ approaching 600 μsec seems a little unreal. Keeping in mind that determining the conductivity level and the resulting current distribution was the main objective in getting this solution, the results are probably adequate for this purpose. One would not want to argue that the conductivity distribution was exactly this result without studying the effect of using more general forms of conductivity distribution in the calculations.

Solutions for all the cases studied in detail are tabulated in Appendix 5, giving the electric field and resulting conductivity distributions.

These values of $\sigma(\tau)$ and $E(\tau, x')$ were fed into the computer program to obtain the results for each case.

The gradual increase in conductivity with time after the wave passes, as shown in Fig. 4-8, may result from having the seed material coated on the walls, rather than distributed in the free stream. The high conductivity observed was due to the seed material, however, as such conductivities were not obtained before adding the KCl. The process by which the effects are noted in the free stream when the material is initially coated on the walls is the topic of a brief discussion which follows.

Electrons accelerated by electric fields will bombard neighboring molecules and atoms producing more electrons.³⁹ This process of multiplication of charge requires large electric fields to accelerate the electrons sufficiently to produce higher concentrations of electrons. The electric fields in the free stream here, as determined from probe measurements, are not large enough to account for the high concentration of electrons, on the basis of this mechanism.

Turcotte and Friedman⁴⁰ have concluded that seed material coated on the electrode surfaces during flame studies is responsible for high rates of electron emission. Since the work function of potassium³⁹ is only 2.2 volts, it is reasonable to conclude that it could be emitting electrons thermionically and still be well below the free stream temperature. (See Appendix 1) In the experiments described here, there was a coating of seed material, which started as KCl, on both electrodes as well as on the side walls of the tube.

In the electric field measurements, a cathode drop of between 100 and 150 volts is observed immediately behind the wave front. This drop decreases with time until it reaches a value in the vicinity of 45 volts. Emission of electrons at the surface, increasing with time as the temperature of material on the surface rises, could qualitatively explain this trend.

A slightly smaller anode drop is observed initially, but rather than decreasing, this drop increases until a drop of several hundred volts occurs across 0.1 inch. Ohmic heating in this thin layer would further raise the temperature of the seed material on the anode, causing emission of electrons. The electrons emitted at this surface would undoubtedly be accepted by the positively charged anode, leaving a high concentration of K^+ ions near the surface. Positive potassium ions have a very large collision cross-section which would inhibit electron flow, giving the effect of a high resistance. This would qualitatively explain why a large potential drop is required near the anode, to pass the current.

CHAPTER 5

THE EFFECT OF ENTHALPY ADDITION AND LORENTZ FORCES ON THE FLOW FIELD

The previous chapters have explained the theoretical derivation and how calculations were carried out. Experimental procedures have been explained and some results discussed which are important to the final discussion but only lead up to it. In this chapter, the results of computations will be presented as well as the results of experiments. By way of introduction to this discussion, it may be said that the theoretical computations provide a good basis for understanding the experiments, and the experiments point out some of the strong points as well as some weaker points in the idealized theoretical development.

Shock tube experiments will unavoidably contain phenomena such as boundary layer effects and the many complicating aspects which accompany boundary layers. The theory which has been developed was intended as a guide to the investigator to predict the type of results to be expected. Therefore, what the author will emphasize in presenting and discussing results is the trend predicted by theory as compared to the trend observed in experiments. The trends are characterized by certain features such as compressions in one region resulting in a pressure rise, and rarefactions in another region resulting in a pressure decrease. Some of the trends seen in the idealized theory would be accentuated if loss mechanisms were included, others would be suppressed by losses. Insight into effects caused by losses can be gained when solutions simulating losses are examined. Following then, is a presentation of results of solutions with

no losses considered together with results of solutions where possible losses are simulated. This is followed by a presentation of trends as observed in experiments. The magnitude of changes observed in experiments is also cautiously compared to the magnitudes predicted in theory.

5.1 Cases Studied

A brief explanation of the method used to categorize results is in order. The conditions used in experiments which the theory attempted to correspondingly simulate were divided into seven cases as summarized in the table.

CASE	INITIAL VOLTAGE ON ELECTRODES	APPROXIMATE MAGNETIC FIELD STRENGTH
0 (control)	0	0
I	500	0
II	500	-1 web/m ²
III	500	+1 web/m ²
IV	1000	0
V	1000	-1 web/m ²
VI	1000	+1 web/m ²

Case 0, or the control case, is discussed in Chapter 4. Since theory and experiment show significantly different pressures even for this case, the discussion which follows will be carried on, on the basis of comparing the pressure changes observed between control and "with field" experiments to the changes predicted between control and "with field" solutions.

Cases I and IV have only electric fields, with case IV passing more current through the gas. Cases II and V are similarly related but with

magnetic fields oriented so that the Lorentz force opposes the flow. Cases III and VI are the parallels to II and V with the Lorentz force pushing the flow.

In the experiments with magnetic fields, these cases had a \bar{B}_{\max} of about 1.1 web/m^2 which would give an approximate average of 1 web/m^2 during the time of the experiment. (Fig. 3-3)

An extra set of computations was performed for cases II, III, V and VI by setting the $\bar{E} \cdot \bar{j}$ term to zero and considering the effect of losing all the electrical enthalpy added by some unspecified heat loss mechanism. These solutions are designated as IIA, IIIA, VA, and VIA respectively. This set of solutions would be realized in practice when dissipative phenomena just balanced the energy addition.

5.2 Trends of Theoretical Predictions

By the nature of the governing equations it was necessary to solve for the quantities u , c and p as well as the x and t location of each lattice point. Theory, therefore, readily provides more information than experiments and by using this information about changes in u and c as well as p , it is easier to understand how the overall changes in pressure are brought about.

One way of observing trends in theoretical solutions is to observe how the physical characteristic net is changed. Figs. 5-24, 25 and 26 are the x - t diagrams obtained from solutions for cases I, II and III. These three cases illustrate the three basic categories being studied. Case I (Fig. 5-24) illustrates the effect of electric fields only, case II (Fig. 5-25) the combined effect of electric fields and Lorentz forces

which retard the gas motion and case III (Fig. 5-26) the combined effect of electric fields and Lorentz forces which push the gas in the direction it is already flowing.

Each x-t diagram will first be compared with the diagram obtained from the control run, case 0, which is shown in broken lines. The broken line has been omitted wherever it was approximately coincident with the solid line. The trend of each will be noted and compared to the other two.

The x-t diagram for the control run is much easier to interpret than these shown for cases I, II and III. Since no losses are considered in this idealized theory, and no energy or momentum changes are introduced in case 0, the flow field is isentropic and behaves according to simple relations such as those given by eqn. (2.35) and (2.36). From eqn. 2.36, it can be seen that when u decreases, c decreases and vice versa. From eqn. 2.35 it can be seen that when u decreases, p decreases and vice versa. When both u and c decrease, the type II characteristics bend back more than the type I characteristics, giving a fan shape associated with a rarefaction. The opposite shift occurs when both u and c increase and this depicts a compression.

For the non-isentropic cases such as these with electromagnetic energy addition and momentum changes, no such generalizations can be made. Equations (2.19) and (2.21) illustrate the complicated relationship between the properties u , c , and p for the electromagnetic case. So in interpreting the x-t diagrams, all that can definitely be obtained from observing the characteristics is the changes in $(u-c)$ and $(u+c)$ compared to other cases. To facilitate pressure comparisons, the author has written in the pressure at each lattice point shown, in cm of Hg.

Approximate comparison with the control pressure can be made by noting, as for the region upstream of the field in each case, that the pressure does not change along a type I characteristic for the control case. Therefore an estimate of what the control pressure at any point would be can be obtained by noting what the pressure on that same type I characteristic is, upstream of the field. This is not exact due to the shift in location of the lattice point for the different cases. A more exact comparison is obtained by cross-plotting pressure vs. x , or pressure vs. time behind the wave as are shown in Figs. 5-1, 4, 7, 9, 11, 13, 15, 17, 19, 21 and 23. The pressure vs. time plots were used because they are a direct parallel to what is measured by a transducer in a fixed location in the tube. Pressure vs. x experimental data would have to be obtained from cross-plotting measurements from numerous positions along the tube. This was not done for the experiments, or for the theoretical solutions.

Comparing Figs. 5-24, 25, and 26 can provide insight into some overall trends. All the plots exhibit some increased backward bending of the type II characteristics near the beginning of the field as well as some increase in pressure in this region. Case II which has the Lorentz force retarding the particle velocity exhibits this character most strongly. All the cases shown here would produce some change at sta (1) after some time but the changes occurring for the case with the Lorentz force retarding the flow would appear at sta (1) after about 850 μsec or less after the wave passed that point, whereas for the other two cases the changes would be noticed somewhat later, and the rise in pressure would be greater for this case (i.e. with Lorentz

forces retarding the flow) than for the others. Since solutions were terminated after about 900 μ sec behind the wave, the only one of these three cases showing changes at sta (1) during this time was case II.

Fig. 5-7 shows the p vs time plot at sta (1) for case VA. Case VA has the same orientation of magnetic field as case II, with a higher current density, but it considers the $\overline{E} \cdot \overline{j}$ enthalpy addition to be just balanced by heat loss by some unspecified mechanism. For this case there is no change in stagnation enthalpy, so the effect observed is due to Lorentz forces alone. The solution for case IIA, which neglects the enthalpy addition of case II in this same way, is not noticeably different from the control run as far as is plotted here. The solution for case II shows a pressure rise beginning at about 850 μ sec behind the wave front and rising more gradually than for case VA.

Next, the trends throughout the field region will be discussed. Comparing Fig. 5-24 and 26 it can be seen that cases I and III have about the same slope of type II characteristic throughout the field region, but the type I characteristics for case III are bent more toward the wave front than for case I. This means that $u-c$ is about the same for each, but $u+c$ is greater for case III. Comparing the actual magnitudes of each at sta (3) which are plotted on Fig. 5-2 and 5-18 it can be seen that case I has a reduction in particle velocity and an increase in sound speed (temperature) to give a larger difference in u and c than for the control run. This causes the type II characteristics of slope $1/(u-c)$ to bend backward more than for the control run. By adding the particle velocity and sound speed at any point as shown on

Fig. 5-2 it can be seen that $u+c$ for case I is higher than for the control immediately behind the wave but lower than the control after several hundred microseconds. This means that the type I characteristic of slope $1/u+c$ bends toward the wave near the wave more than it did in the control, but since $u+c$ is still not perceptibly larger than $(u+c)_{C-J}$ there will be little modification of the detonation wave speed. In case III on the other hand, the Lorentz force is pushing the particles so the particle velocity is not reduced as in case I; in fact it stays very near the control as is seen in Fig. 5-18. Immediately behind the wave, in case III, both the sound speed and particle velocity are increased above the C-J level, causing the type I characteristic to bend toward the wave and giving more promise of wave speed changes. These wave speed changes will be discussed further later.

It has already been noted that for case II, the type II characteristics bend backward more than for either cases I, III or the control. Fig. 5-10 shows the plot of u and c vs. time at sta (3) for this case. From this it can be seen that u is decreased and c increased to give a large change in $u-c$. Here the Lorentz force is helping to reduce the particle velocity.

The tendency for the particle velocity to be reduced for case I, which has only energy addition and no momentum changes, can be understood from eqn. (2.21) which shows that the energy addition term, here shown as kEN/Bc , along the type II characteristic causes a decrease in u . And for case II, the Lorentz force has the same effect, causing a larger decrease in u than for case I. For case III, the Lorentz force has the opposite effect of the energy addition along the type II

characteristic, keeping the particle velocity near normal.

From Fig. 5-10 for case II, it can be seen that even near the wave front $u+c$ is less than $(u+c)_{C-J}$, so interactions with the wave front can be ruled out at this point of the flow field for this case.

So, from these observations, it can be noted that the Lorentz force can have a significant effect on the distribution of energy between the mode of thermal energy characterized by the sound speed ($c^2 = kRT$) and the mode of flow energy characterized by the particle velocity. Without adding or subtracting any enthalpy then, the temperature can be raised by reducing the particle velocity and vice versa. This is an important observation as it provides an understanding for the different pressure changes for these various cases.

From eqn. 2.19 it can be seen that pressure changes are directly proportional to changes in sound speed but are only weakly related to the particle velocity through the \bar{uB} term. For the three cases being compared here, the electromagnetic term on the right side of eqn. 2.19 is approximately the same for each, or at least considerably less than the term involving sound speed change, so the pressure compares almost as the sound speed among these three cases.

Comparing cases I and II, it can be noted from comparing Fig. 5-10 for case II and Fig. 5-2 for case I that the sound speed is generally higher for case II. This, it may be recalled, was partly due to the Lorentz forces in case II retarding the particles, causing more of the total energy to appear as heat by redistribution of energy. From this discussion, it would be expected that the pressure would be higher here for case II than for case I, as indeed it is. (Fig. 5-9 vs. Fig. 5-1)

The author would like to caution the reader from carrying some of these arguments further than they are taken here. It will be recalled that the electric field and conductivity values used in these calculations were obtained from experiments as described in Chapter 3 and 4. So, although the initial voltage on the electrodes was the same, subsequent developments not all of which are understood, affected the electric field and current densities, so that the energy input was not the same for these three cases even when the initial electrode voltage was the same. One of the main purposes of these solutions was to duplicate experimental conditions as closely as possible. As a result of this, some of the qualitative comparisons which would lead to quantitative comparisons between cases must be carried on cautiously since the total energy addition was not quite the same for each of these three cases.

Some comparisons can be carried further nevertheless. From comparing the sound speed of case III (Fig. 5-18) with that of case II and I, (Figs. 5-10 and 5-2), it will be noted that c is higher for case III than for either of the other two cases. Correspondingly, the pressure for case III, (Fig. 5-17) is higher than for either case I (Fig. 5-1) or case II (Fig. 5-9).

The comparative trends of the solutions in the transition from the field region to the downstream region is also of interest. For case I, and II the type II characteristics (Figs. 5-24 and 5-25) were bent backward more than the ones for the control (in broken lines) throughout the field region. These now gradually return to the normal slope. From Fig. 5-14 it can be seen that $(u-c)$ is still smaller than $(u-c)$ for the control run, but in comparing it to Fig. 5-10 it can be seen that both

u and c have changed a great deal in the interval. The reader is reminded that the electromagnetic fields have no direct effect in this downstream region. The difference from the control run is only due to what is convected downstream with the flow. Even in this purely one-dimensional case, there are changes in the flow field as it leaves the electromagnetic field region. These changes are brought about by the following mechanism.

One term remains in effect in eqn. 2.21. This term, shown expanded in eqn. 2.22 results from lengthwise derivatives in p and c which accounts for lengthwise distribution of entropy. (Shapiro¹⁹ p. 977). Upstream of the field region where the flow was isentropic, this term had no influence. (Even in the approximate numerical technique employed for these solutions, this term had a negligible contribution as it should ideally for the control run which was intended to have an isentropic solution in the flow field.) Inside the field region, this term has some effect and downstream it accounts for all the changes taking place. In this downstream region, it has the effect of bringing about a redistribution of energy.

As a result of this redistribution of energy, for case I the particle velocity which was below normal at sta (3) (Fig. 5-2) is now slightly above normal at sta (4) (Fig. 5-5). The sound speed which was above normal at sta (3) is still slightly above normal and the pressure has also returned almost down to the control level, Fig. 5-4.

For case II, the particle velocity which was far below normal at one point at sta (3) Fig. 5-10, is now very nearly back to normal, Fig. 5-14. The sound speed is also seen to decrease between sta (3) and sta (4), Figs. 5-10 and 5-14, as some of the thermal energy contributes

to acceleration of the gas particles. There is a large decrease in pressure between sta (3) and sta (4) for this case. (Fig. 5-9 and 5-13).

For case III, the type II characteristics actually bend back less than for the control in this downstream region. (Fig. 5-26) By comparing particle velocities and sound speed changes between sta (3) and (4) for this case (compare Fig. 5-18 with Fig. 5-22) it can be seen how the equalization process already mentioned has brought the particle velocity from a level around the control at sta (3) to well above it at sta (4). At the same time the sound speed has been decreased somewhat but remains above normal. As a result of this, their sum, $u+c$, is actually higher for the most part than it was at sta (3) giving increased bending toward the wave front of the type I characteristic (Fig. 5-26). Again the pressure reflects the trend of the sound speed and remains well above normal. Fig. 5-21.

To summarize the trends of these solutions then, it was pointed out that case II, which has the Lorentz force opposing the flow direction, would produce the largest pressure change at sta (1). The electromagnetic effects are expected to generally increase the pressure above the control level, with the largest changes occurring for case III which has the Lorentz force pushing the flow. There is an expected trend of decreasing pressure as the flow leaves the field, with case II, which had the greatest decrease in particle velocity within the field region due to the effect of retarding Lorentz forces, showing this effect most strongly.

5.3 Detailed Results of Computations

The preceding discussion dealt with trends in solutions and what

generally caused these trends. The solutions discussed up to this point were idealized solutions in the sense that no deviation from one-dimensionality was allowed. In examining the solutions at each point, a parallel set of computations will be presented which, in a simple way, simulate the possible effect of energy losses to the walls of the tube.

Since the information gleaned from experiments does not include any direct measurements of heat loss or viscous dissipation losses, it is impossible to provide the computer with all conditions existing in the experiments. Consequently, only if these loss mechanisms had made negligibly small contributions could the theory predict accurately what would be the effects observed in experiments.

The effects of losses can be simulated however. An extreme case simulating additional heat loss would be if the electrical energy added was just balanced by losses so the only net effect remaining was that caused by Lorentz forces. This case was realized by setting the $\bar{\mathbf{E}} \cdot \bar{\mathbf{j}}$ term equal to zero. Perhaps a more realistic way to simulate additional heat loss would be to limit the temperature rise above normal, (since the present scheme leads to some ambiguities as will be seen) but this will be discussed later. (See Appendix 7) The case of only electric and no magnetic field applied was studied both theoretically and experimentally and so the case of no momentum changes is taken care of. Partial losses of both effects can be observed by studying cases of lower current.

The author therefore provides solutions with both $\bar{\mathbf{E}} \cdot \bar{\mathbf{j}}$ and $\bar{\mathbf{j}} \times \bar{\mathbf{B}}$ included for low current levels. A solution with only $\bar{\mathbf{E}} \cdot \bar{\mathbf{j}}$ is included to show the effect of heat addition alone. Finally solutions at both the higher and lower current levels used in experiments are provided, by

artificially setting $\overline{\mathbf{E}} \cdot \overline{\mathbf{j}}$ to zero, which show the effect of Lorentz forces alone. This last set of solutions may have no exact parallel in experiments but is helpful in understanding the effects of heat losses when Lorentz forces are large enough to substantially change the flow field conditions.

In all the cases considered, the region of primary interest is the first 400 to 500 μsec after passage of the wave at sta (3) and (4). At sta (1) the region of interest begins later than that, and so for the interesting cases here, results will be presented as long as 900 μsec after the wave passes.

a) Cases I and IV (Electric Fields only)

These two cases are considered jointly as they are qualitatively alike and quantitatively differ primarily in the current density in the gas. Due to this similarity, computations were performed only for case I.

No interesting changes in conditions are predicted for this case at sta (1), within the region of interest.

Fig. 5-1 shows the predicted pressure rise at sta (3) while Fig. 5-2 shows the corresponding changes in particle velocity and sound speed. The reason for the decrease in particle velocity below the control solution may be traced to the governing equations (as was discussed in section 5.2) which give a negative increment to u for heat addition along the type II characteristics. At a point after 600 μsec , the type II characteristic which crosses the sta (3) position originated downstream of the field so it doesn't impose so great a velocity decrease. Consequently, from this point on, the particle velocity, taking energy from the heat energy stored in the gas, gradually approaches the value

of the control case. This latter process produces a decrease in sound speed (temperature) and is brought about by the term in the equation which comes from gradients in the properties c and p in the flow field which may be identified with entropy changes (as pointed out earlier).

The outcome of these equalization processes may be seen at sta (4), (Fig. 5-4 and 5-5). Here the pressure is only slightly above the control case. The particle velocity is now also slightly above the control case, and the sound speed, although reduced from sta (3) is still well above the control solution.

For these cases with no magnetic field, the effect of losing all the additional heat added would simply bring the solution back to the control solution.

b) Cases II, IIA and VA (Lorentz Force Retarding Flow)

These cases have interesting effects at sta (1). The solution for case II predicts a small pressure pulse accompanied by an increase in sound speed and decrease in particle velocity propagated back from the fields region which appears at sta (1) after 850 μ sec. When the $\vec{E} \cdot \vec{j}$ term was omitted, case IIA showed no pressure pulse, while case VA still had a pulse at sta (1) as shown in Fig. 5-7. Fig. 5-8 shows the corresponding changes in particle velocity and sound speed.

Fig. 5-9 shows the predicted pressure rise at sta (3) for the cases II and IIA, with the corresponding sound and particle velocity shown on Fig. 5-10. The current density and electric field for case II is not substantially different from case I, but the distribution of energy is apparently influenced by the Lorentz forces. Comparing Fig. 5-2 with 5-10, it can be seen how the Lorentz force has retarded the flow, case II,

reducing the particle velocity a great deal more than in case I. The flow energy which is reduced when the particle velocity is reduced appears as thermal energy as the sound speed for case II is considerably higher than for case I. It can further be noted from Fig. 5-10 for case IIA, when no enthalpy is added, that the sound speed is still increased above the control value due to the redistribution of energy when the particle velocity is suppressed.

The predicted pressure, sound speed and particle velocity changes for case VA, at sta (3), are shown on Figs. 5-11 and 5-12. Here again the particle velocity is greatly reduced and the sound speed increased.

As the wave leaves the field, the equalization processes, noted in case I, again take effect and the properties approach their control values at sta (4). Fig. 5-13 shows the pressure at sta (4) for cases II and IIA. Both are only slightly different from the control value with case II slightly above and case IIA slightly below the control pressure. The particle and sound velocities for these cases are shown on Fig. 5-14.

The pressure, sound speed and particle velocity at sta (4) for case VA are shown on Fig. 5-15 and 5-16. Here the pressure is considerably below the control case, the particle velocity is well below its control case, and the sound speed oscillates around its control.

It is noteworthy that the electromagnetic term on the right of eqn. 2.19, giving the pressure change along the path line is j^2/σ . When $\bar{\mathbf{E}} \cdot \bar{\mathbf{j}}$ is zero, there still remains a term of $\bar{\mathbf{u}} \cdot \bar{\mathbf{j}} \times \bar{\mathbf{B}}$ which contributes to a pressure decrease for cases IIA and VA.

c) Cases III, IIIA, and VIA (Lorentz Force pushing Flow)

There is nothing of interest predicted for sta (1) during the observation time for these cases although small changes may appear later as observed from Fig. 5-26.

Fig. 5-17 shows the pressure rise predicted at sta (3) for cases III and IIIA, while the corresponding changes in sound speed and particle velocity are shown on Fig. 5-18. For case III, the Lorentz force is tending to increase the particle velocity and the enthalpy addition to decrease it. The resulting effect is that the particle velocity is very near the control level, the sound speed is greatly increased above the control level and the pressure is also a great deal higher than the control level. Without the enthalpy addition, case IIIA, the particle velocity through momentum changes rises much higher than the control level, (Fig. 5-18) the sound speed must compensate as there is no enthalpy added and it goes below normal. The pressure follows the trend of the sound speed and also falls below the control level.

The solutions for case VI A at sta (3) are shown in Figs. 5-19 and 5-20. The increased current (over IIIA) results in a greater Lorentz force with the result that the particle velocity increases even more than for case IIIA. Again, since the stagnation enthalpy remains unchanged, the sound speed must decrease to compensate, and now the particle velocity exceeds the sound speed after about 300 μ sec. This decrease in sound speed corresponds to a temperature decrease of about 1000°R. The pressure is initially above normal, but when the sound speed decreases so rapidly, the pressure follows this trend until it is far below normal.

The equalization tendency already noted, as the wave leaves the field, again takes effect for these cases. For case III, the particle velocity, which had remained near the control level up to sta (3), now increases to a level above the control at the expense of the sound speed which is decreased but still remains well above the control level. The pressure is reduced somewhat from sta (3) but remains well above the control level.

Technical difficulties prevented the computer solutions from going through to sta (4) for cases IIIA and VIA. Only some calculated information could be kept in storage due to the limited size of the computer memory. Some information already deleted was required for the completion of these solutions. The difficulties were not insurmountable, but the solutions were not deemed important enough to make the necessary alterations in the mechanics of the program at this time. Based on trends in other solutions, the author will deduce the final outcome of these two solutions.

For case IIIA, the particle velocity and sound speed would return approximately back to the control level, with both perhaps a little above the control. The pressure would again follow the trend of the sound speed and end very near the control level.

Based on intermediate points in the solution for case VIA, the tendency is similar to other cases. It appears as though the particle velocity will remain a little above normal, the sound speed was returning toward the control level but was still well below it after several hundred μsec . The pressure at the intermediate point seemed to be well above normal for the first several hundred μsec , and then follow the trend of the sound speed and fall below normal.

d) Wave Speed

Since the treatment of the problem is one-dimensional, with the same chemical energy added in the wave in the presence of electromagnetic fields as without them, the only possible solutions other than the C-J solution are ones having increased velocity corresponding to strong detonations. The changes predicted in the cases studied are very small. Case I shows a maximum increase of .0045%. Case II a maximum increase of .0063% while case III predicts a maximum increase of .032%. These changes did not persist as an average change. The numbers quoted here are the maximum increase above the control velocity. The average velocity would be even closer to the control.

The cases with no enthalpy addition were not very different at the wave front. The maximum increase for any of these was 0.43% for case VIA.

The overall trend from these solutions at the wave front is one of very little or negligible change. The reason for this can be traced to the fact that the electrical conductivity at the wave front is much lower than in most of the flow field. Consequently, most of the energy input and the maximum momentum change occurs too far behind the wave to strongly affect the wave front within the short field region.

In comparing solutions for no heat loss to the tube walls to those solutions simulating heat loss by considering all the electrical enthalpy which was added to be lost, it is found that the effect of heat loss is to reduce the pressure. In the case with the Lorentz force retarding the flow, the temperature still rises above normal when no enthalpy is added and the pressure is reduced below normal downstream of

the fields. For the case of Lorentz forces pushing the flow, the accelerated gas flow causes the temperature to drop far below normal, which in turn causes the pressure to fall below normal.

5.4 Experimental Results

Before giving a detailed account of experimental results for all cases, the author would like to point out the conditions under which very definite changes in pressure were seen. The oscilloscope traces shown in Fig. 4-2 illustrate the most interesting cases. As a reference regarding the dependability of reduced results, the reader may refer to Appendix 3. An account of how data were reduced to the form presented in this chapter is given there, with a plot showing error flags which could be attached to all such measurements. The oscilloscope traces shown in Fig. 4-2 illustrate typical results. Some show no changes from the control, others show substantial change.

Fig. 4-2(a) shows pressure traces for a control run. The high frequency wiggles in these curves were assumed to be associated with the transducer ringing characteristics and were smoothed out in plotted data. The lower frequency wiggles observed at sta (3) were assumed to be due to acceleration effects caused by the mounting of the transducer, as discussed in Chapter 4. These wiggles were plotted on graphs although some reservation was held about their significance, as was discussed in Chapter 4.

Fig. 4-2 (b) shows traces for sta (1) and (3) for case IV. No perceptible change from the control is observed at sta (1). At sta (3) the first thing to notice is the smoothed out wiggles. A slight rise in pressure is observed here as plotted in Fig. 5-3.

Fig. 4-2 (c) shows the pressure traces for sta (1) and (3) for case V with the $\bar{j} \times \bar{B}$ forces retarding the flow. The upper trace (sta (1)) clearly shows a pressure rise at about 640 μsec behind the wave. Theory predicted that this orientation of fields, of the three considered, would produce the largest pressure change at sta (1) and this piece of experimental evidence is in direct support of this prediction. Little can be said of any change observed at sta (3) of this figure.

Fig. 4-2 (d) shows the pressure traces for case VI at sta (1) and (3). No change is observed at sta (1), which further substantiates the agreement noted above for case V. The pressure rise at sta (3) is not as large as theory predicts but it is perceptible. Of the three categories considered, theory predicted the largest rise at this station for this orientation of fields. Again experiments with this orientation of fields gave the largest pressure increase.

Fig. 4-2(e) shows the oscilloscope traces at sta (1) and (4) for the case of electric fields only (case IV). Again, nothing of note is seen at sta (1), and no obvious change is seen at sta (4). The small effect predicted by theory at these two stations for this case would probably be difficult to detect with the present apparatus.

Fig. 4-2(f) shows a control for sta (1) and (4) to be compared to the following four illustrations. Fig. 4-2(g) is another control with the pressure from the downstream transducer not added to the upper trace. This provides a sharper contrast to the one which follows.

Fig. 4-2(h) is another set of traces for the $\bar{j} \times \bar{B}$ force retarding the flow, but for sta (1) and (4) now. This again illustrates the pulse seen in (c) at sta (1). The pulse here does not have as sharp a rise as

the one in (c). Comparing the current flowing to the electrode, as shown in each case, it can be seen that the current rises faster for (c) than for (h). This would indicate that there is greater concentration of current near the leading edge of the electrode in (c), resulting in a larger interaction with the magnetic field, hence producing a larger pulse which steepens more. Results of this type are shown plotted on Fig. 5-7. By comparing this figure with Fig. A3-1, the reader can clearly see that the probable error flags on that figure do not enclose the large changes plotted on Fig. 5-7. The lower trace of Fig. 4-2(h) illustrates the changes in pressure observed at sta (4) under these same field conditions. It is obvious that at times around 500 - 600 μsec behind the wave, the point-by-point pressure on this curve is lower than the corresponding points of the control. Fig. 5-15 shows a plot of some typical results obtained for these conditions. Again the error flags would not enclose these points. The current density for these experiments is in the vicinity of 10 amps/cm^2 and the magnetic field strength about 1 web/m^2 .

Fig. 4-2(i) and (j) show two representative sets of traces for the case when current densities are again in the vicinity of 10 amps/cm^2 , and the magnetic field of about 1 web/m^2 combines with the current to push the gas flow. In the upper trace of (i) there is again no distinct rise in pressure as observed on the upper trace of (h). After reduction of data, any change at sta (1) for this case falls within the error margin cited on Fig. A3-1, giving further significance to the result seen on the upper trace of Fig. 4-2(h) and (c). The upper trace of Fig. 4-2(j) has the downstream pressure added at a reduced scale.

This was used, as in the control shown in (f) to measure the wave speed between the transducers. This could be disconnected to observe the entire trace at sta (1) as was done in (g), (h) and (i).

The lower traces of (i) and (j) illustrate changes observed at sta (4). The changes observed at this station fell into two general categories as shown here. The type shown in (i) had large fluctuations in pressure, predominately above the control, but sometimes falling below the control, locally. The type shown in (j) had a relatively smooth rise in pressure which had a peak somewhere in the vicinity of 200 μsec behind the wave front. In the experiments measuring pressure at sta (3), the pressure rise was like that shown in Fig. 4-2(d), which resembles the rise in (j) here. Only a limited number of experiments were performed measuring pressure at sta (3), so perhaps a representative sample was not obtained at that point. At sta (4), it was found that sometimes several consecutive experiments showed the character of change illustrated in (i), followed by a number of runs exhibiting the nature of change shown in (j), without any apparent change in experimental conditions. The author has no proof of the cause of the changing character, but suspects that it could be traced to local changes in current density distribution patterns. Support for this suspicion comes from an earlier set of experiments not reported here. Small coils were placed in the tube walls which were connected to an integrating circuit. These coils picked up a signal due to flux linking of the winding with currents in the gas. They were never calibrated, nor was their spacial resolution determined so the results obtained were purely qualitative. In those experiments, large fluctuations in the output of these pick-ups had a

frequency corresponding to the frequency of pressure pulses measured by a transducer several inches downstream. The conclusion was that the current patterns were interacting with a relatively uniform magnetic field causing pressure pulses of the same frequency. Similar interactions may be causing the fluctuations observed here, although the current sensitive coils were not used to detect these effects in this set of experiments.

The tendency of pressure pulses to steepen into shocks may cause pressure pulses of the type shown in (i) to coalesce or partially merge to form a pulse of the type shown in (j). The significant point to be made here, at any rate, is that both (i) and (j) show large pressure changes which fall well above the error margins shown on Fig. A3-1. Fig. 5-23 show the points for five runs for case VI giving results representative of both categories discussed here. By joining points, the oscillating or smooth rise for any run can be seen more clearly.

Fig. 4-2(k), (l) and (m) are intended to indicate the effect of initial detonation pressure on the changes observed. Only a few runs were done at 20 mm of Hg. initial pressure and no detailed theoretical solutions were performed to correspond to this case. Some qualitative comparisons can be made on the basis of governing equations. From eqn. (2.21) it can be seen that changes in u and c are directly proportional to N which equals $\sigma B (E-uB)/\rho$. From the perfect gas law, we know that density is directly proportional to pressure for a fixed temperature. Since the temperature in the wake of a detonations is effectively unchanged for different initial detonation pressures,

provided the mixture is unchanged, it follows that the term N in eqn. 2.21 is inversely proportional to the pressure upstream of the detonation. This tells us that for the same electromagnetic interactions the changes in u and c will be inversely related to the initial pressure. This trend continues in eqn. 2.19. From this it can be seen that $\frac{dp}{p} \sim \frac{dc}{c} - \frac{M}{p}$. So without doing a detailed solution, since the term M/p is much smaller than dc/c for the cases studied in detail and would not change significantly for this case, it can be concluded that a larger percentage pressure rise should be observed for lower pressures.

In Fig. 4-2(1), a large pressure pulse is observed at sta (1) for the case with $\bar{j} \times \bar{B}$ retarding the flow. Comparing the pressure at sta (4) between the control run (k) and (1), a small decrease in pressure is seen for (1).

A more dramatic change is seen at sta (4) in Fig. 4-2(m). This result parallels those of (i) and (j) but now the pressure pulse appears as a shock wave. The percent increase in pressure here is approximately double that seen in (i) and (j).

The oscilloscope traces referred to in this discussion have clearly shown that there are some very definite pressure changes observed in the flow field which are caused by the electromagnetic fields. The major changes observed may be summarized by:

1) With $\bar{j} \times \bar{B}$ retarding the flow, at current densities of about 10 amps/cm^2 and a magnetic field strength of about 1 web/m^2 , a pressure increase is observed at sta (1) about $650 \text{ } \mu\text{sec}$ after the wave front passes. These same conditions result in a point by point pressure decrease at sta (4). (Fig. 4-2(h))

2) With $\bar{j} \times \bar{B}$ pushing the flow, at average current densities of about 10 amps/cm², with a magnetic field strength of about 1 web/m², pressure increases are observed at sta (3) and sta (4). (Figs. 4-2(d), (i) and (j)).

Results obtained for smaller current densities, and for electric fields alone are also presented here. These will now be examined systematically and compared with theoretical predictions.

a) Cases I and IV (Electric Fields only)

The typical experimental results for these cases are plotted on Figs. 5-1 through 5-6. No plot is provided for sta (1) since no modification of pressure was observed and none predicted.

At sta (3), theory predicts a pressure rise of as much as 14 cm of Hg. for case I but experiments show no such rise (Fig. 5-1). Experiments for case IV show a slight pressure rise (Fig. 5-3) about 4-6 cm of Hg. at maximum. If the enthalpy added by $\bar{E} \cdot \bar{j}$ terms was lost to the tube walls or dissipated in some way, there would be no pressure change for these cases. It appears as though this happened for case I, but more energy was added in case IV and not all of it was lost, so a small change in pressure was observed. A discussion of how this added energy could be lost is provided in Appendix 7.

At sta (4), the predicted pressure rise is smaller than at sta (3). Experiments show no noticeable change for case I, but a slight rise above the control level for case IV (Figs. 5-4 and 5-6).

b) Cases II and V

A pressure increase at sta (1) after about 600μsec is noted for case V (Fig. 5-7). No such rise is seen for case II in the experiments.

Theory for case II predicts a gradual rise after 850 μ sec, but no such rise when the $\bar{E} \cdot \bar{j}$ term is set to zero in case IIA. Case VA (Fig. 5-7) still predicts a pressure rise after 840 μ sec, so good qualitative agreement, and reasonable quantitative agreement is seen between experiments and theory when enthalpy loss is allowed. Noteworthy on Fig. 5-8 is the fact that the temperature (sound speed) is still above the control level in the pressure pulse. So, having allowed all the energy added to escape, the temperature is still above normal.

It is interesting to note that the pressure pulse observed here arrives sooner than predicted. This would indicate that the particle velocity is smaller in magnitude than the sound speed by a greater amount than used in the theory. (Type II characteristics have a slope of $(1/(u-c))$ so the smaller u is, and the greater c is, the more they bend backwards. Consequently disturbances can reach sta (1) from downstream sooner.) It would seem as though wall effects have not only reduced the pressure below what is expected by ideal 1-D theory, as discussed in Chapter 4, but have also reduced the gas velocity proportionately more than the sound speed.

Based on the relations for turbulent boundary layers given by Fay³⁸, the boundary layer would close in the author's tube at a distance of about 2.8 meters behind the wave or about 1300 μ sec after the wave passes a point. The free stream is only a small fraction of the tube after 500 μ sec. (See Appendix 7) This being a non-steady flow problem, rarefaction waves originating at the wall could be propagating into the free stream, and the free stream conditions could be affected through these. This could, perhaps, account for the apparent reduction of particle velocity below what is expected from 1-D theory.

The pressure measurements at sta (3) for case II show no obvious change from the control pressure. This is in reasonably good agreement with the case IIA solution which also predicts little change from normal. The temperature for case IIA is still above normal, so the assumption that heat transfer has dissipated the added enthalpy does not lead to any ambiguities here.

Fig. 5-11 shows the pressure measured for case V at sta (3) compared to the solution for case VA. The measurements seem to indicate a slight decrease below normal after about 250 μ sec, while theory predicts first a slight decrease, then a moderate increase followed by another drop. This pressure increase coincides with a rise in sound speed due to a large suppression in particle velocity.

At sta (4), (Fig. 5-13) the pressure measurements for case II show negligible deviation from the control, which is consistent with theory for both case II or IIA.

Case V shows a definite decrease in pressure below the control, from experimental measurements at sta (4). Fig. 5-15 compares these results with theory for case VA. The theoretical curve has a slight "kink" in it which looks very much like the curve for particle velocity change. The conductivity used in these calculations started low, rose to one plateau and then rose again, much like shown in Fig. 4-8. It appears as though the change in pressure and particle velocity from the control level has been directly influenced by the conductivity distribution. Since it has not been proved that this conductivity distribution accurately depicts the one in the experiment, the emphasis, in comparing experimental results with theoretical predictions, should be placed on the trend

of the solution rather than the point by point correspondence.

With this understanding, it can be said that the experiments for case V distinctly display the features predicted in the solution for case VA which considered all the enthalpy added to be lost. The temperature, again, has not fallen appreciably below the control level at this point for case VA.

In summary for cases II and V, there is good agreement between experiments and the theoretical solutions which considered the enthalpy addition to be compensated by an equivalent loss mechanism. Since in these cases, the temperature still rose above normal in the field region, there are no ambiguities resulting from assuming this heat lost.

c) Cases III and VI ($\bar{J} \times \bar{B}$ pushing the flow)

No pressure changes were observed at sta (1) for either of these cases, and since none was predicted there is good agreement between theory and experiment at this point.

At sta (3), the pressure measurements for case II (Fig. 5-17) show very little difference from the control level. There appears to be a slight tendency toward pressures lower than the control level after about 450 μ sec, which qualitatively agrees with the case IIIA solution. Associated with this pressure drop in the solution is a decrease in sound speed below the control level. This is a little ambiguous as any mechanism for additional heat loss would not likely lower the temperature below the level at which it normally equilibrated, unless the heat transfer coefficient was altered. Discounting this possibility for the present, it would seem more reasonable that the sound speed would not drop below normal and the pressure would also be closer

to the control level. It is expected that agreement between theory and experiment would still be quite good if this were so.

This argument becomes of more importance in evaluating the results for case VI. The few experiments done at sta (3), (Fig. 5-19) for this case show a consistent rise in pressure beginning after about 100 μ sec remaining above normal for several hundred μ sec, and a drop back to normal about 400 μ sec after the wave passes, remaining around the control level thereafter. The solution for case III which includes enthalpy addition and effects of Lorentz forces, but has a lower current level than the experiments of case VI, could be used to simulate partial loss of both effects. This solution predicts a substantial increase in pressure which does not return to the control level as do the experimental results. Recalling that the turbulent boundary layer penetrates far into the tube by 500 μ sec, one would expect a higher rate of dissipation thereafter, thus perhaps explaining the deviation of experiments from this solution after several hundred microseconds.

The solution for case VIA, on the other hand introduces some ambiguities as a result of this simplified method of simulating heat loss. Since the Lorentz forces are large and no energy is added to suppress the particle velocity, it has risen several hundred m/sec above the control level. The sound speed has fallen below the particle velocity, with a corresponding temperature drop of about 1000°R below the control level. This does not seem physically possible since the energy is actually added and its rate of loss presumably would be governed, at least in part, by the rise in temperature above normal. When the temperature drops to the control level, one would expect energy losses

to be reduced to the level experienced in control runs. The enthalpy addition should therefore maintain the temperature a little above normal and perhaps suppress the particle velocity a little. Consequently, the particle velocity would not go supersonic and the pressure would not drop far below normal as predicted for case VIA.

It would seem, therefore, as though a more sophisticated way of treating heat loss would result in a closer agreement between theory and experiment.

The pressure measurements for case III at sta (4) (Fig. 5-21) gave no indication of change from the control level. This would agree with the expected solution for case IIIA at this location.

The results for case VI at sta (4) are more interesting again. (Fig. 5-23) Experiments showed pressure rises of 10 to 15% over a range of several hundred μ sec. The pressure profile did not look exactly the same for each experiment with these conditions. Two examples are shown on Fig. 4-2 (i) and (j). The reader can follow the trend of other experiments by examining the results on Fig. 5-23. The best comparison with theory available, is with the solution for case III, which, as was mentioned, could be considered a simulation of partial loss of both the effects of enthalpy addition and the effects of the Lorentz forces. Over the first 400 μ sec the experiments display a definite rise above normal, which agrees qualitatively with theory. After that there is some discrepancy as the closing boundary layer undoubtedly dissipates the effects seen in theory.

In summary, for cases III and VI. The experimentally observed pressure changes are smaller than predicted by the solutions having no

heat loss. When all the enthalpy which is added in experiments is neglected in theory, the temperature falls far below normal and now the pressure also falls below normal, a trend which is not seen in experiments. The correct solution is expected to be somewhere in between. If the heat loss were proportional to the rise in temperature above normal, the solution would more closely agree with experimental observations.

d) Wave Speed

The wave speed was only measured between two transducers, so the accuracy is not adequate to check the theory. Theory predicts negligible change, and from all measurements, no effect on the speed attributable to the fields has been observed.

A general point can be made for all cases involving magnetic fields. Hall currents were not taken into account in the theoretical solutions. A Hall parameter of about 0.66 is estimated by order of magnitude calculations in Appendix 1. Since the total current measured in experiments included Hall currents, using these current levels in the theory without compensation for Hall currents would lead to predictions of enthalpy addition and momentum changes slightly larger than could be attained, even with no dissipation. In this case, dividing the currents in the computations by a factor of 1.44 for a magnetic field strength of 1 web/m^2 would give a more accurate estimate of the effects to be expected. The Hall component of current is perpendicular to the electric field direction so it would not contribute to $\overline{\mathbf{E}} \cdot \overline{\mathbf{j}}$ enthalpy addition. It is also parallel to the axis of the tube so the resulting $\overline{\mathbf{j}} \times \overline{\mathbf{B}}$ forces would be at right

angles to the axis, giving no contribution to momentum changes in the x direction unless through modifying the boundary layer.

It is nevertheless not likely that the discrepancy between idealized, no-loss theory and experiment can be accounted for in terms of Hall effects.

CHAPTER 6

CONCLUSIONS AND SUGGESTIONS FOR FUTURE RESEARCH

6.1 Conclusions

a) Theoretical Predictions

Analytical solutions for the one-dimensional non-steady model proposed by the author, using electric field and current distributions obtained from experimental results, have predicted some definite trends for modification of the flow field for the three orientations of electric and magnetic fields under study. The three orientations under consideration are electric fields only, electric fields plus magnetic fields which result in Lorentz forces which retard the gas motion and electric fields plus magnetic fields which result in Lorentz forces which push the gas. These field conditions were examined to determine their effects on particle velocity, sound speed and pressure in regions upstream of the field, within the field and downstream of the field. The trends predicted are as follows.

All three field orientations would produce some pressure rise in the region upstream of the field, but the combination of electric fields and Lorentz forces which retard the gas motion would produce a considerably larger pressure rise here than either of the other field orientations. Correspondingly, the pressure rise is noticed nearer the wave front for this case than for the other two.

Within the field region, all three field orientations would produce some pressure rise, but the combination of electric fields and Lorentz

forces which push the gas would produce a greater pressure rise than either of the other two. In the transition from the field region to the region downstream of the field, the pressure would generally decrease, and again the case which had a combination of electric fields and Lorentz forces which push the gas would maintain the highest pressure in the downstream region.

For all three of these orientations of fields, the major changes produced by electromagnetic fields were far enough from the wave front so that less than 1 per cent change in detonation wave speed was predicted.

Heat loss to the tube walls was simulated by considering the effect of having the $\overline{\mathbf{E}} \cdot \overline{\mathbf{j}}$ enthalpy addition just balanced by an unspecified loss mechanism, so no net enthalpy was added. From these solutions, it could be seen that the effect of energy losses was to generally reduce the changes brought about by the fields. Even with all the added energy lost, the case with Lorentz forces retarding the flow still maintained temperatures generally above the level of control runs within the field region and still produced a pressure rise upstream of the field region (although reduced in magnitude). In the transition from the field to the region downstream, the general trend of reducing pressures resulted in a pressure level below that for control runs (in this downstream region) for this case with Lorentz forces retarding the flow. When all the added energy was considered lost (in the case with Lorentz forces pushing the gas) the temperature was observed to fall far below the level it maintained in control runs within the field region, resulting in pressures far below normal. The fact that the temperature fell far below normal

for this case, appears to make the trial assumption of all added energy lost an ambiguous one for this case.

b) Experimental Observations

Experimental pressure measurements simultaneously obtained from two pressure transducers (one upstream of the field, the other in the field or downstream of the field) were presented and examined for trends of changes. It was observed that there was a definite rise of pressure at the station upstream of the field for the case with Lorentz forces retarding the gas motion. The magnitude of this rise was seen to increase as the current density in the field region was increased. No noticeable change was observed here for the other two orientations of fields.

At the station in the field region, a small pressure rise was observed for the case with electric fields only, but of these three orientations, the greatest rise above normal was seen for the case which had Lorentz forces pushing the gas.

At the station downstream of the field, the greatest pressure rise above normal was again observed for the case which had had Lorentz forces pushing the gas within the field. These pressure rises were observed to be as much as 20 per cent above normal. The case which had had the Lorentz forces opposing the gas motion within the field exhibited pressures decidedly below the normal level at this downstream position.

Within experimental accuracy no changes were observed in the detonation wave speed in the experiments.

c) Comparison of theory and experiment

In comparing theory and experiment, it can be seen that the prediction of maximum pressure rise above normal in the region upstream of the field, for the case with Lorentz forces retarding the flow, has been verified in experiments. The smaller changes predicted here for other orientations of fields must have been too small to detect in experiments.

The prediction of greatest pressure rise above normal within the field for the case having Lorentz forces pushing the gas was also verified. The trend of falling pressure in the transition from the field region to the region downstream was seen most strongly in the case where the Lorentz forces were opposing the flow, which is also in agreement with theory. Observation of the largest pressure rise above normal at this downstream station for the case which had had Lorentz forces pushing the flow was also in agreement with theory.

The fact that no change in the detonation wave speed was observed for these experiments was also, within experimental accuracy, a verification of the theoretical predictions.

d) Evaluation of simulated heat loss

The experimental results for the case with Lorentz forces opposing the flow was in better quantitative agreement with the theoretical solutions with simulated heat loss than for the ones with no losses. For the former case, the temperature within the field region as seen in solutions was higher than in control solutions even with the added energy loss, so it was not considered unreasonable that all this added energy could be lost. For the case with Lorentz forces pushing the gas, the

solution, allowing all added energy to be lost predicted temperatures far below normal with resulting pressures far below normal. This large pressure drop was never observed in experiments and the fact that the predicted temperatures dropped so far below normal gave evidence that the assumption which allowed all the added energy to be lost was not correct. The experimentally observed rise in pressure was smaller than predicted when no losses were considered, however, so it was concluded that some losses occurred in this case too, but not all the added energy was lost.

The general conclusion that energy losses to tube walls could have a substantial effect in reducing the pressure in the flow field was first arrived at by comparing results obtained by the author in his tube, and published results by other investigators in various sized tubes, to the theory of a progressive rarefaction wave, which has no allowance for tube diameter.

e) Shock interaction with detonation

In a study, somewhat related to the general thesis (Appendix 6), it was demonstrated that when large currents are allowed to concentrate in a small region in a transverse magnetic field, shock waves are formed. This method was used to generate shock waves behind the wave front. The detonation wave was observed to become overdriven when these shocks overtook it, resulting in propagation speeds several hundred m/sec above their usual C-J speed. This result is again qualitatively explained on the basis of a one-dimensional model.

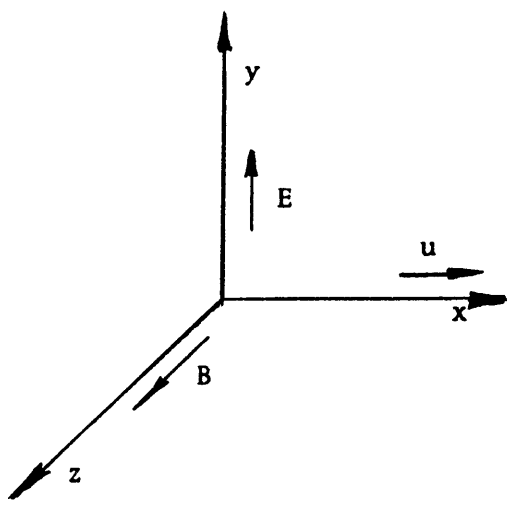
6.2 Suggestions for Future Research

Many of the arguments used to explain experimental results ended in the conclusion that energy losses to the tube walls had a great effect on the flow field. Heat transfer measurements to the tube walls which could identify the mechanism of loss as well as the magnitude would significantly enhance knowledge in this area. A theoretical model employing two-dimensional concepts to determine loss rates, combined with the one-dimensional nonsteady formulation to describe the flow field would appear to be a good approach for analysis. Extending this study to the case with electromagnetic interactions would presumably lend support to inferences made in this thesis.

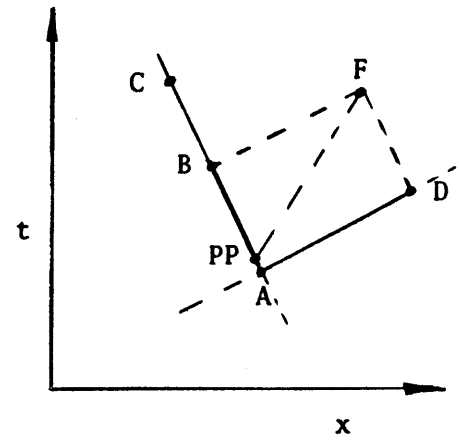
Although many interesting effects were observed in these experiments, the slow increase of conductivity behind the wave partly confined the interesting results to regions too far from the wave front to alter its character. The author recommends performing similar experiments with a more sophisticated method of seeding which could result in a more rapid increase in conductivity. Large current densities immediately behind the front should cause large changes in wave speed. Such effects are predicted with the theory used in this thesis for the above mentioned conditions but were not observed in experiments, nor were they predicted for the field variations obtained in experiments.

The experiments reported in appendix 6 were only of a preliminary nature but gave promise of an interesting area of research. Studying the actual interaction of the shock and detonation waves by schlieren techniques may prove interesting. It would also be of interest to see how well one-dimensional theory could predict changes in wave characteristics.

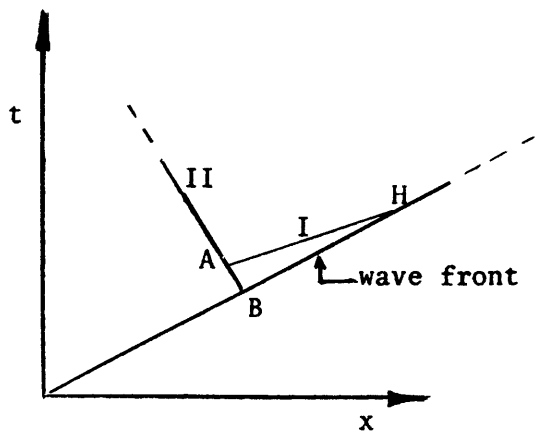
Qualitative comparisons were in agreement here, but careful quantitative comparisons were not made. It would be of interest to obtain structure measurements in the newly formed wave, after the shock overtakes the detonation, to see if the location of the region of chemical reaction had shifted from its former location relative to the von Neumann spike or not.



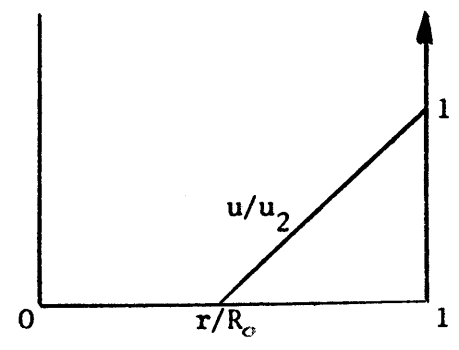
(a)
Co-ordinate system



(b)
Solving for general point



(c)
Solving for hot boundary of wave



(d)
Rarefaction wave

FIGURE 2-1 (a), (b), (c), (d)

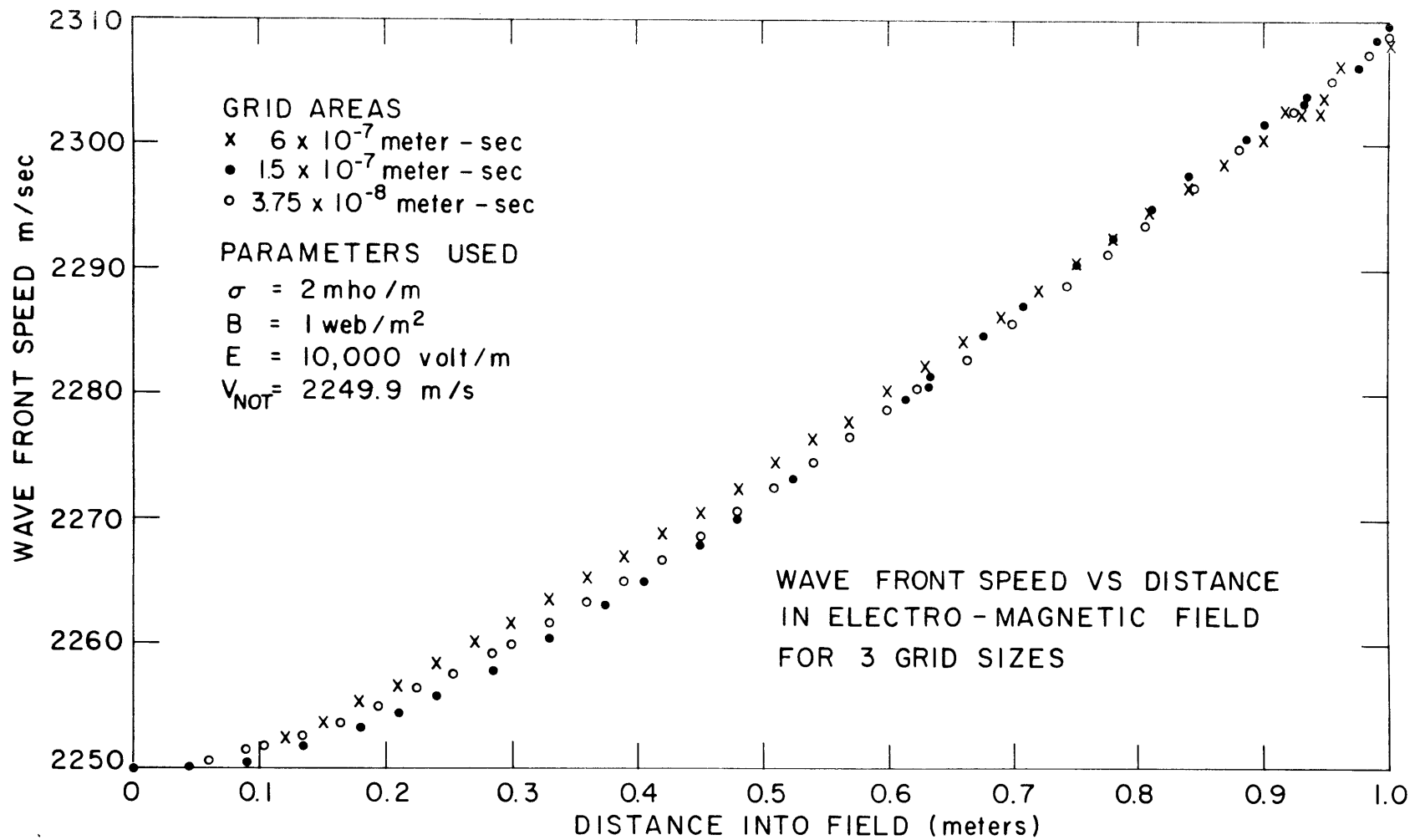


FIGURE 2-2

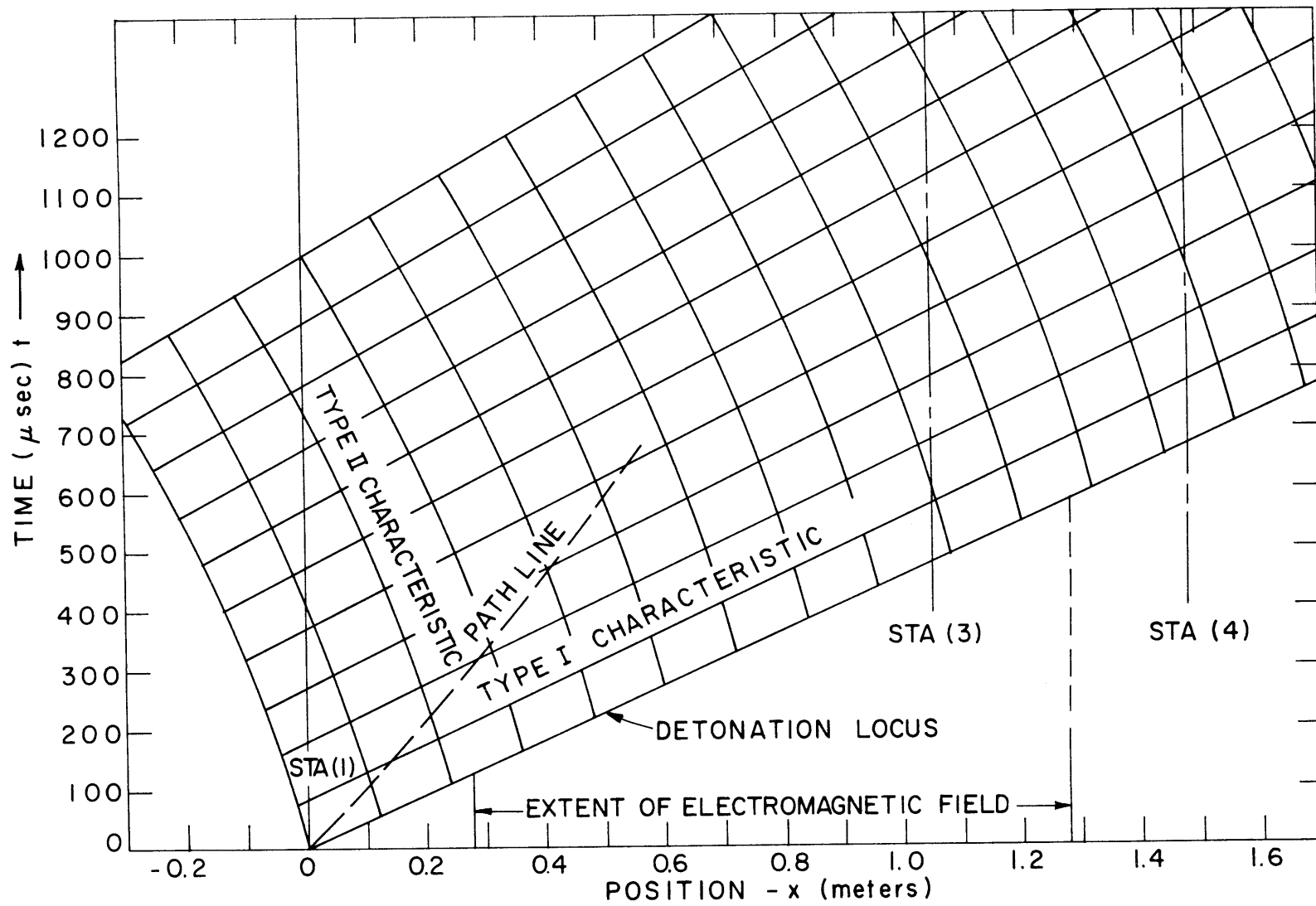


FIGURE 2-3 X-T DIAGRAM FOR NO ELECTROMAGNETIC FIELDS

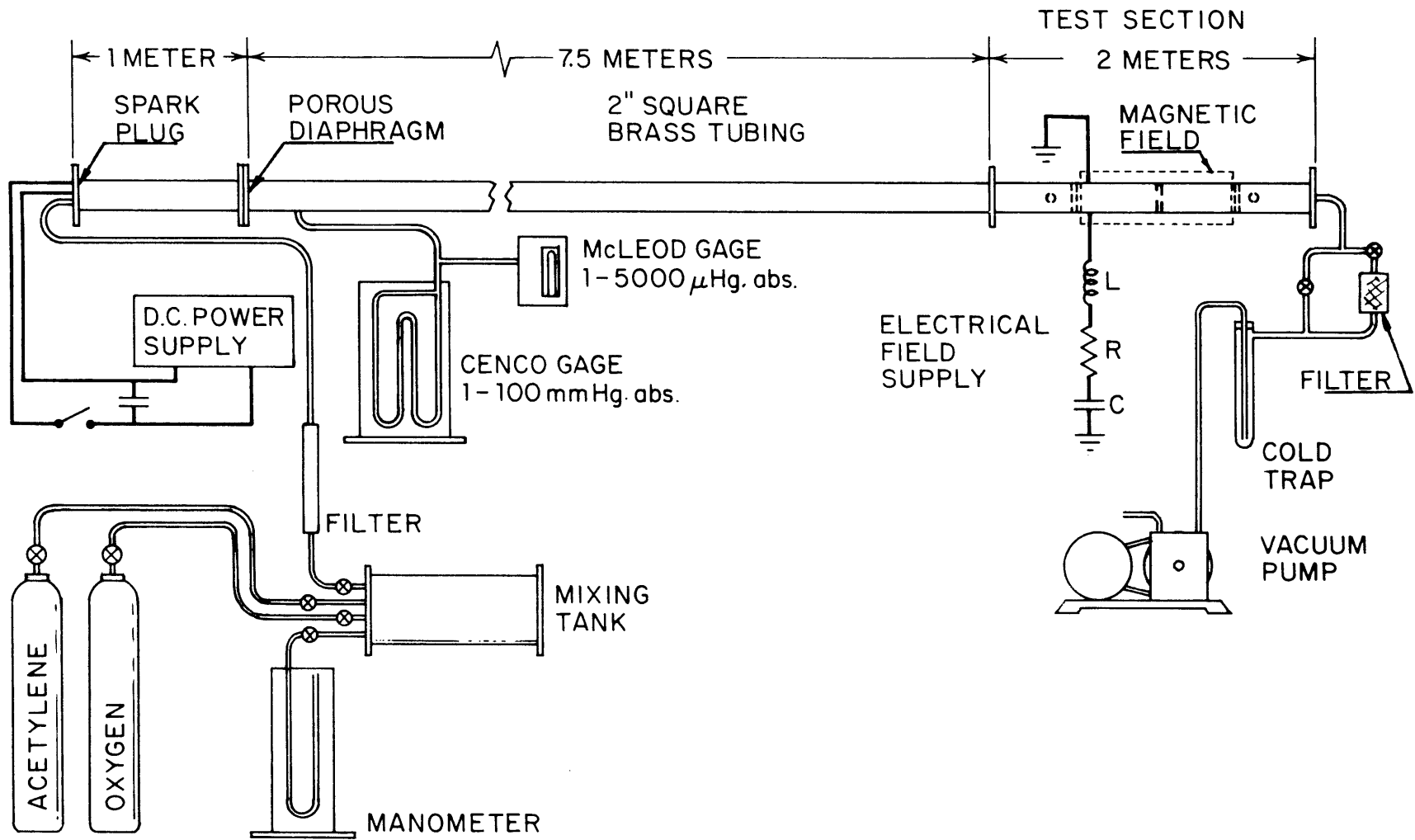


FIGURE 3-1 DETONATION TUBE SCHEMATIC

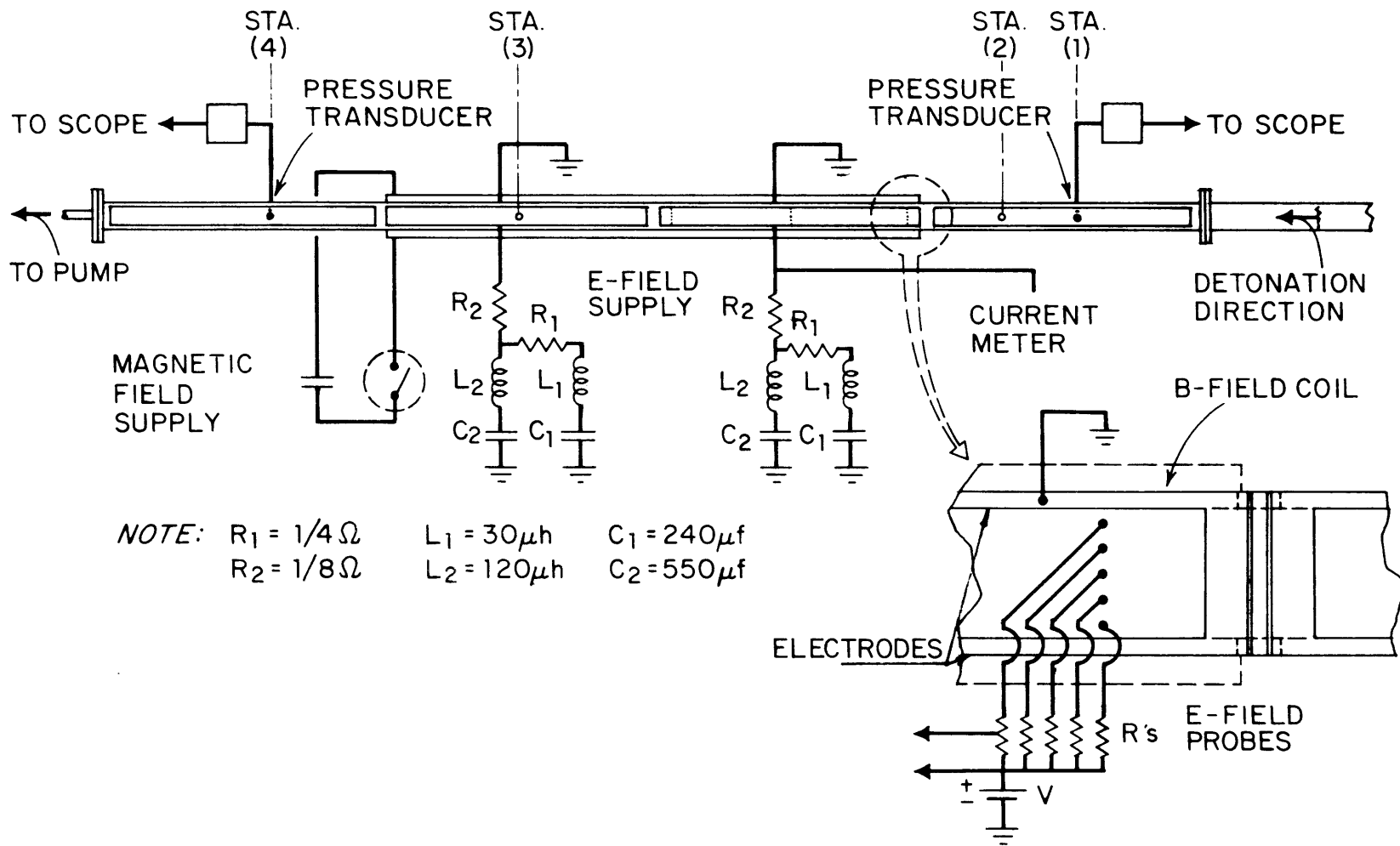


FIGURE 3-2 TEST SECTION SCHEMATIC

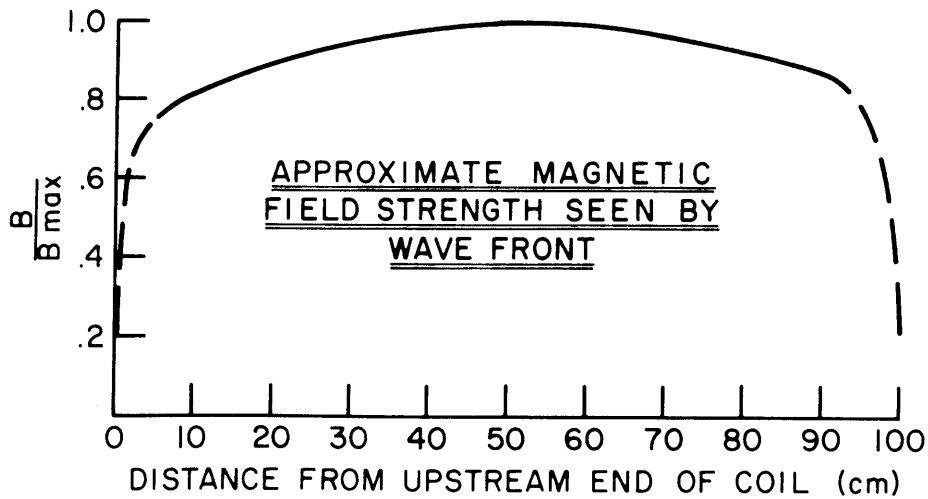
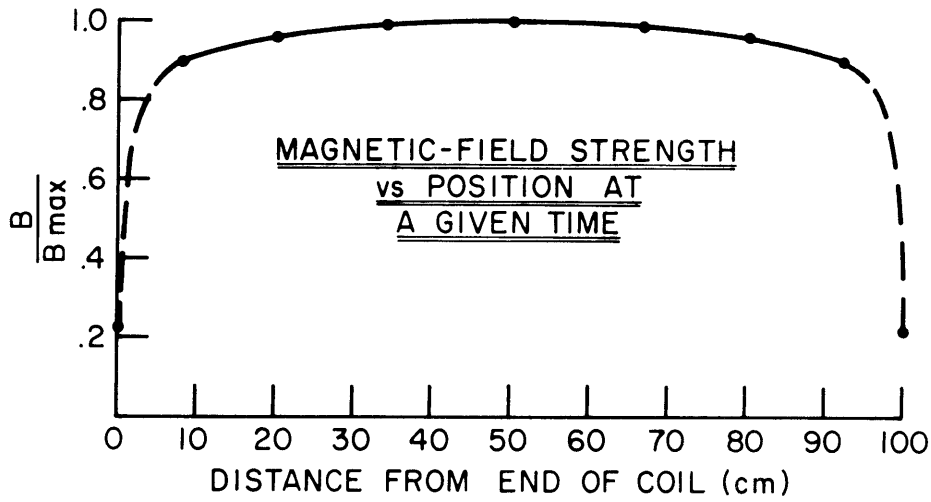
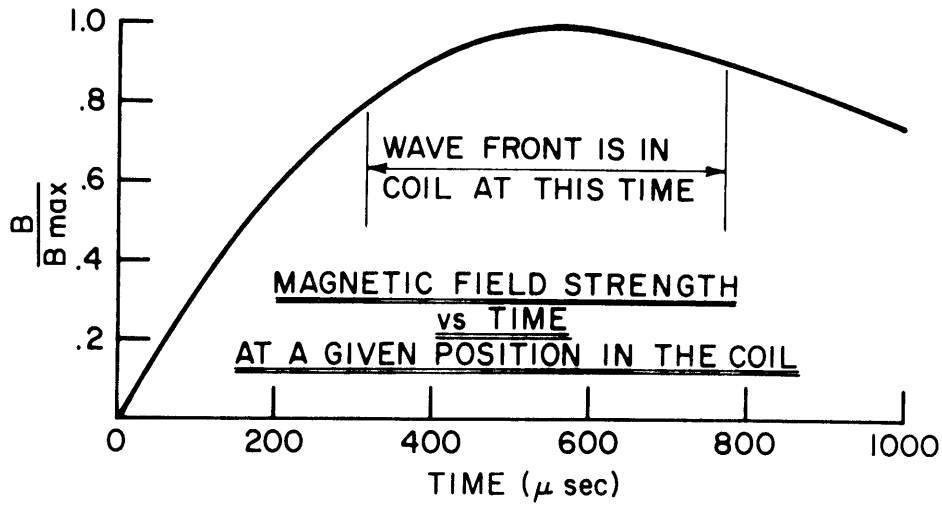


FIGURE 3-3

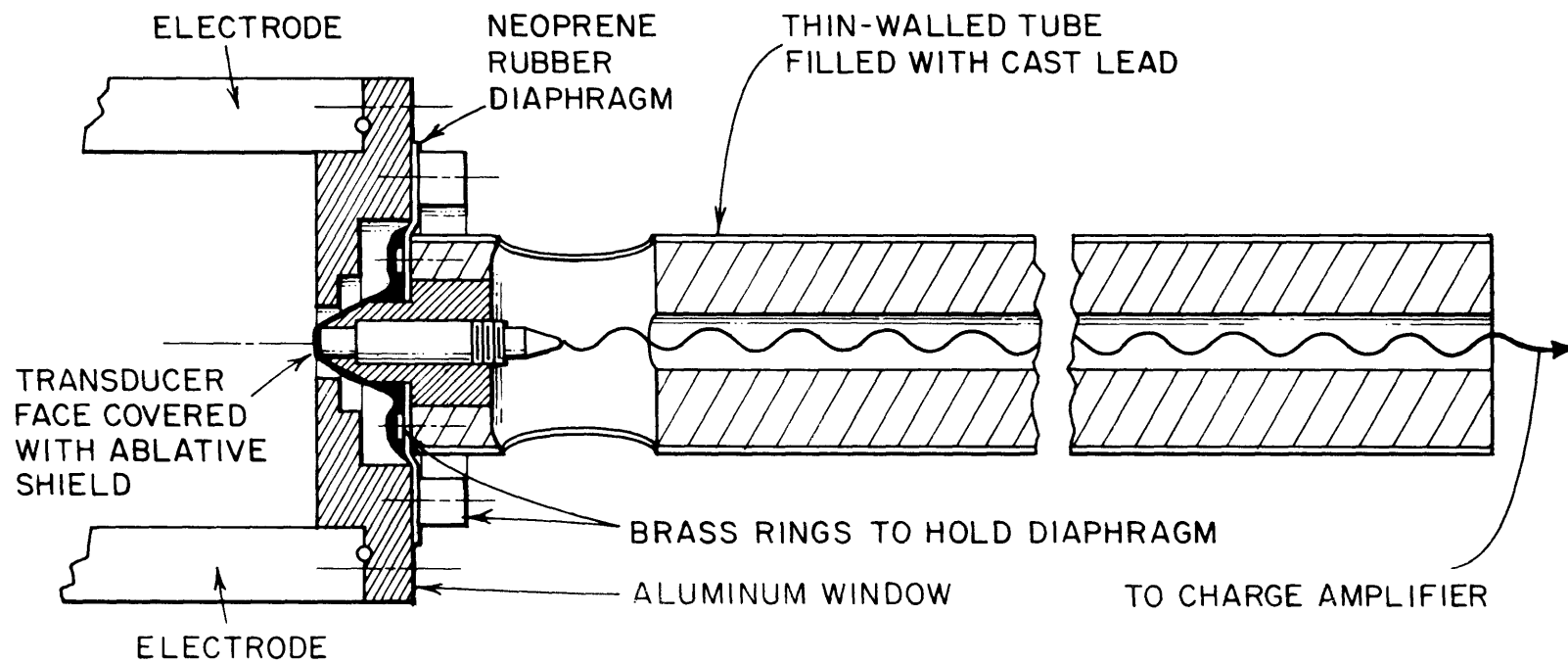
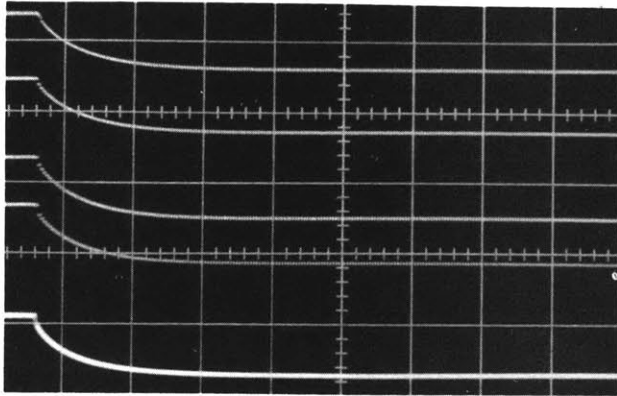
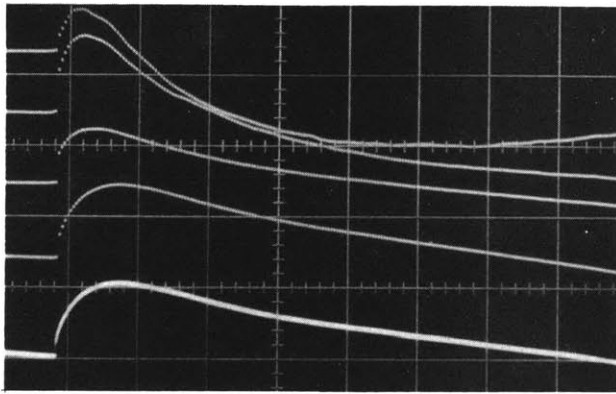


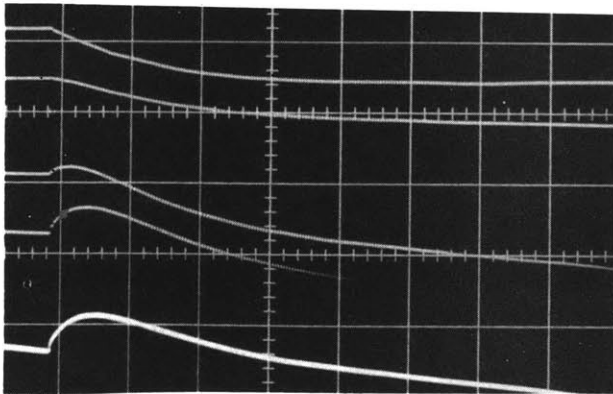
FIGURE 3-4 TRANSDUCER ISOLATION MOUNT, CUT-AWAY VIEW



a) no voltage on electrodes
90 volt battery



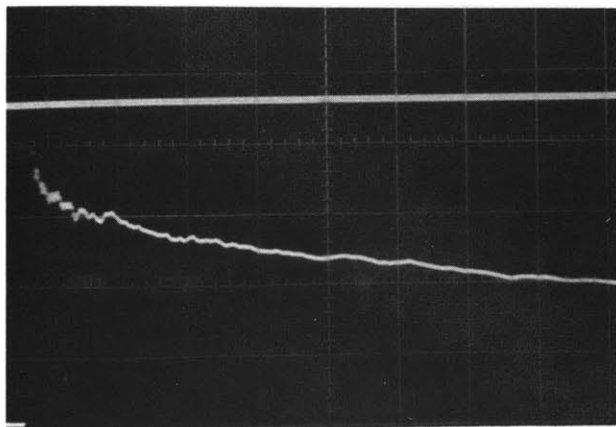
b) 500 volts initially on electrodes
no B field
90 volt battery



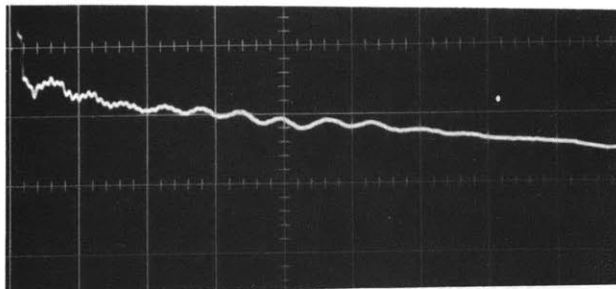
c) 500 volts initially on electrodes
no B field
180 volt battery

FIGURE 4-1 ELECTRIC FIELD PROBE TRACES

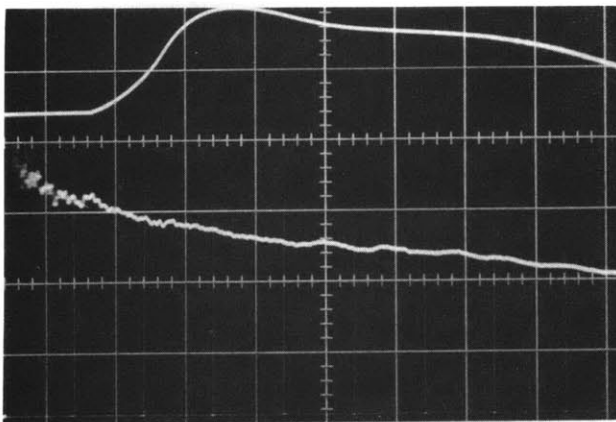
Output of electric field probes in order top to bottom
Top - nearest cathode
Bottom - nearest anode



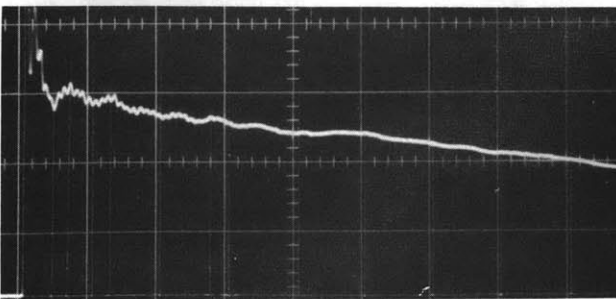
40 mm Hg initial pressure
 a) Control - no fields
 Current and B field monitor
 Pressure sta (1)
 27 cm Hg/cm on scale
 100 μ sec/cm
 2 filters in series on output
 of amplifier



Pressure at sta (3)
 27 cm Hg/cm on scale
 100 μ sec/cm
 2 filters on output

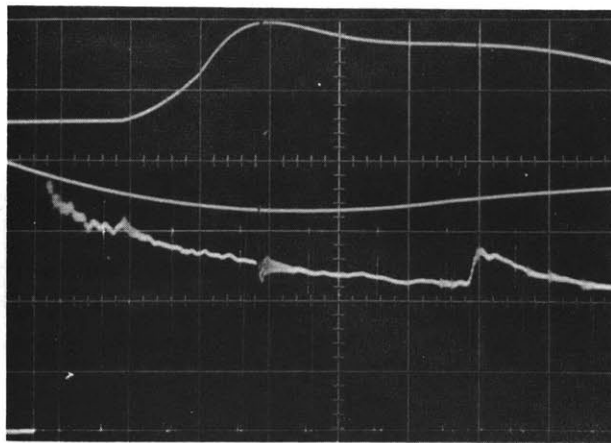


40 mm Hg initial pressure
 b) Case IV (E field only)
 Current to 1st electrode
 1420 amps/cm on scale
 100 μ sec/cm
 Pressure at sta (1)
 27 cm Hg/cm on scale
 100 μ sec/cm
 1 filter on output

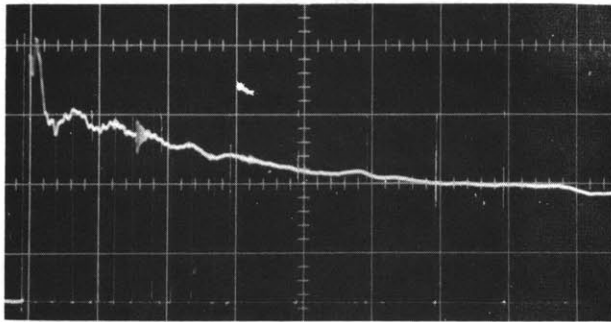


Pressure at sta (3)
 27 cm Hg/cm on scale
 100 μ sec/cm
 2 filters on output

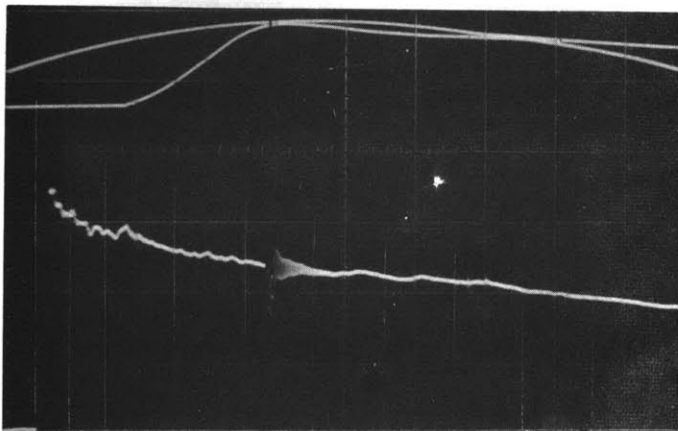
FIGURE 4-2 (a) and (b) SAMPLE OSCILLOSCOPE TRACES
 All runs are with stoich $C_2H_2 + O_2$



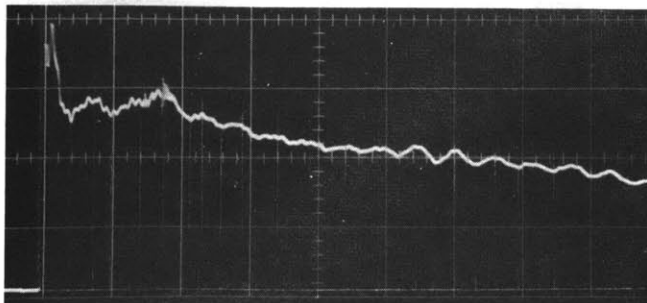
40 mm Hg initial Pressure
 c) Case V ($j \times B$ retarding)
 Current to 1st electrode
 1420 amps/cm on scale
 100 μ sec/cm sweep
 B field monitor
 Pressure sta (1)
 27 cm of Hg/cm on scale
 100 μ sec/cm
 2 filters on output



Pressure at sta (3)
 27 cm Hg/cm on scale
 100 μ sec/cm
 2 filters

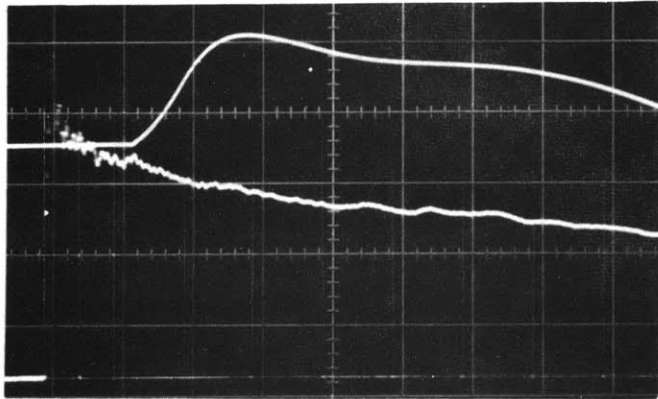


40 mm Hg initial Pressure
 d) Case VI ($j \times B$ pushing)
 B field monitor
 Current to 1st electrode
 1420 amps/cm on scale
 100 μ sec/cm sweep
 Pressure sta (1)
 27 cm Hg/cm on scale
 100 μ sec/cm sweep
 2 Filters

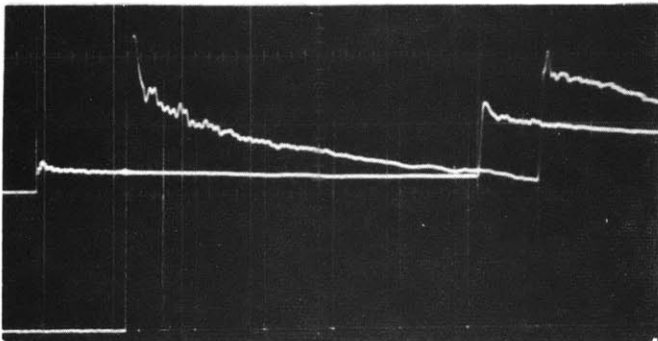


Pressure sta (3)
 27 cm Hg/cm on scale
 100 μ sec/cm sweep
 2 filters

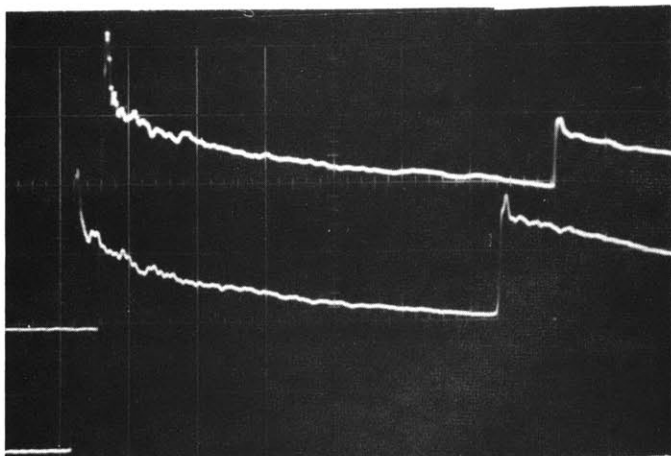
FIGURE 4-2 (c) and (d) SAMPLE OSCILLOSCOPE TRACES



40 mm Hg initial Pressure
 e) Case IV (E field only)
 Current to 1st electrode
 1420 amps/cm on scale
 100 μ sec/cm sweep
 Pressure sta (1)
 27cm Hg/cm on scale
 100 μ sec/cm sweep
 1 filter on output

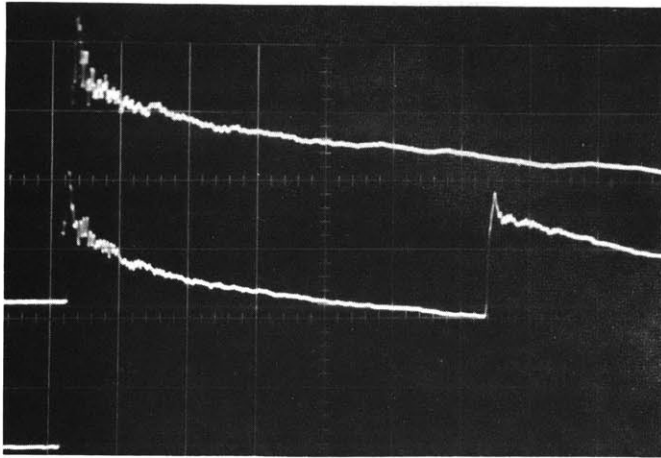


wave speed - 2280 m/sec
 Sum of pressures at sta (1) and (4)
 Pressure sta (4)
 27 cm Hg/cm on scale
 100 μ sec/cm sweep
 2 filters
 2nd rise is reflected shock



40 mm Hg initial pressure
 f) Control - no fields
 Pressure sta (1)
 27 cm Hg/cm on scale
 100 μ sec/cm sweep
 2 filters
 Plus: Pressure sta (4)
 108 cm Hg/cm on scale
 100 μ sec/cm
 2 filters
 Wave speed 2210 m/sec
 Pressure sta (4)
 27 cm Hg/cm on scale
 100 μ sec/cm
 2nd rise is reflected shock

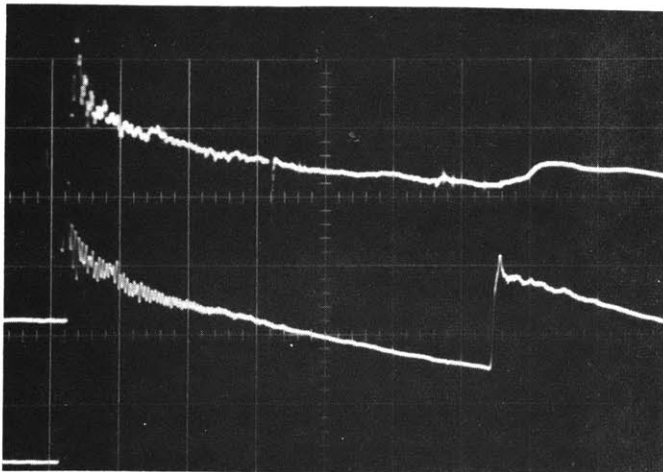
FIGURE 4-2 (e) and (f) SAMPLE OSCILLOSCOPE TRACES



40 mm initial pressure

g) Control - no fields
 Pressure sta (1)
 27 cm Hg/cm on scale
 100 μ sec/cm sweep
 1 filter

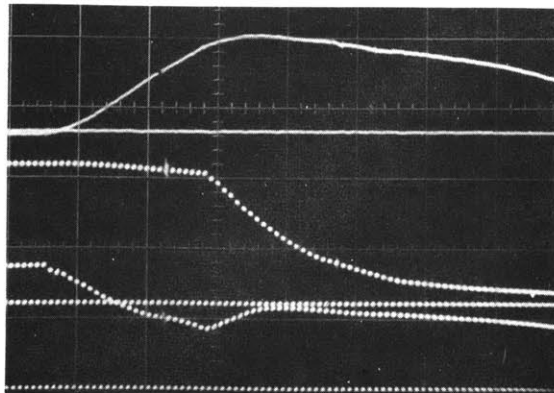
Pressure sta (4)
 27 cm Hg/cm on scale
 100 μ sec/cm sweep
 1 filter



40 mm Hg initial Pressure

h) Case V (J x B retarding flow)
 Pressure sta (1) only
 27cm Hg/cm on scale
 100 μ sec/cm sweep
 1 filter

Pressure sta (4)
 27 cm Hg/cm on scale
 100 μ sec/cm sweep
 1 filter

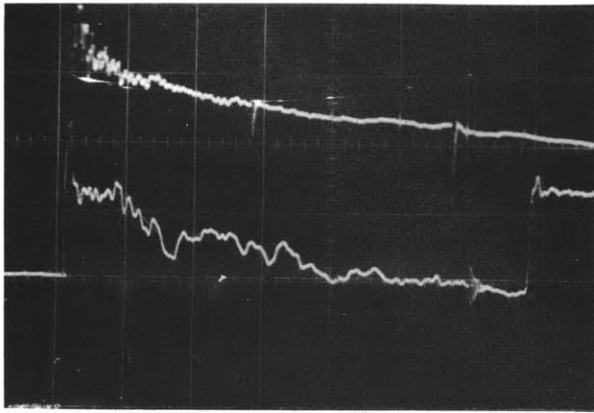


Current to 1st electrode
 1420 amps/cm on scale
 100 μ sec/cm sweep

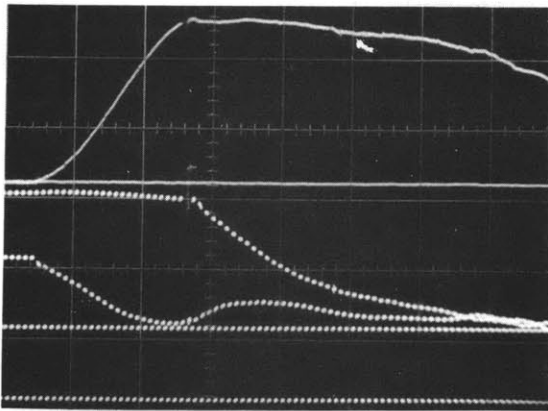
Voltage on 2nd electrode
 500 volt/cm; 100 μ sec/cm

Voltage on 1st electrode
 500 volt/cm; 100 μ sec/cm

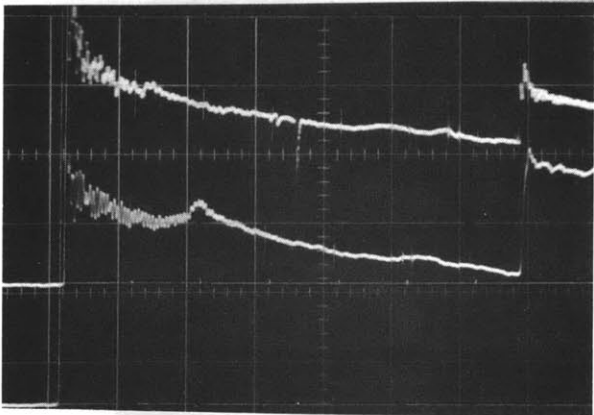
FIGURE 4-2 (g) and (h) SAMPLE OSCILLOSCOPE TRACES



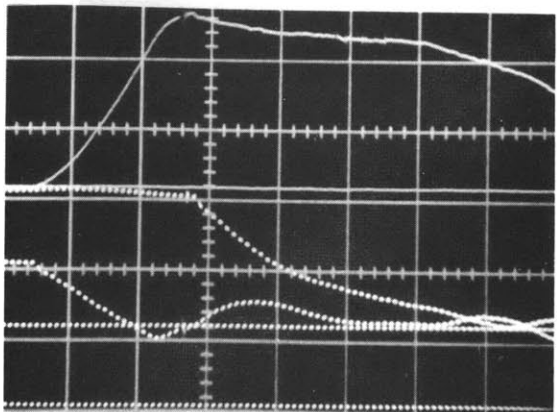
40 mm Hg initial pressure
 i) Case VI (j x B pushing flow)
 Pressure sta (1)
 27 cm Hg/cm on scale
 100 μ sec/cm sweep
 1 filter
 Pressure sta (4)
 27 cm Hg/cm on scale
 100 μ sec/cm sweep
 2 filters
 2nd sharp rise is reflected shock



Current to 1st electrode
 710 amps/cm on scale
 100 μ sec/cm sweep
 Voltage on 2nd and 1st electrode
 500 volt/cm
 100 μ sec/cm sweep

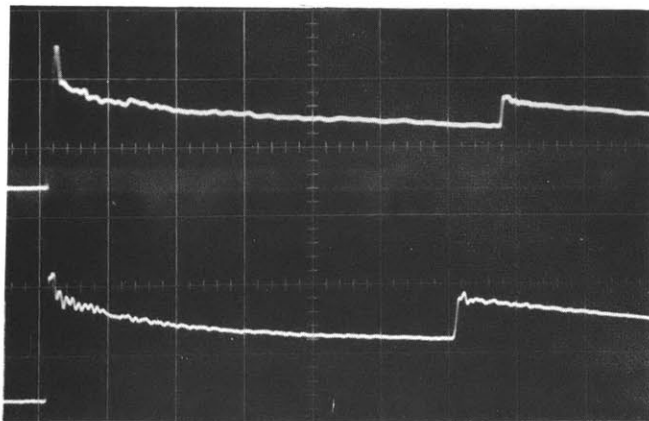


40 mm initial pressure
 j) Case VI (j x B pushing flow)
 Pressure sta (1) plus sta (4)
 Sta (1) - 27 cm Hg/cm on scale
 Sta (4) - 108 cm Hg/cm on scale
 100 μ sec/cm sweep
 1 filter on each
 Wave speed 2210 m/sec
 Pressure sta (4) only
 27cm Hg/cm on scale
 100 μ sec/cm sweep
 1 filter
 2nd sharp rise is reflected shock



Current 1st electrode
 710 amps/cm on scale
 100 μ sec/cm sweep
 Voltage on 2nd and 1st electrode
 500 volt/cm
 100 μ sec/cm sweep

FIGURE 4-2 (i) and (j) SAMPLE OSCILLOSCOPE TRACES



20 mm Hg initial pressure

k) Control - no fields

— Pressure: sta (1) and sta (4)

Sta (1) - 27 cm Hg/cm on scale

Sta (4) - 108 cm Hg/cm on scale

100 μ sec/cm

2 filters

Wave speed - 2230 m/sec

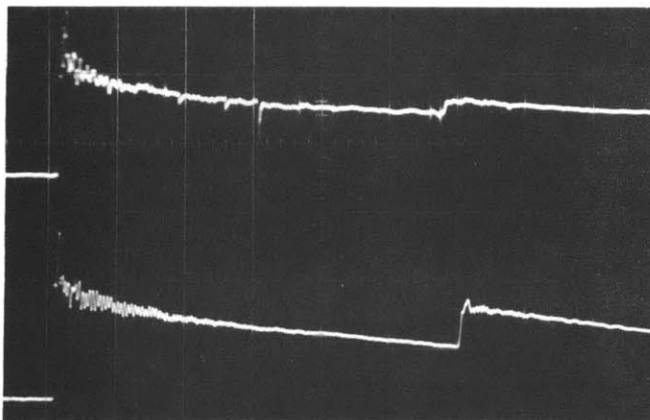
— Pressure: sta (4) only

27 cm Hg/cm on scale

100 μ sec/cm sweep

2 filters

2nd peak is reflected shock



20 mm Hg initial pressure

1) J x B retarding flow

1000 volts initially on electrodes

-1 web/m² B field

— Pressure: sta (1) only

27 cm Hg/cm on scale

100 μ sec/cm sweep

1 filter

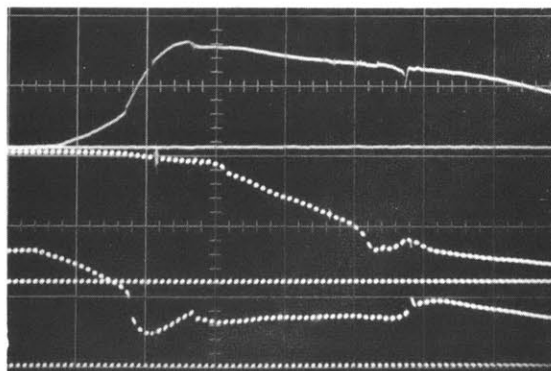
— Pressure sta (4) only

27 cm Hg/cm on scale

100 μ sec/cm sweep

1 filter

2nd peak is reflected shock



— Current to 1st electrode

1420 amps/cm on scale

100 μ sec/cm sweep

— Voltage 2nd and 1st electrode

500 volt/cm

100 μ sec/cm sweep

FIGURE 4-2 (k) and (1) SAMPLE OSCILLOSCOPE TRACES

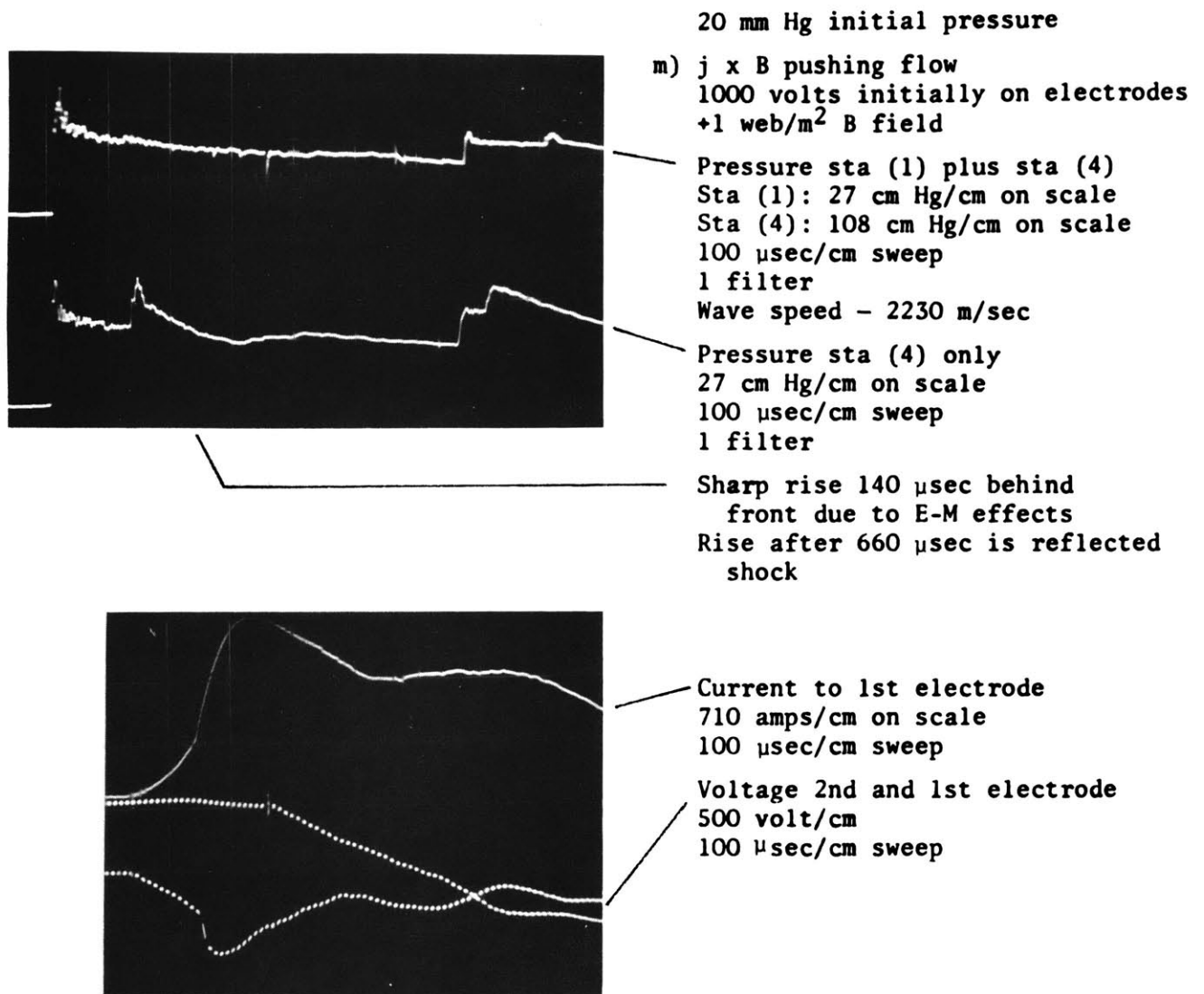


FIGURE 4-2 (m) SAMPLE OSCILLOSCOPE TRACES

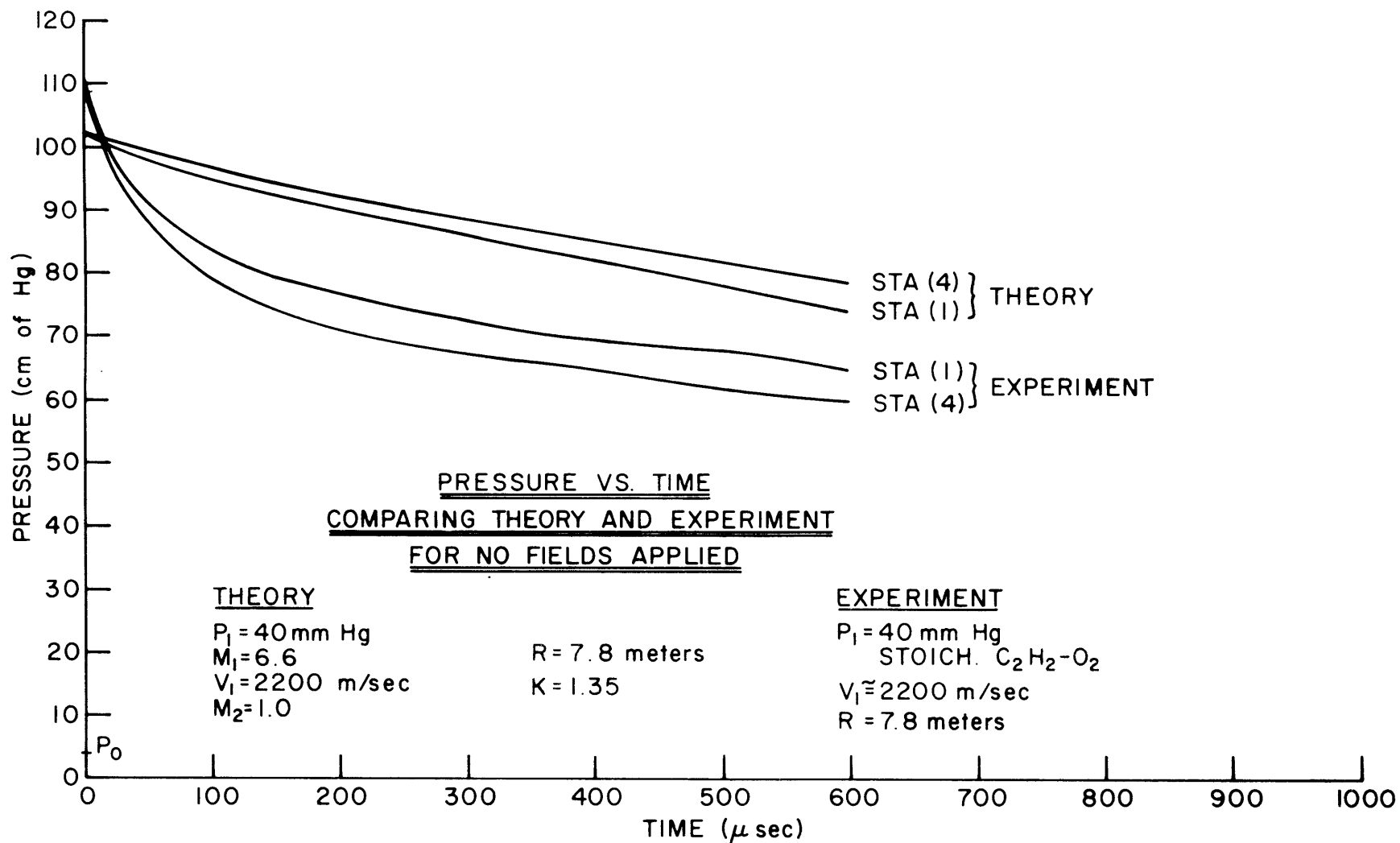


FIGURE 4-3

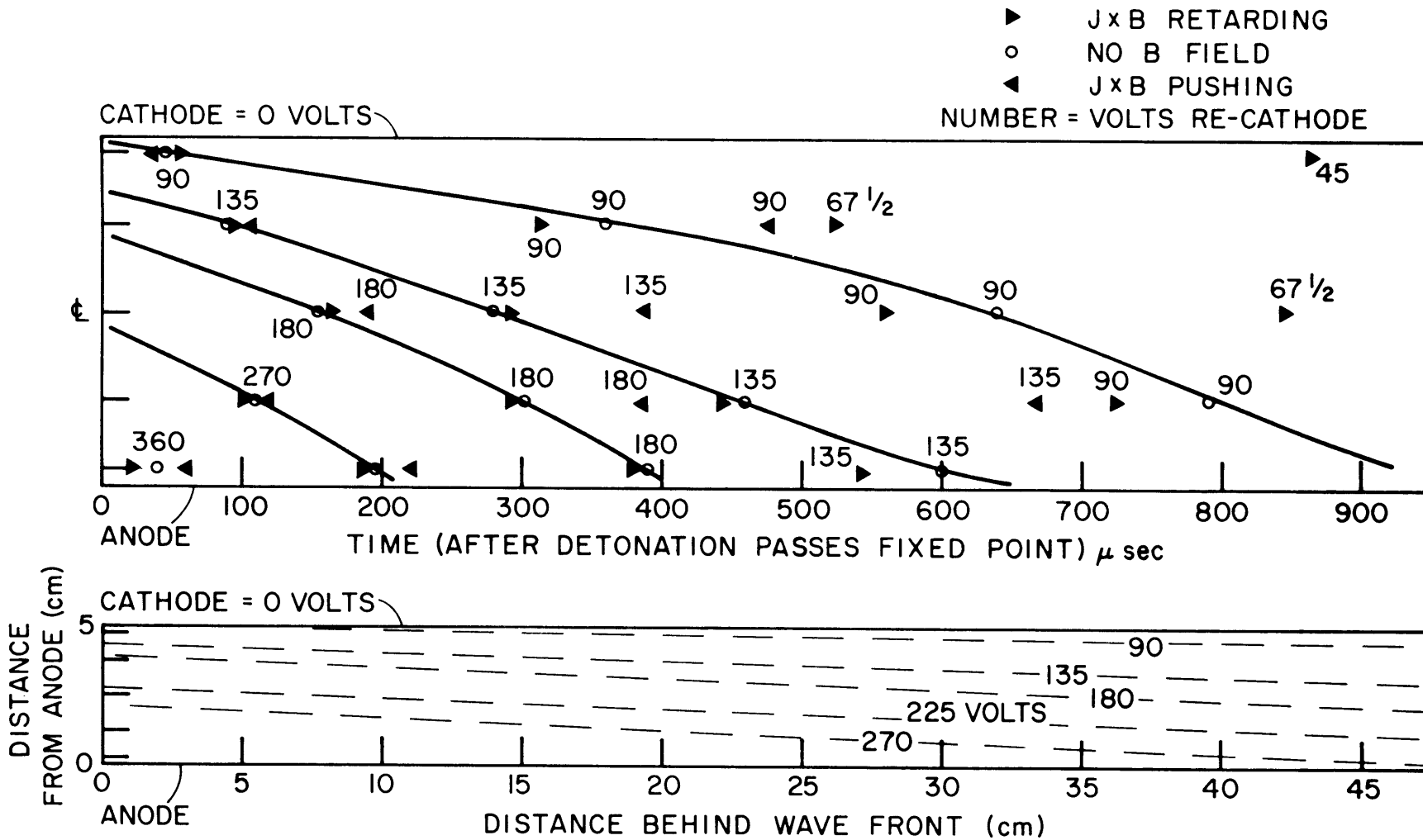


FIGURE 4-4 EQUAL POTENTIAL LINES, 3.5 cm FROM FRONT END OF ELECTRODE 500 VOLTS INITIAL VOLTAGE ON ANODE, 1 WEBER/m² APPLIED B FIELD

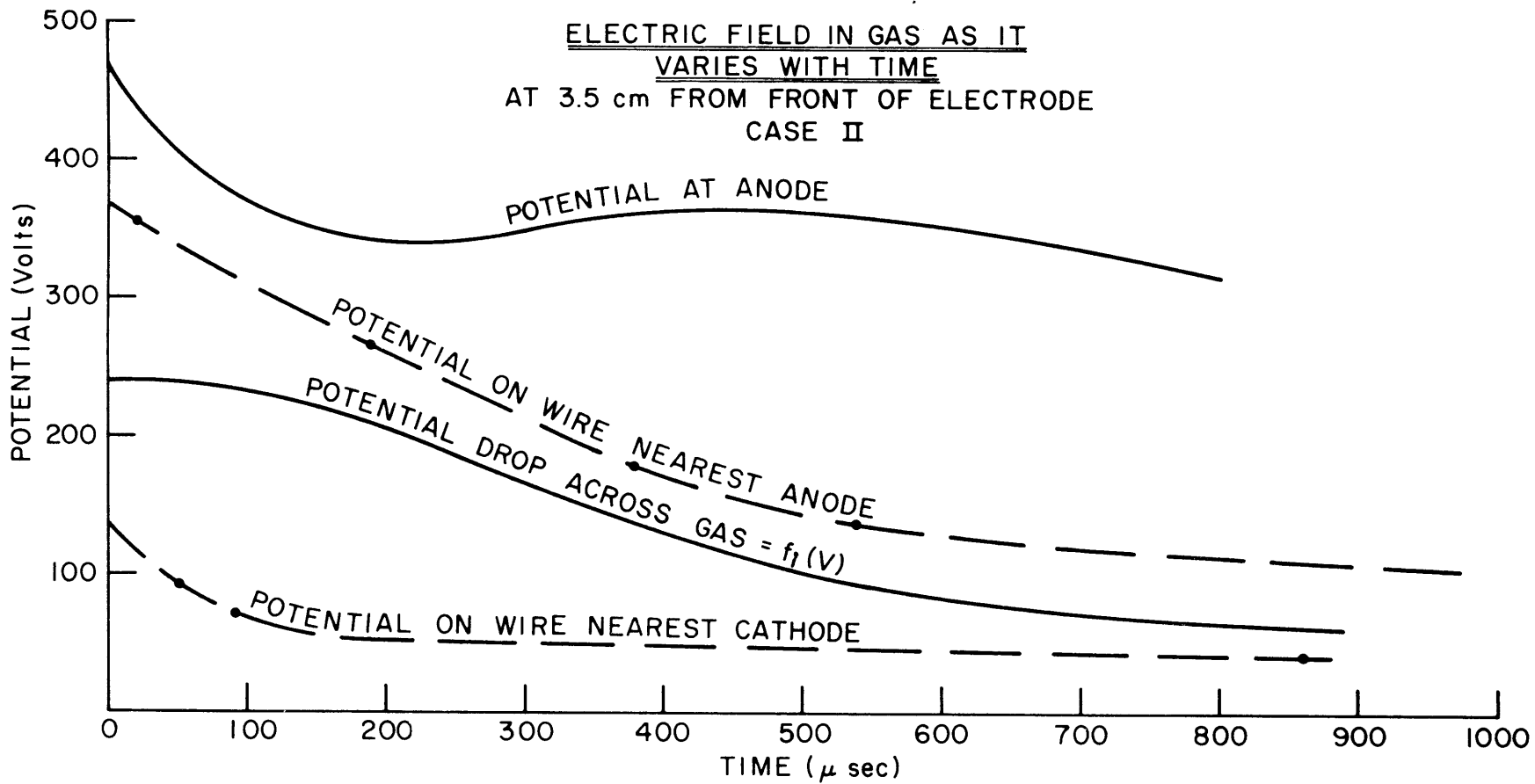


FIGURE 4-5

ELECTRIC FIELD IN GAS
AS IT VARIES WITH TIME
AT CENTER OF FIRST ELECTRODE
CASE II

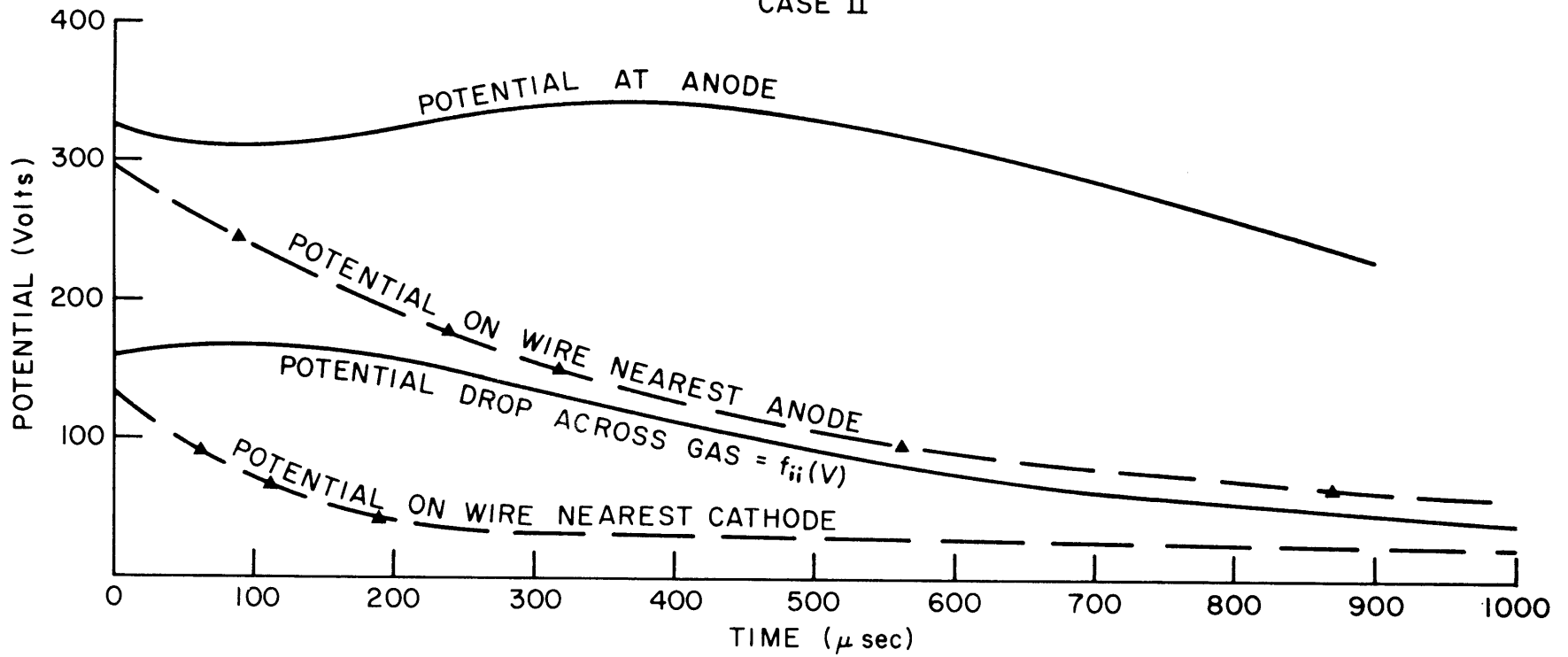


FIGURE 4-6

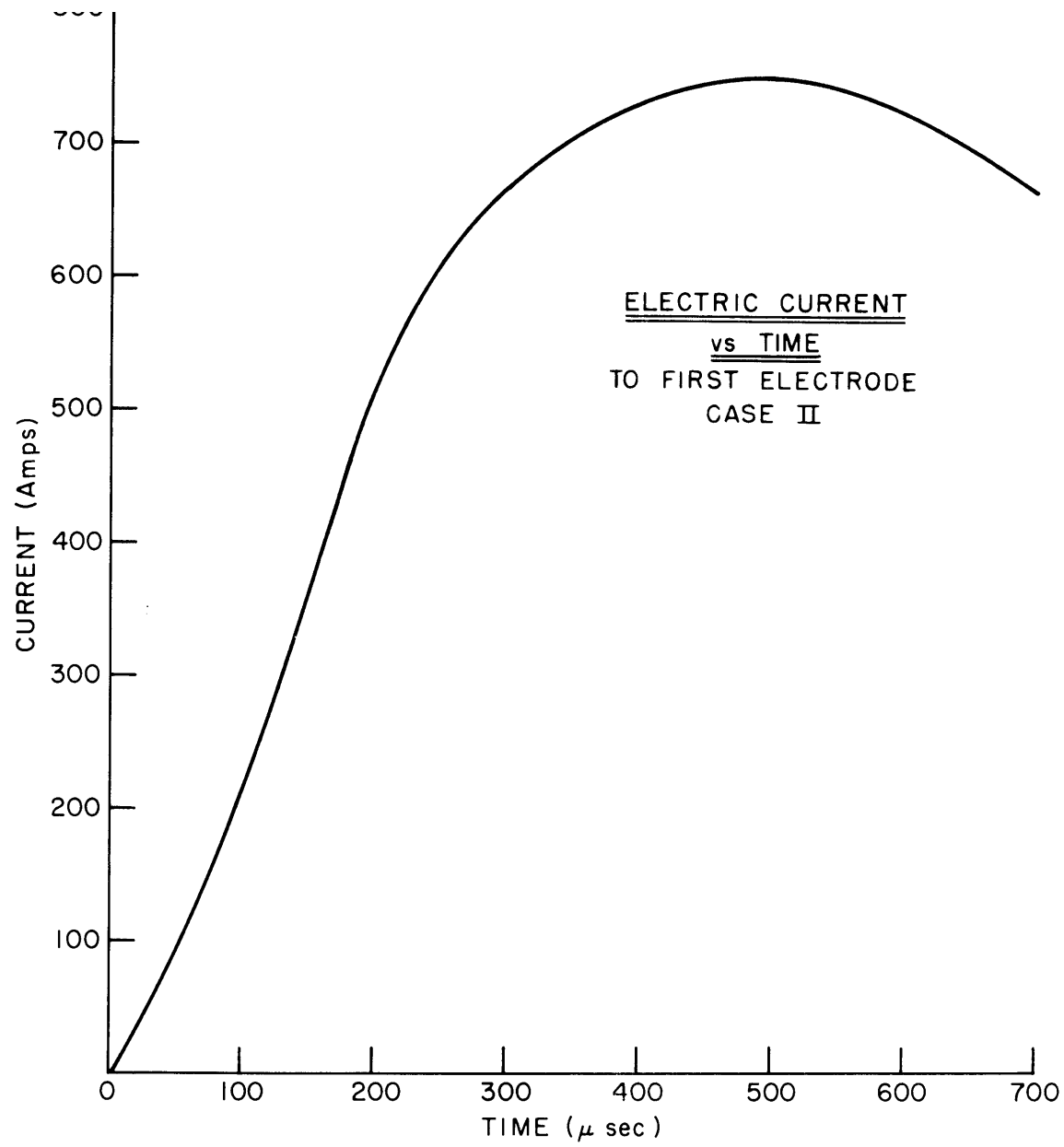


FIGURE 4-7

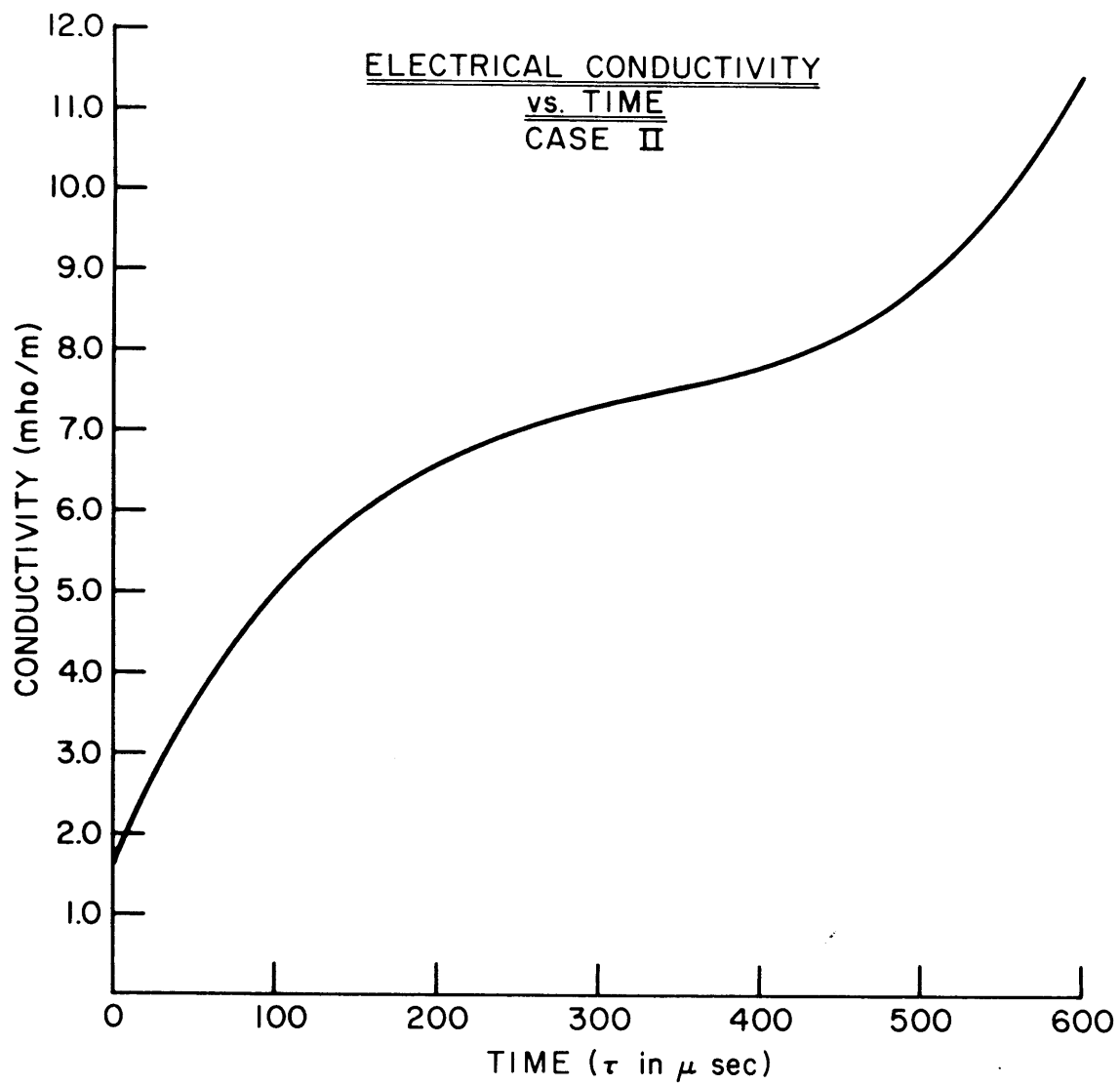


FIGURE 4-8

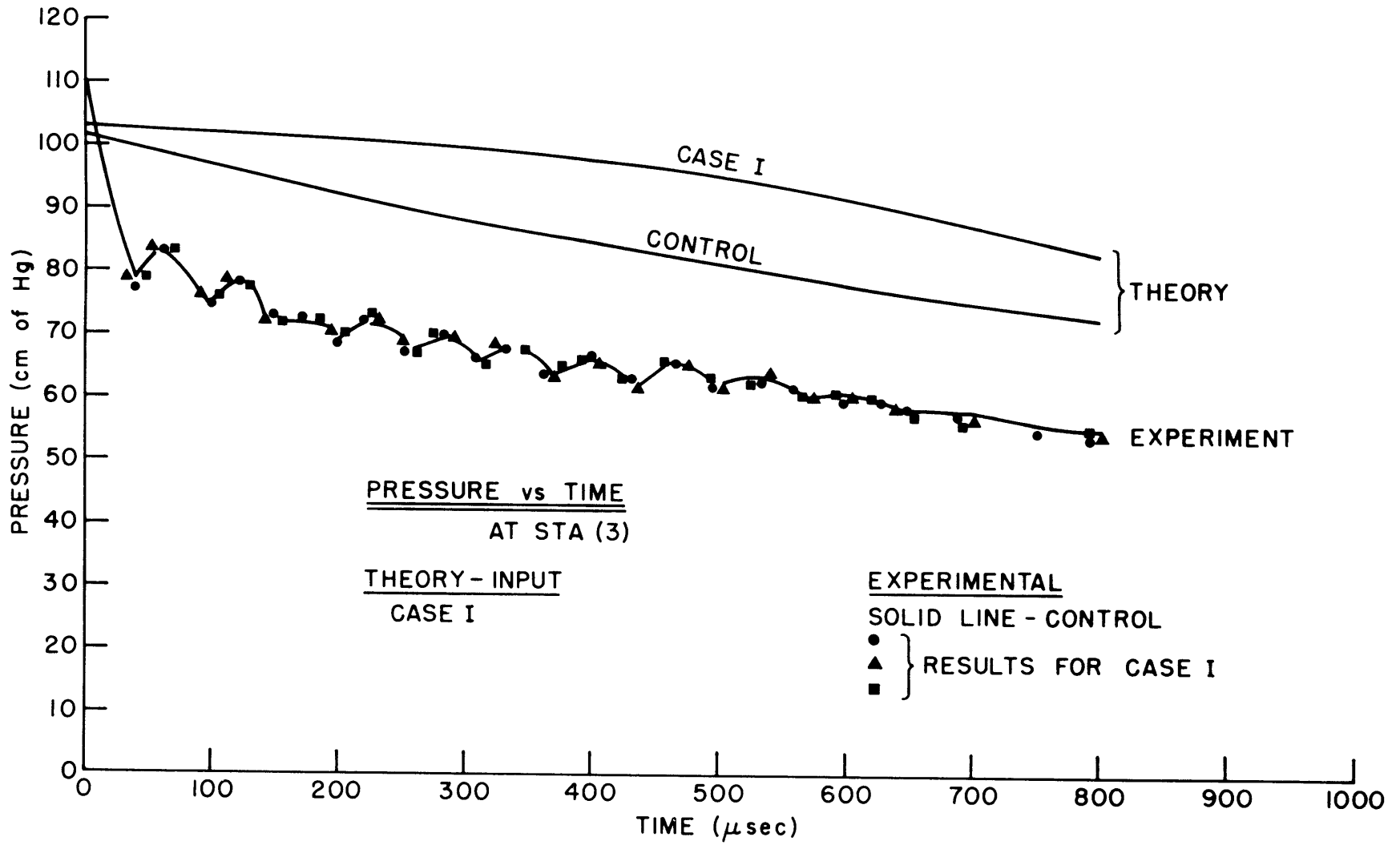


FIGURE 5-1

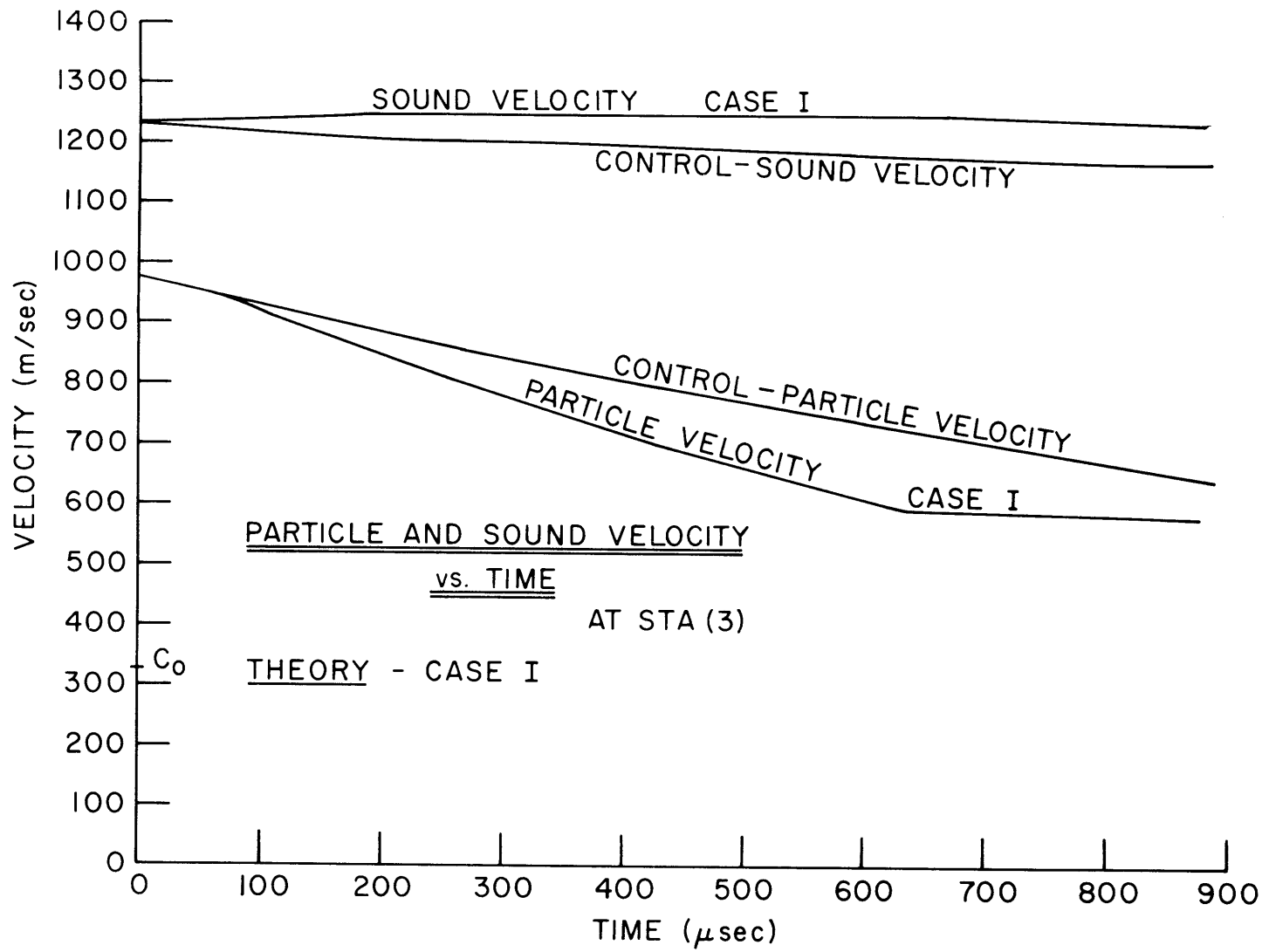


FIGURE 5-2

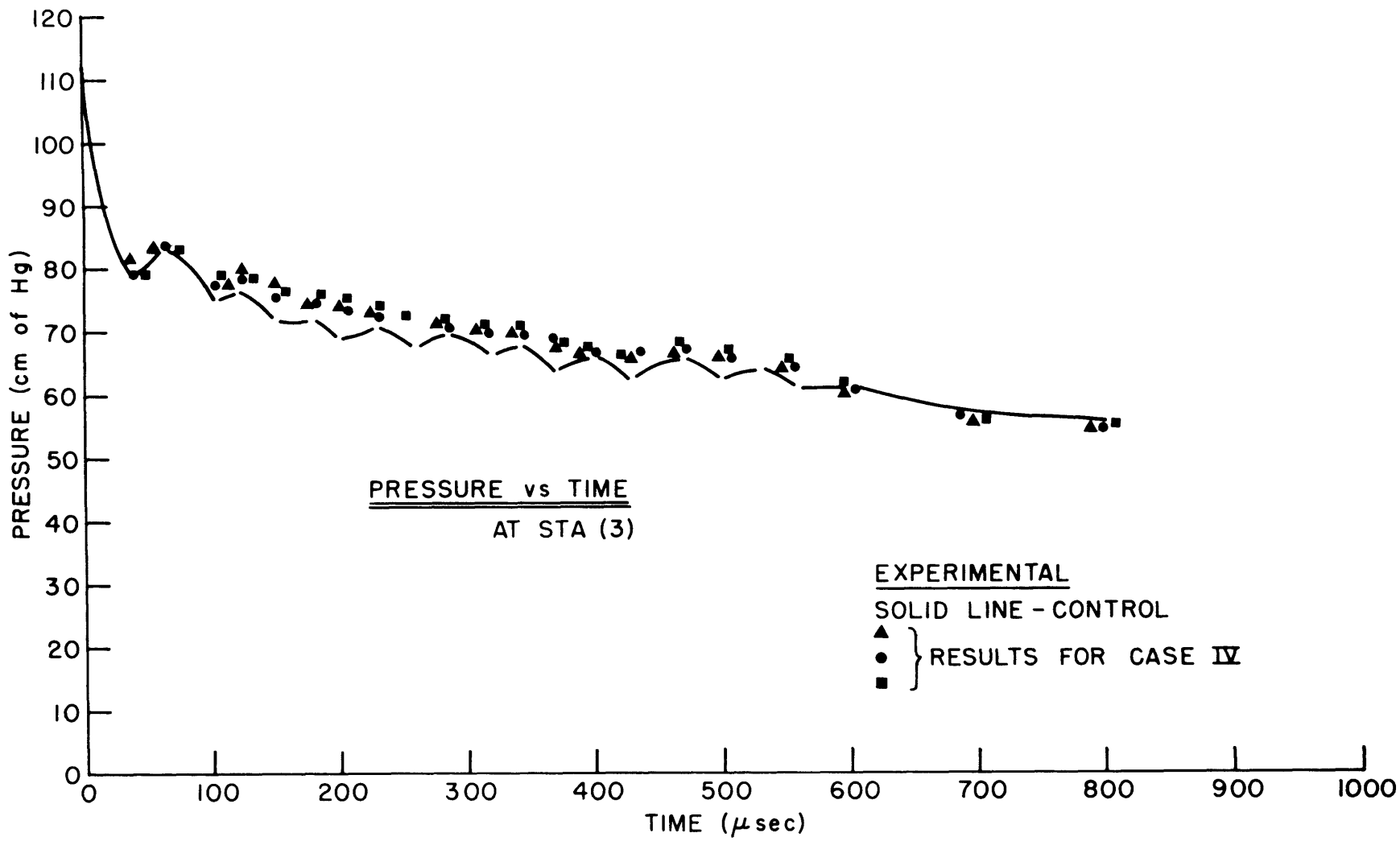


FIGURE 5-3

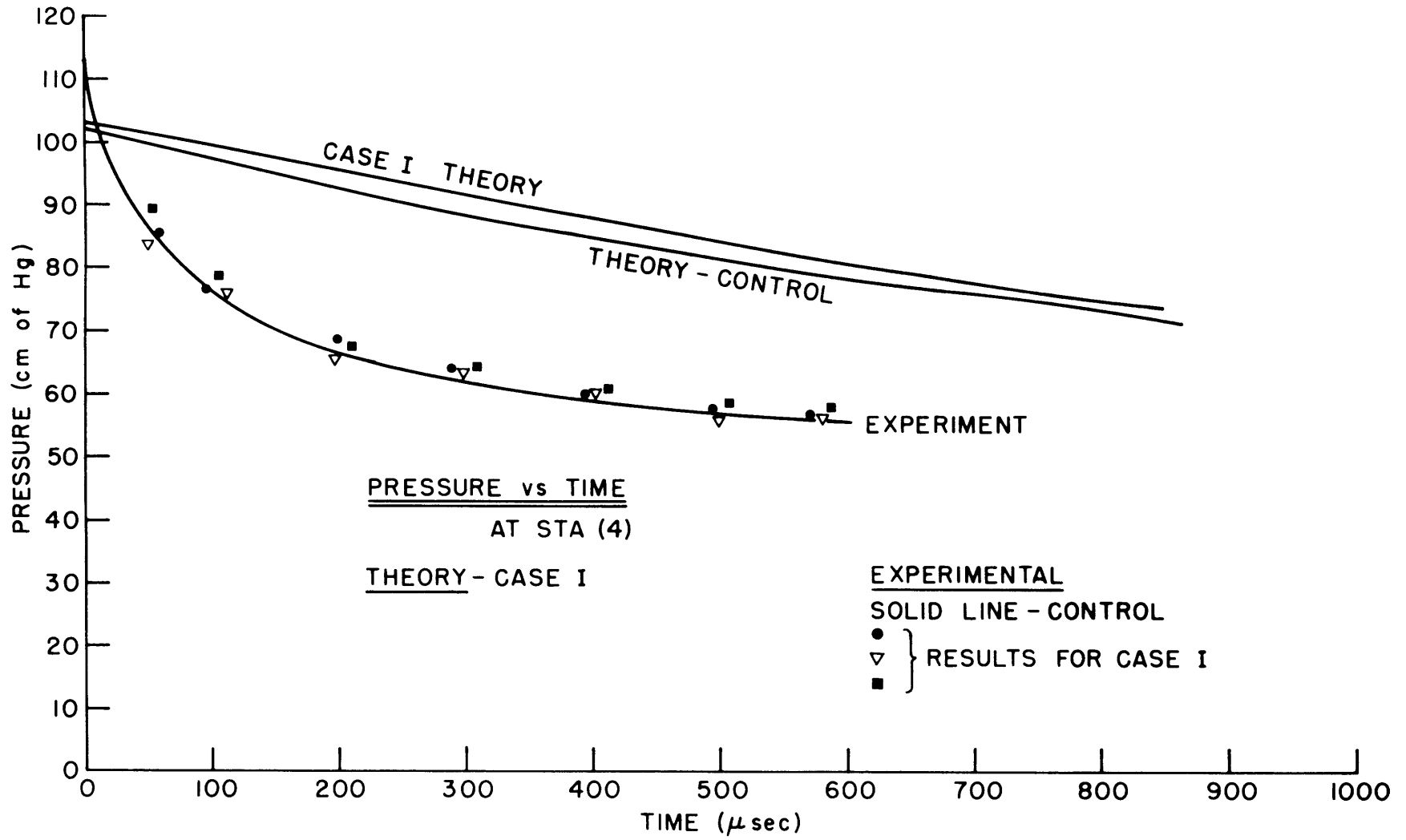


FIGURE 5-4

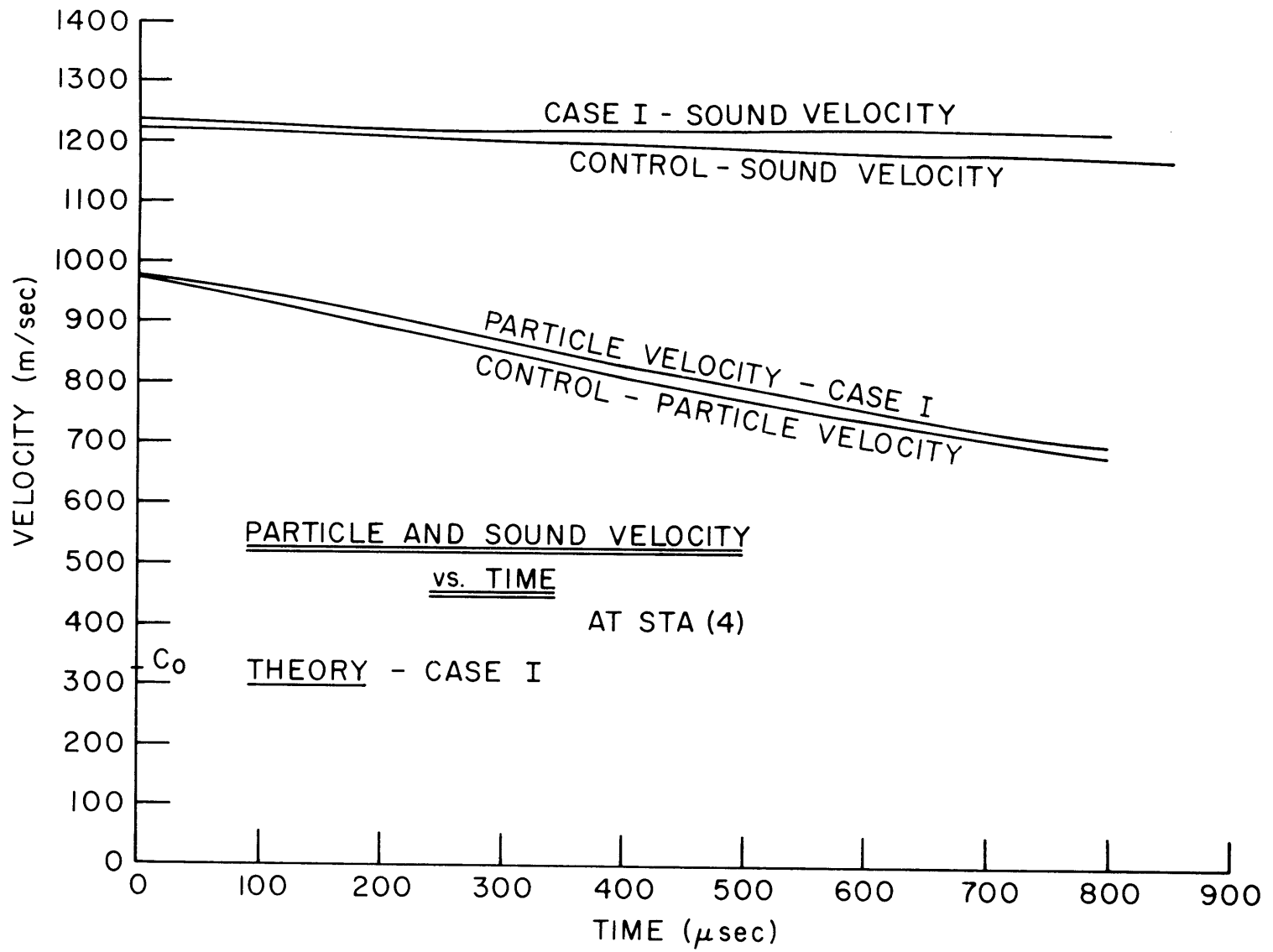


FIGURE 5-5

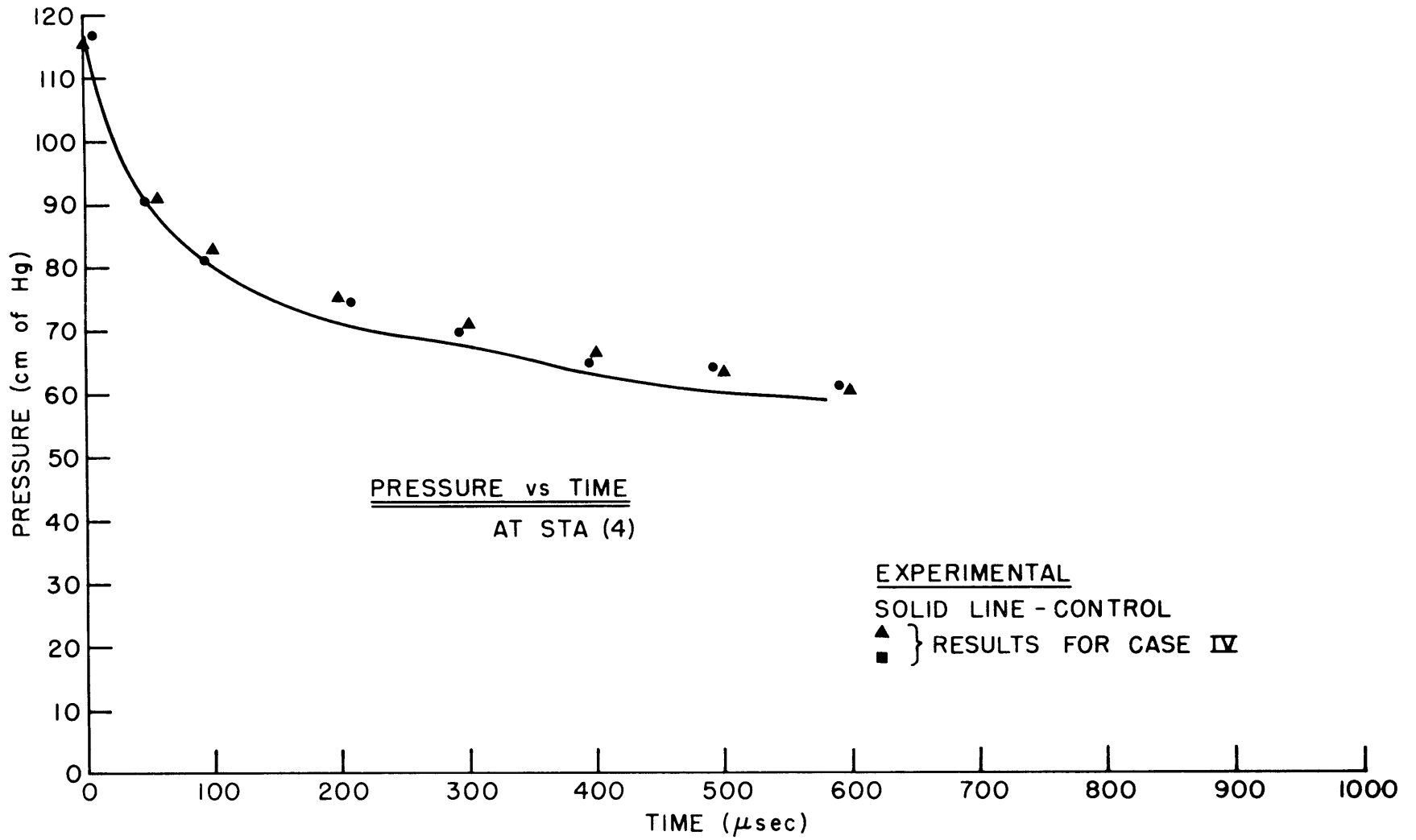


FIGURE 5-6

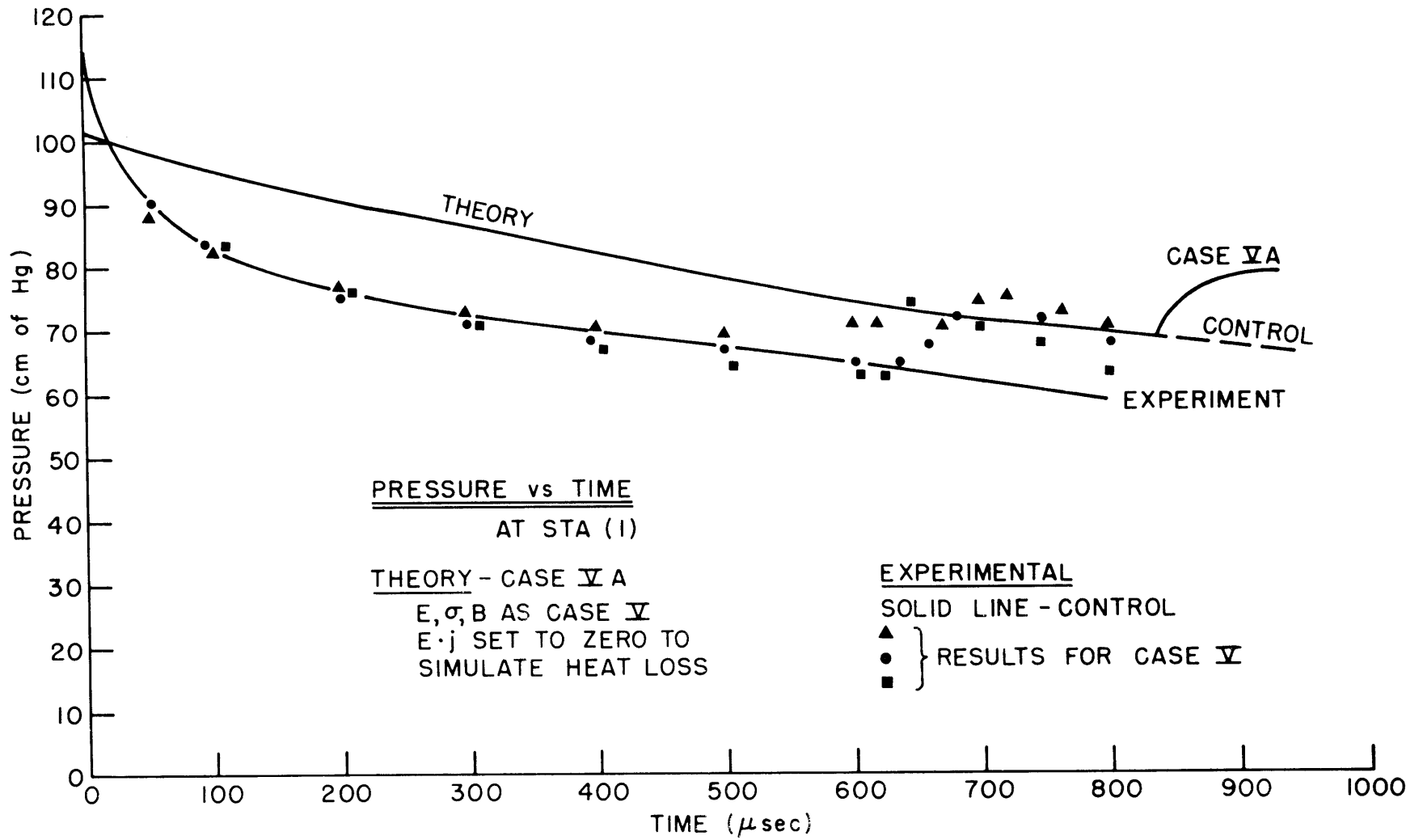


FIGURE 5-7

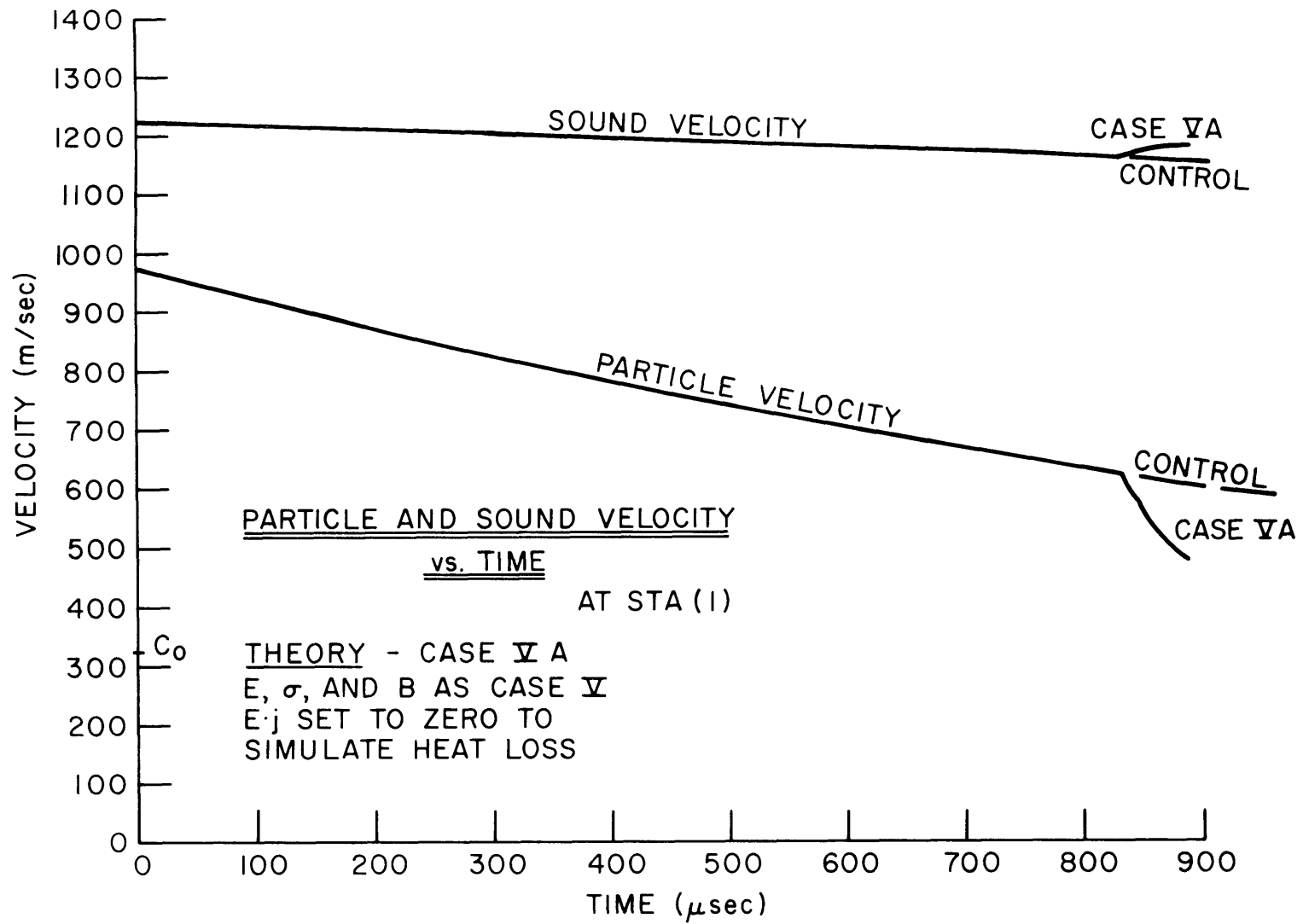


FIGURE 5-8

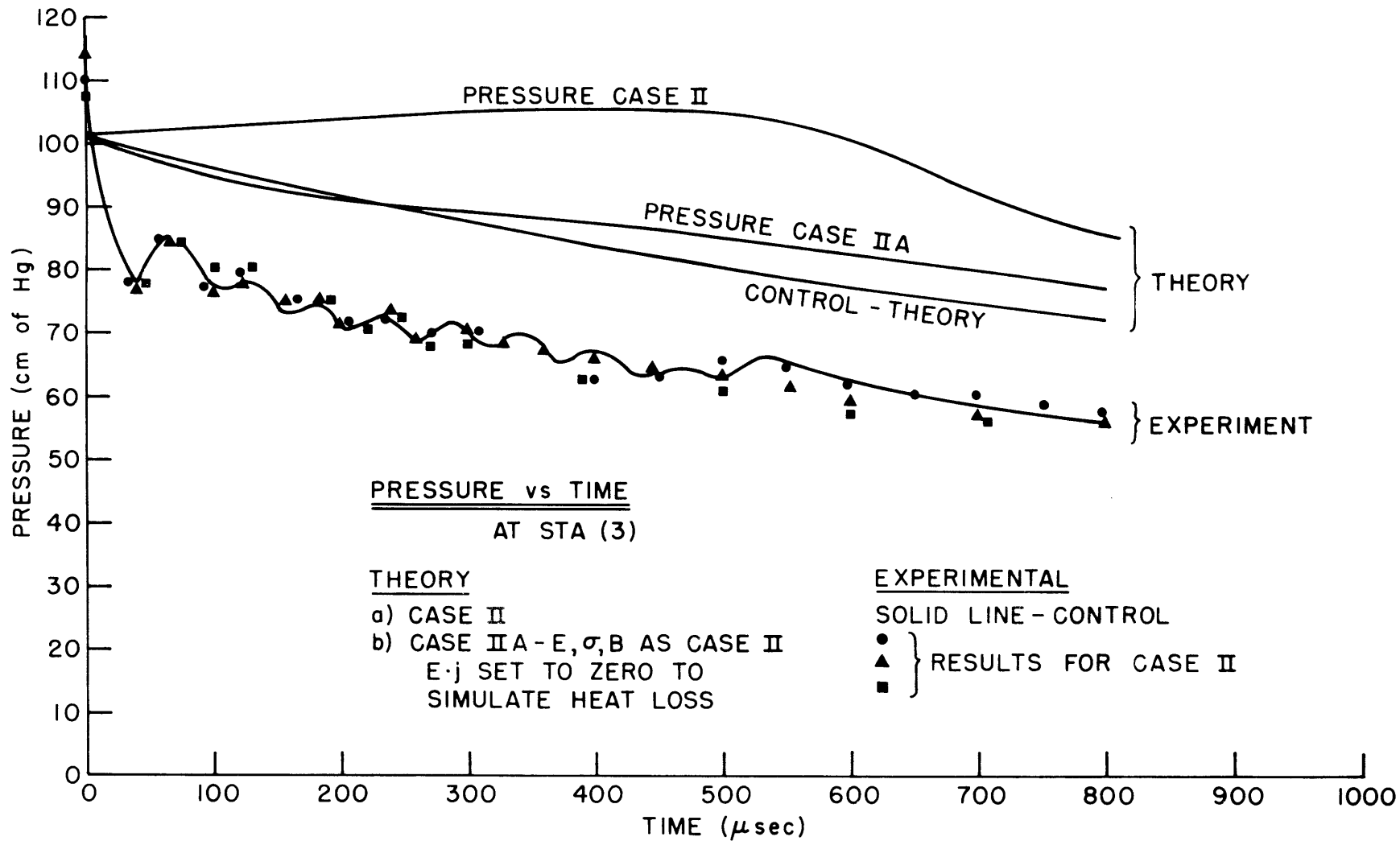


FIGURE 5-9

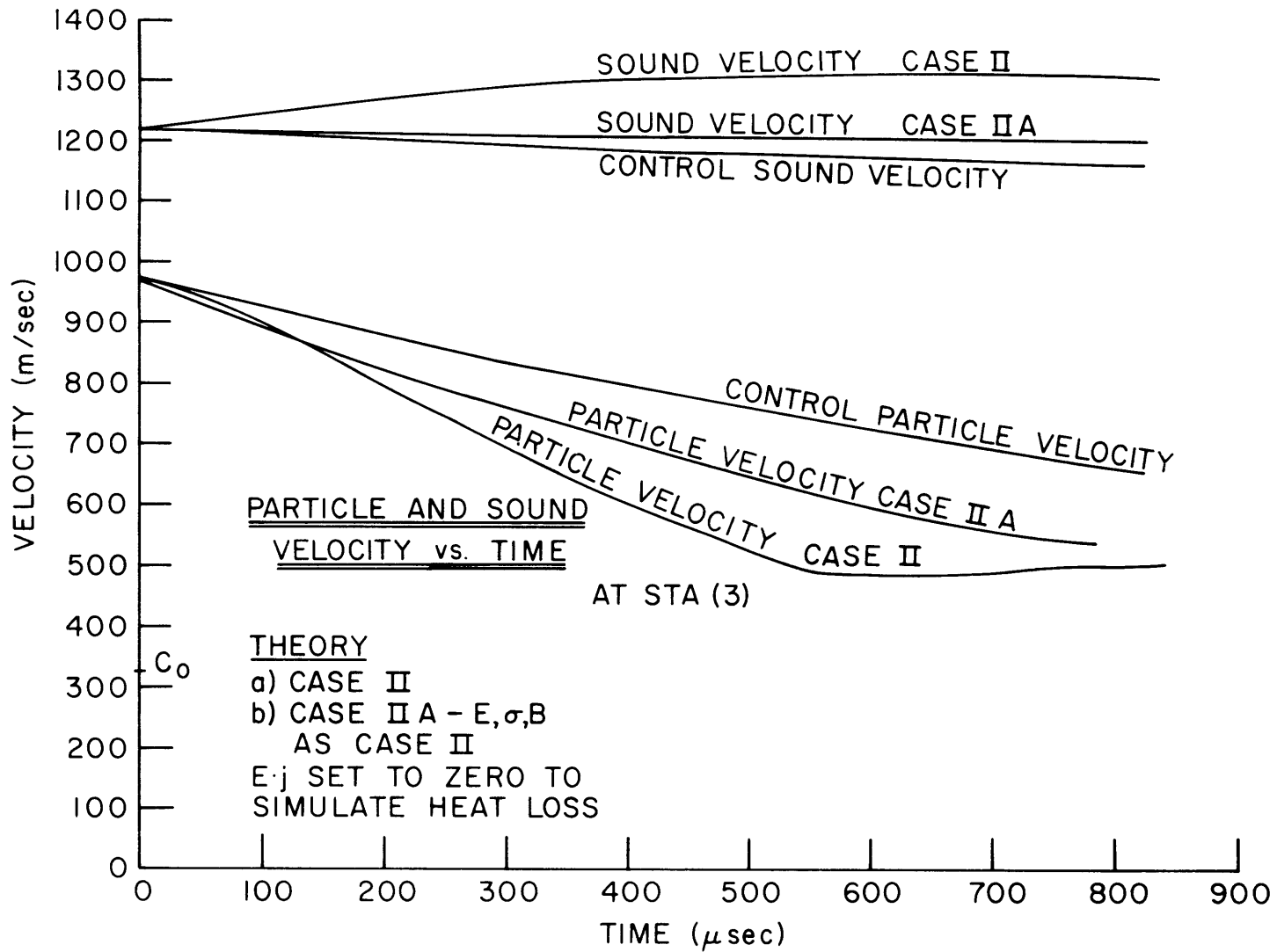


FIGURE 5-10

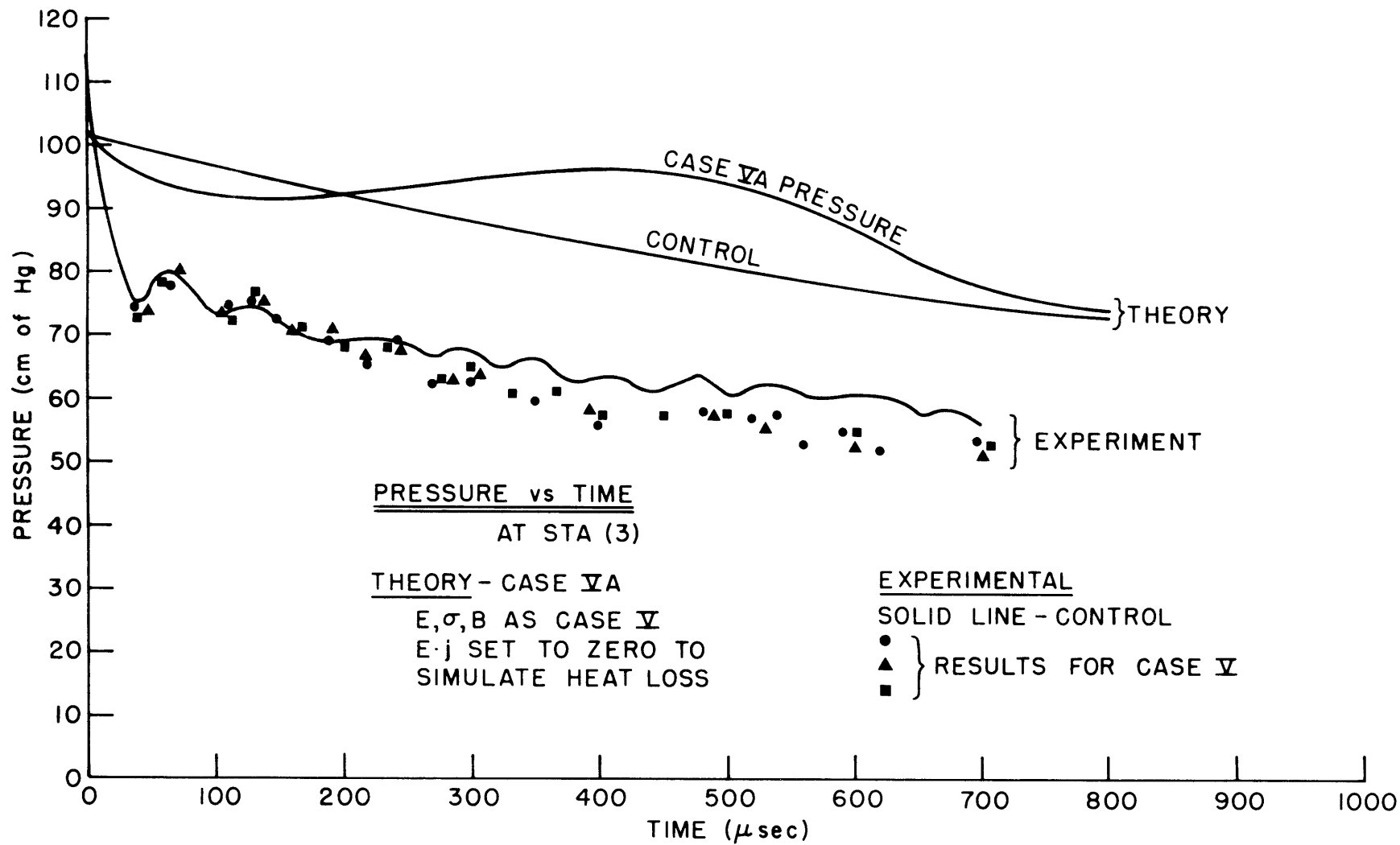


FIGURE 5-11

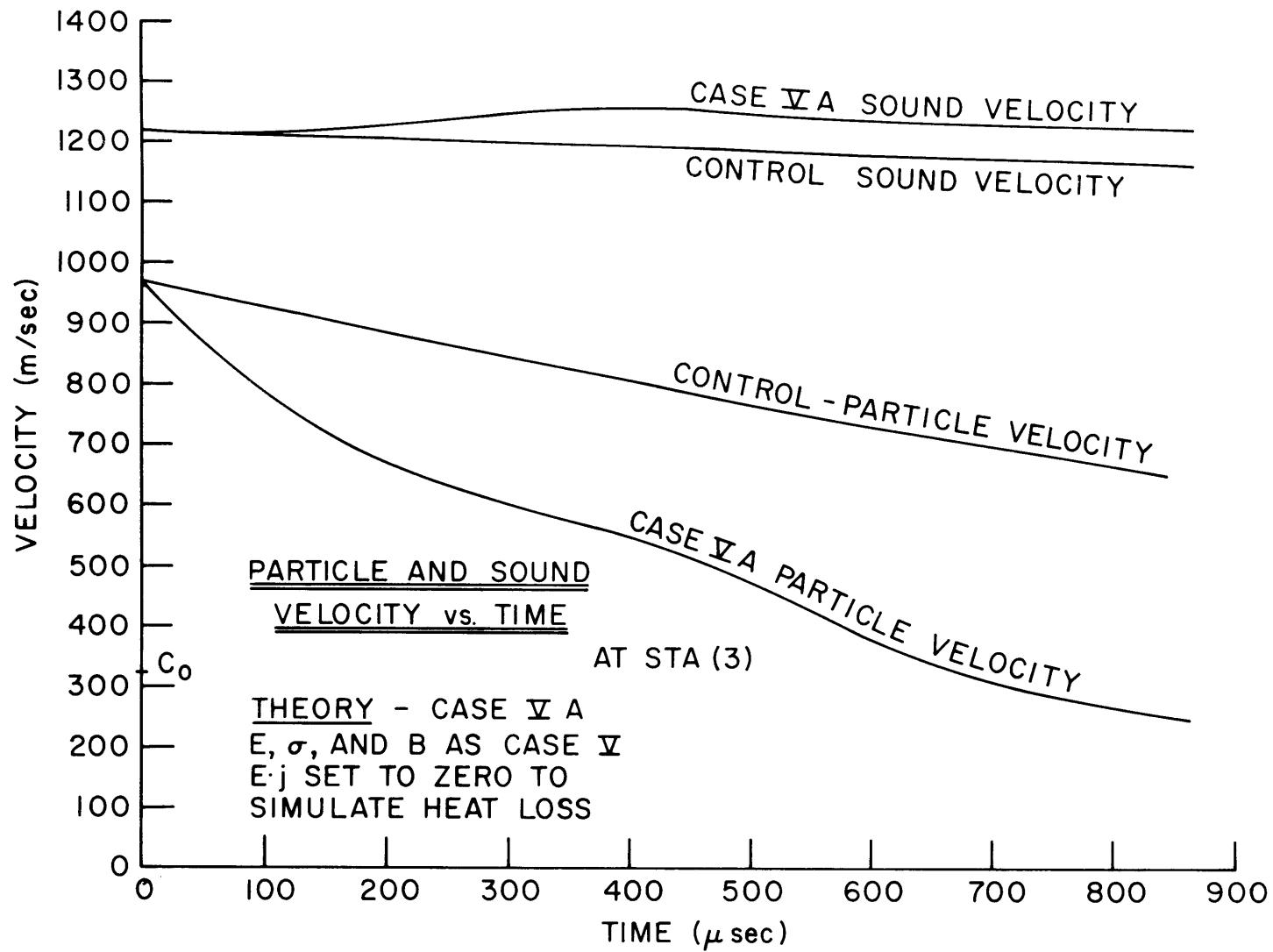


FIGURE 5-12

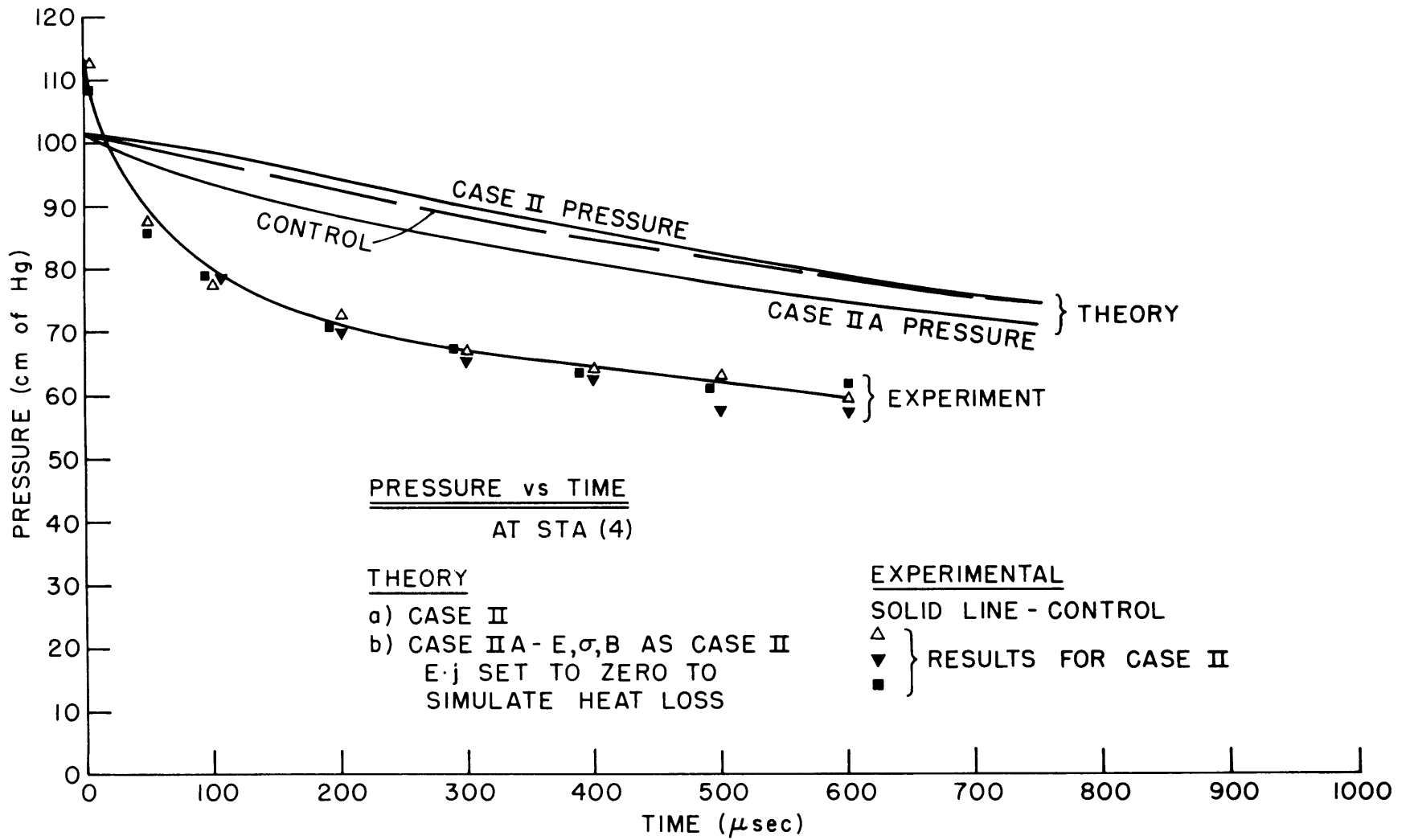


FIGURE 5-13

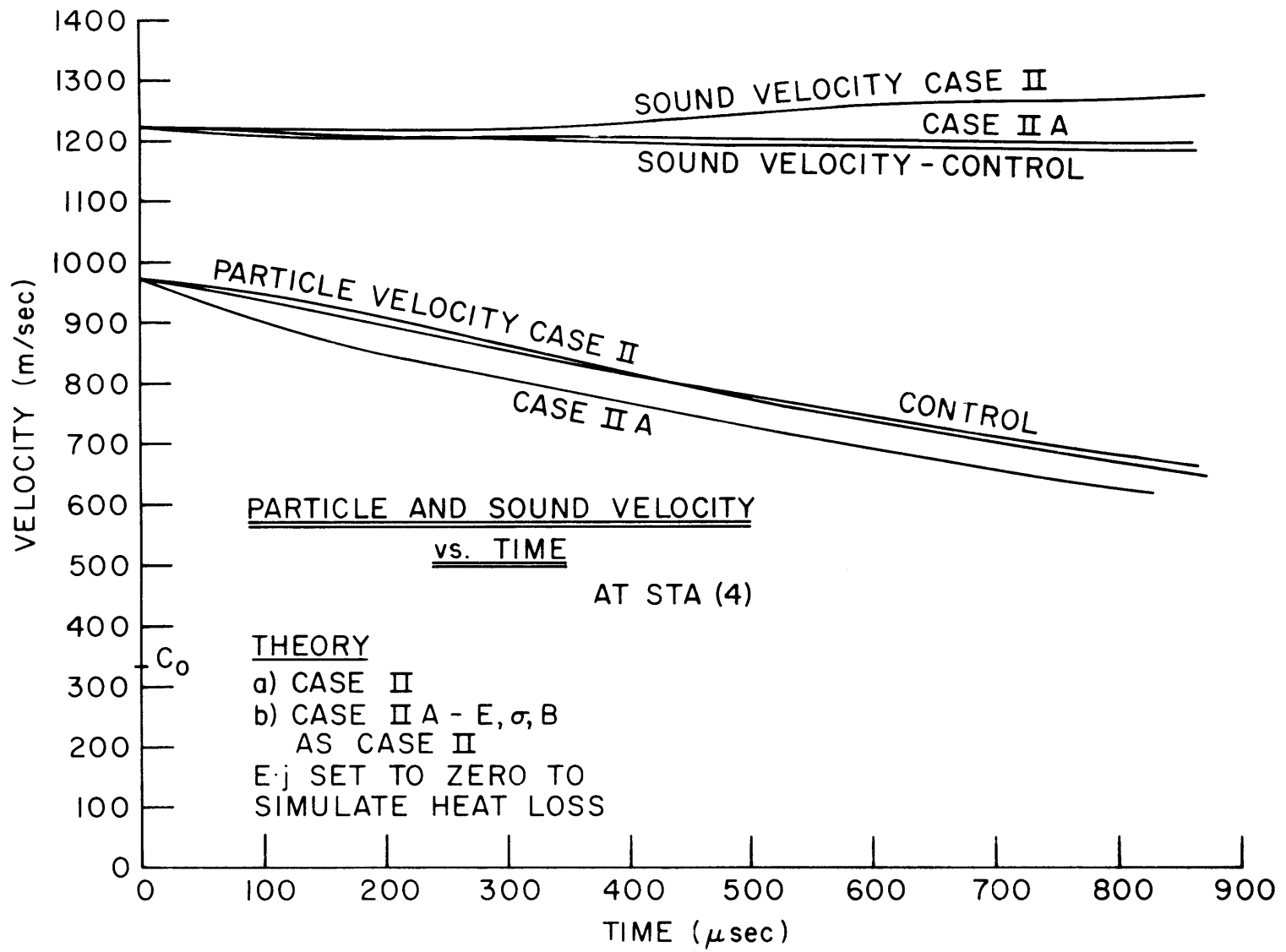


FIGURE 5-14

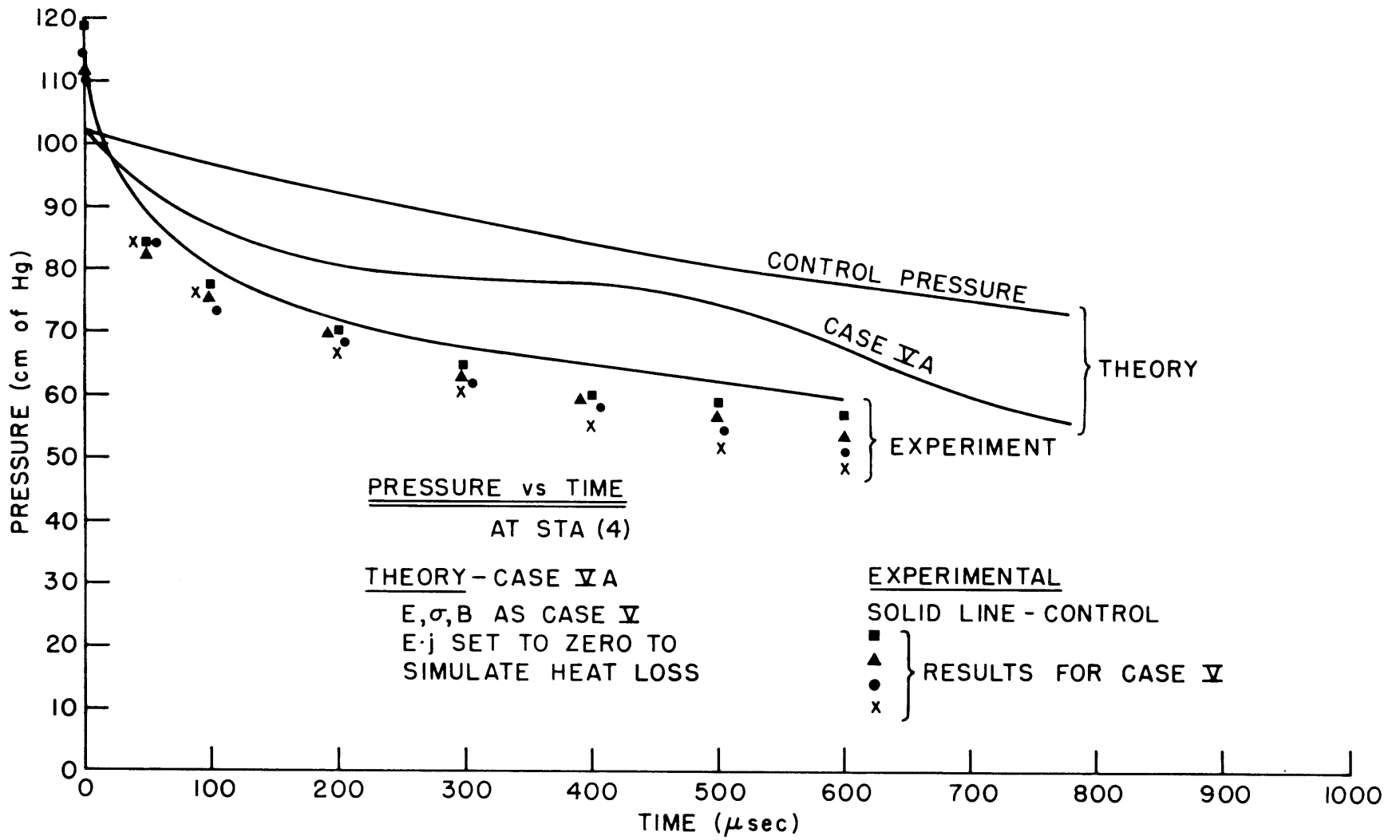


FIGURE 5-15

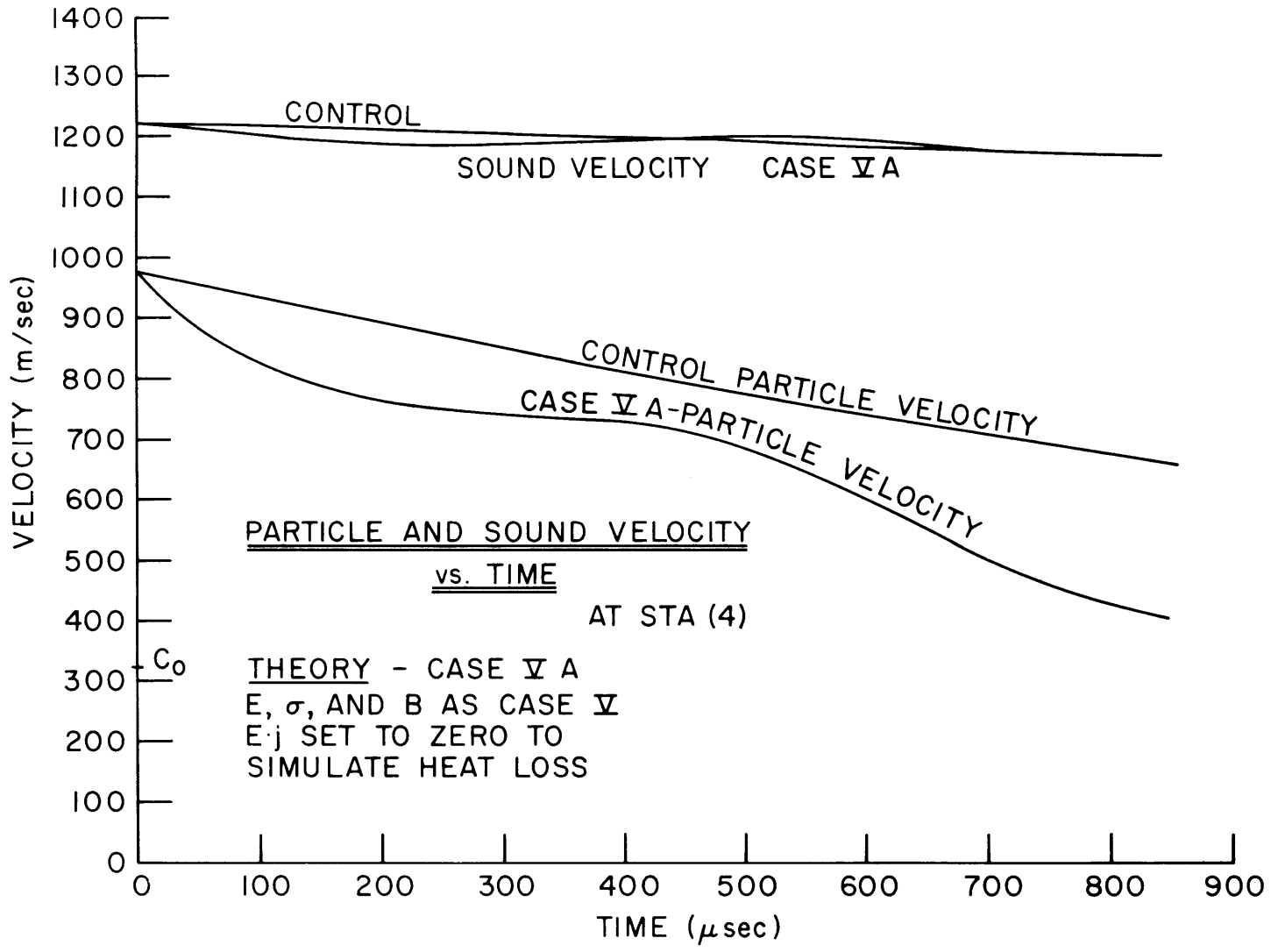


FIGURE 5-16

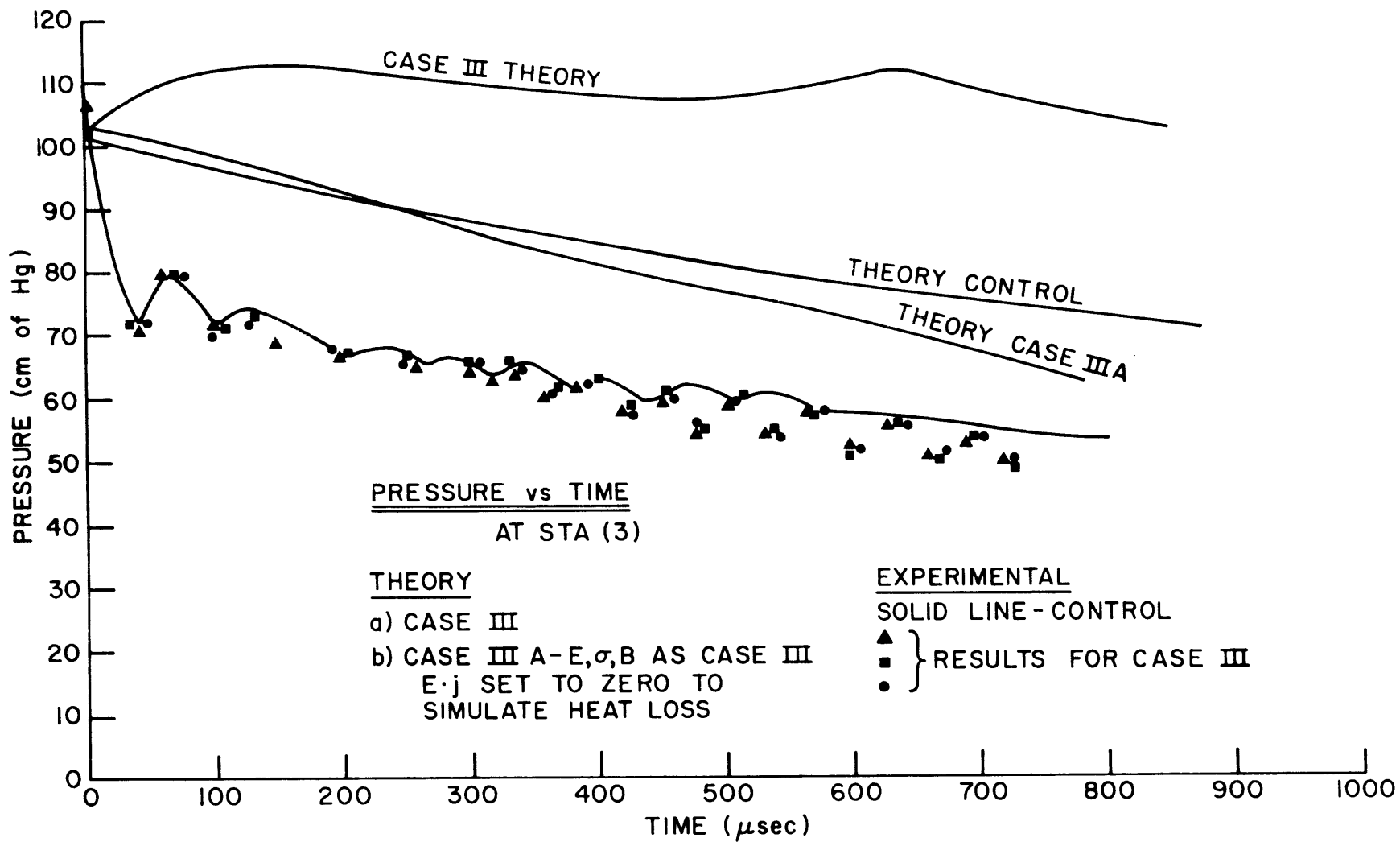


FIGURE 5-17

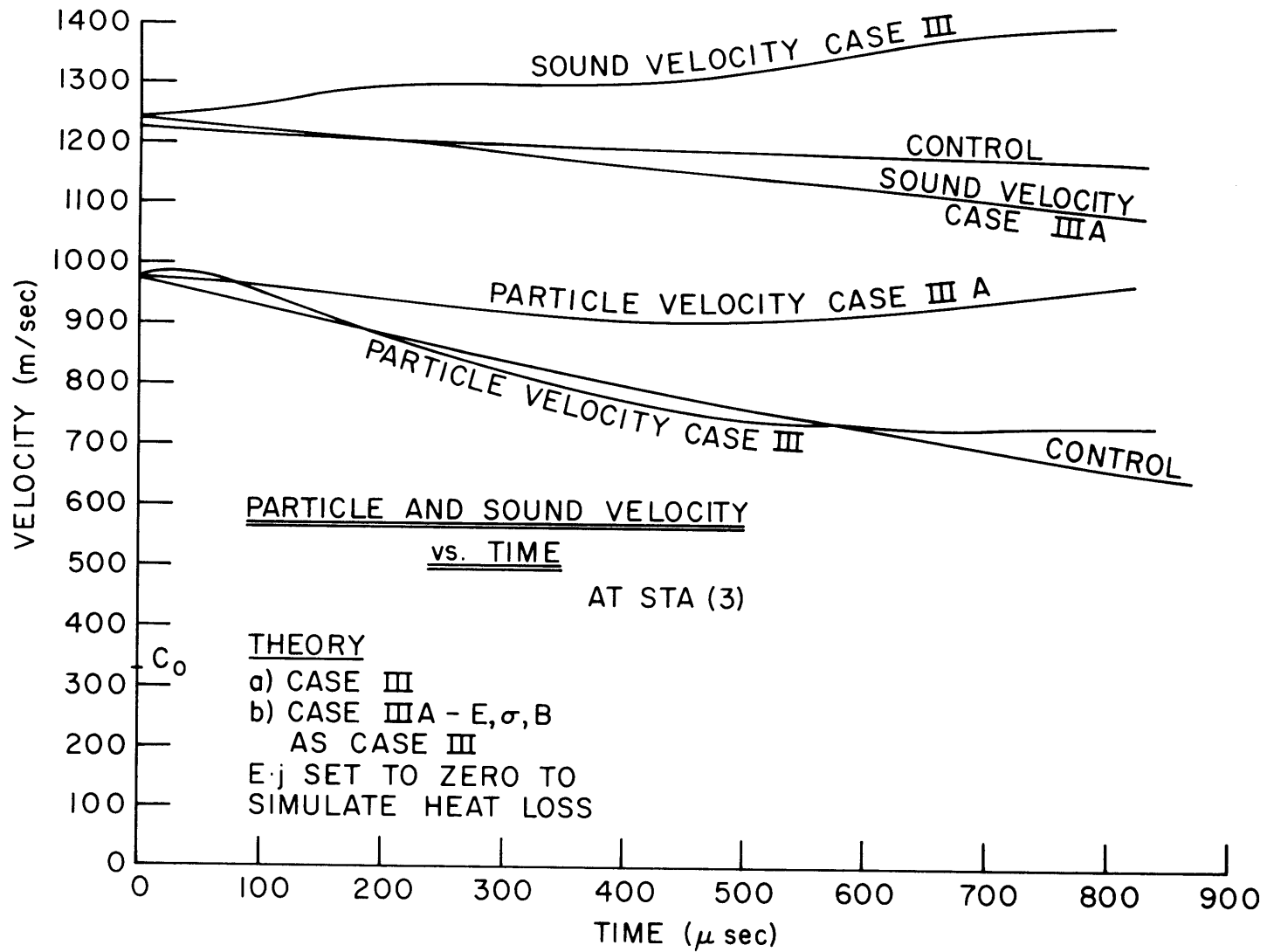


FIGURE 5-18

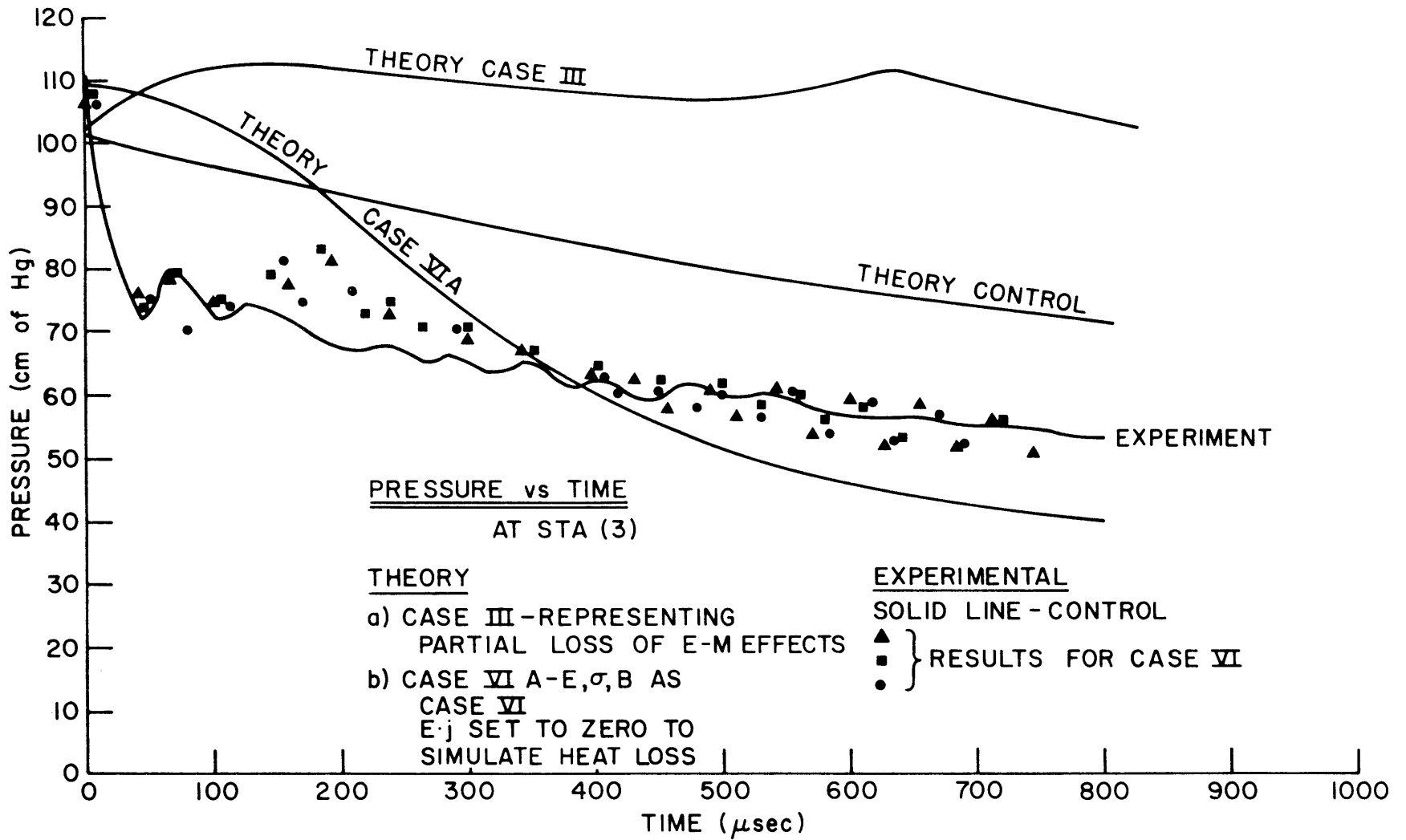


FIGURE 5-19

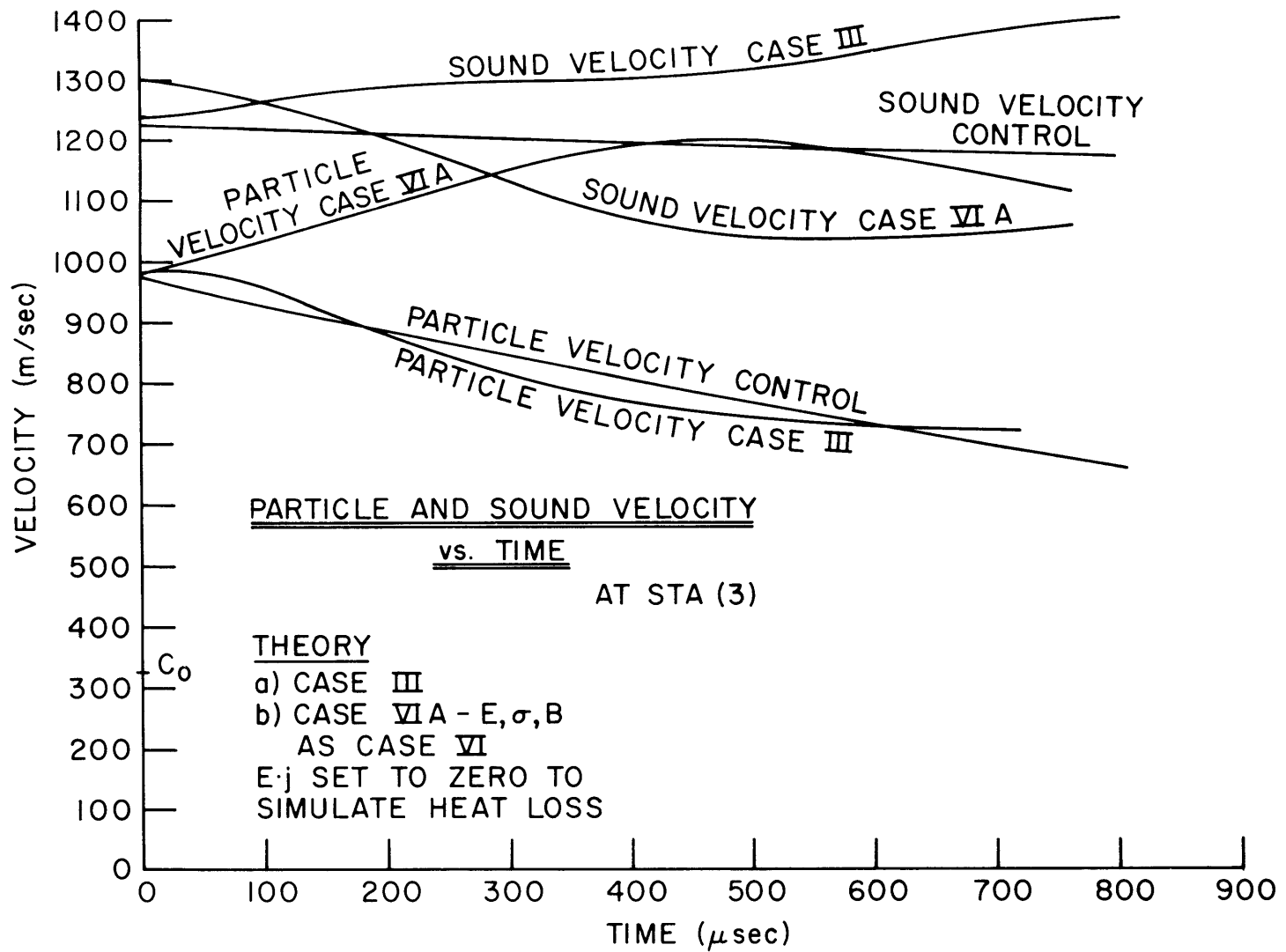


FIGURE 5-20

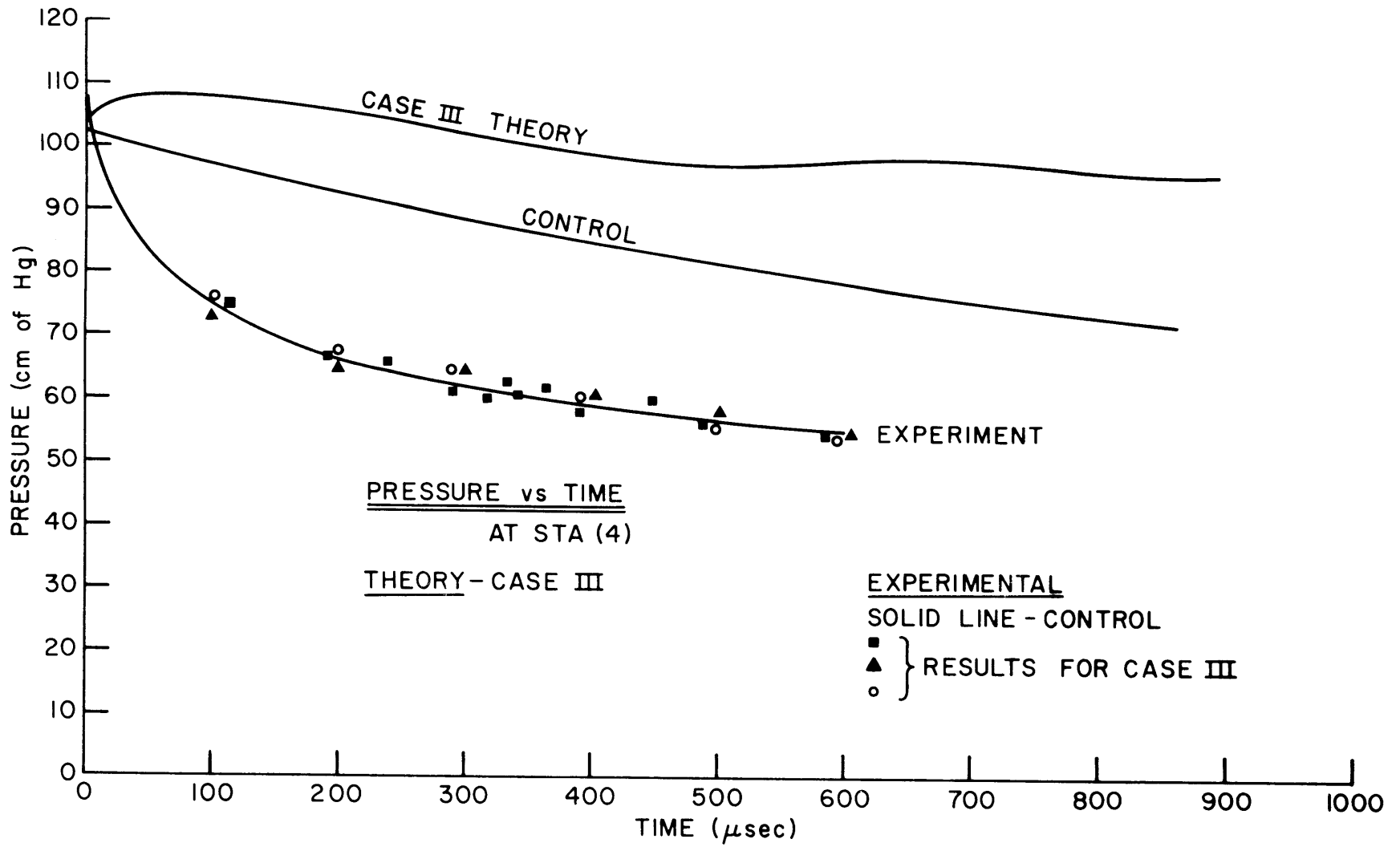


FIGURE 5-21

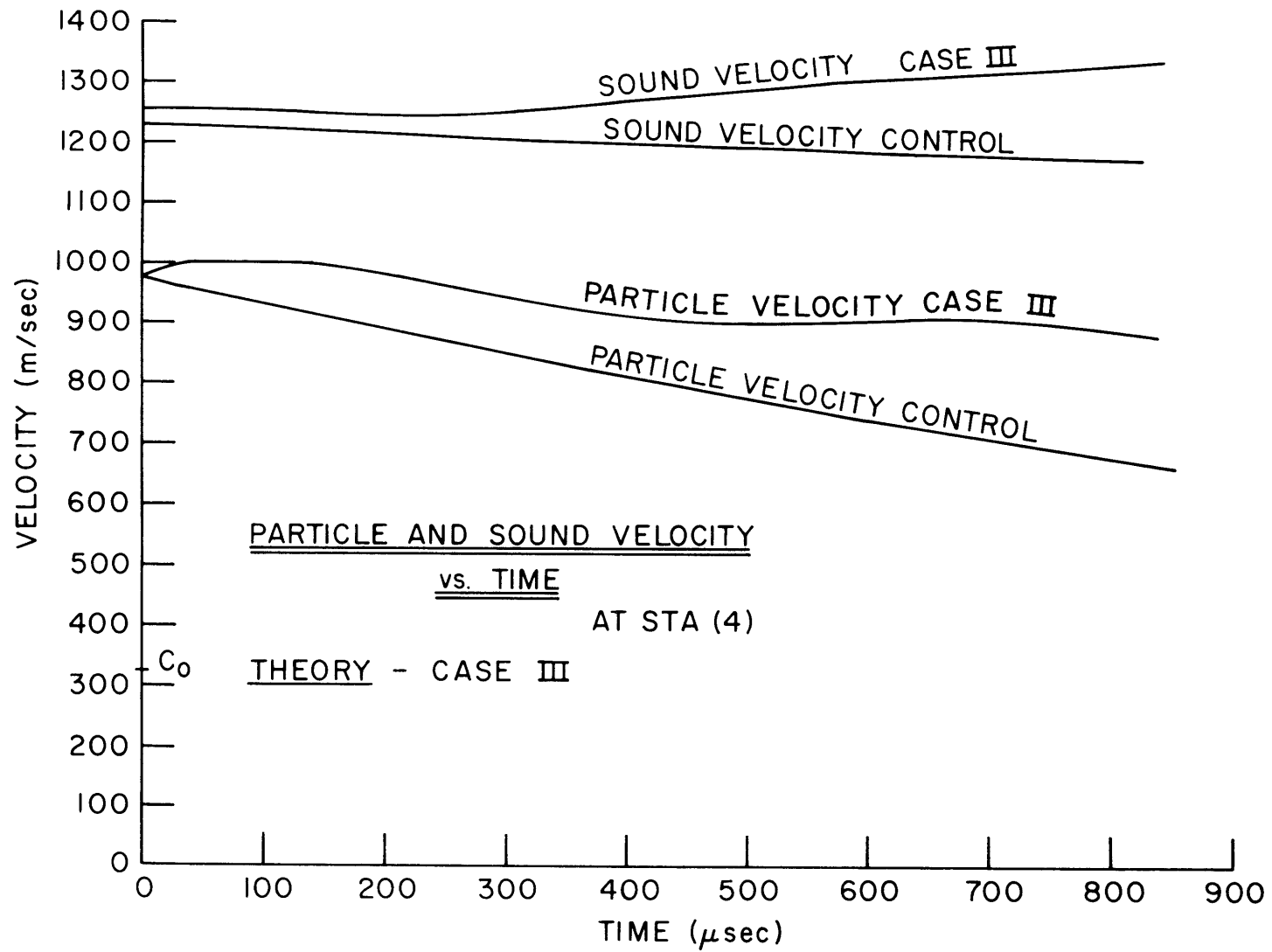


FIGURE 5-22

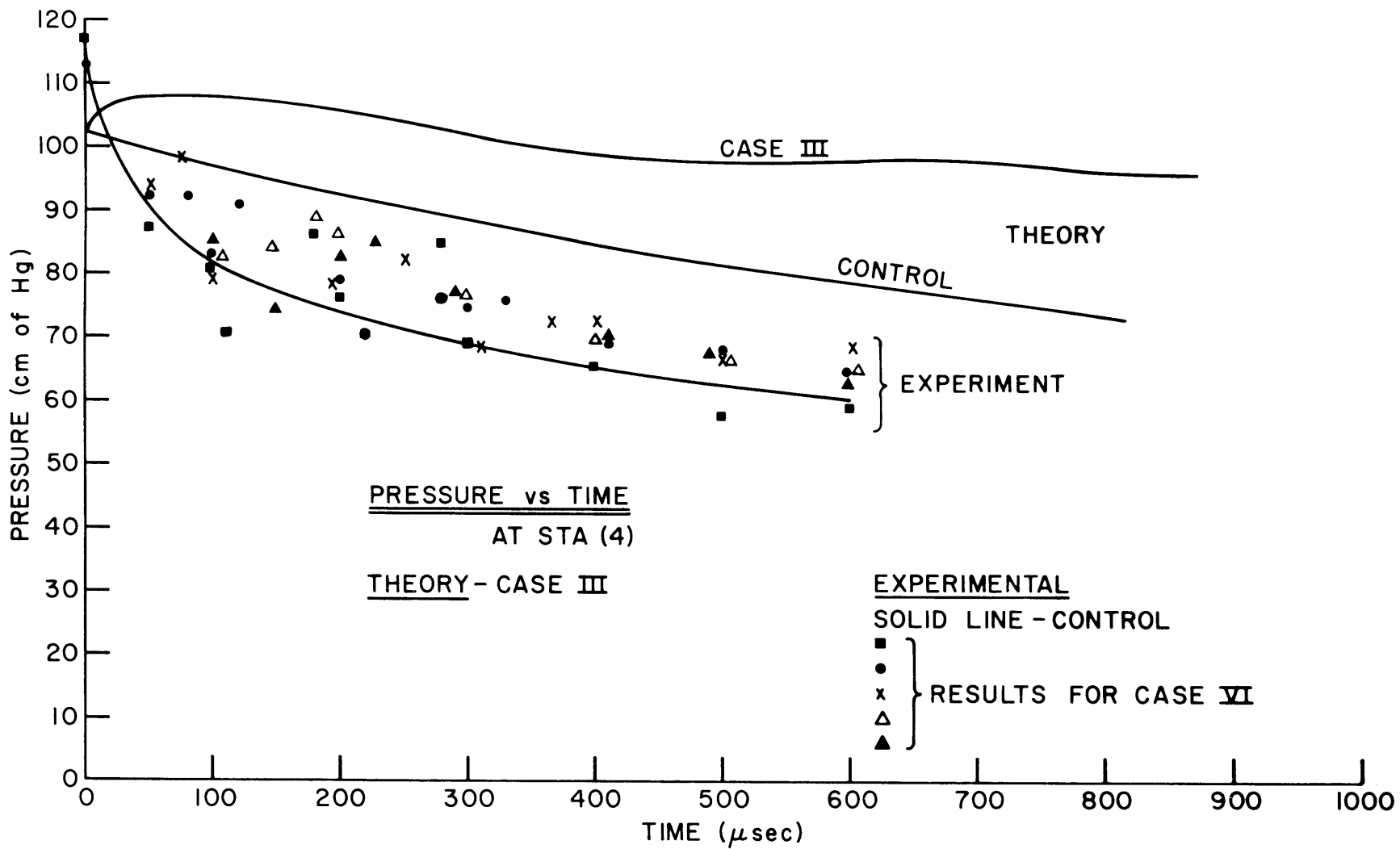


FIGURE 5-23

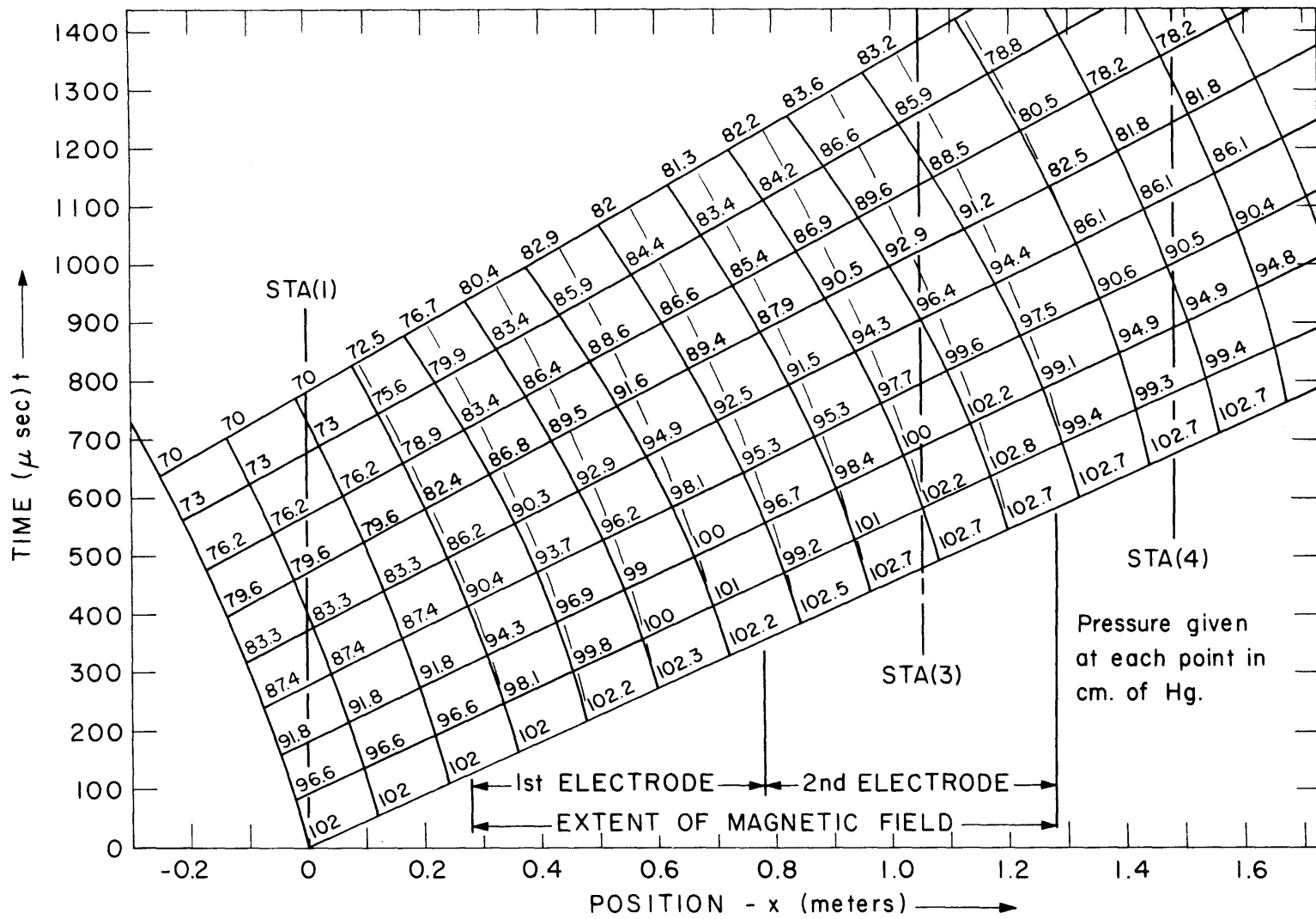


FIGURE 5-24 X-T DIAGRAM FOR CASE I (E FIELD ONLY)

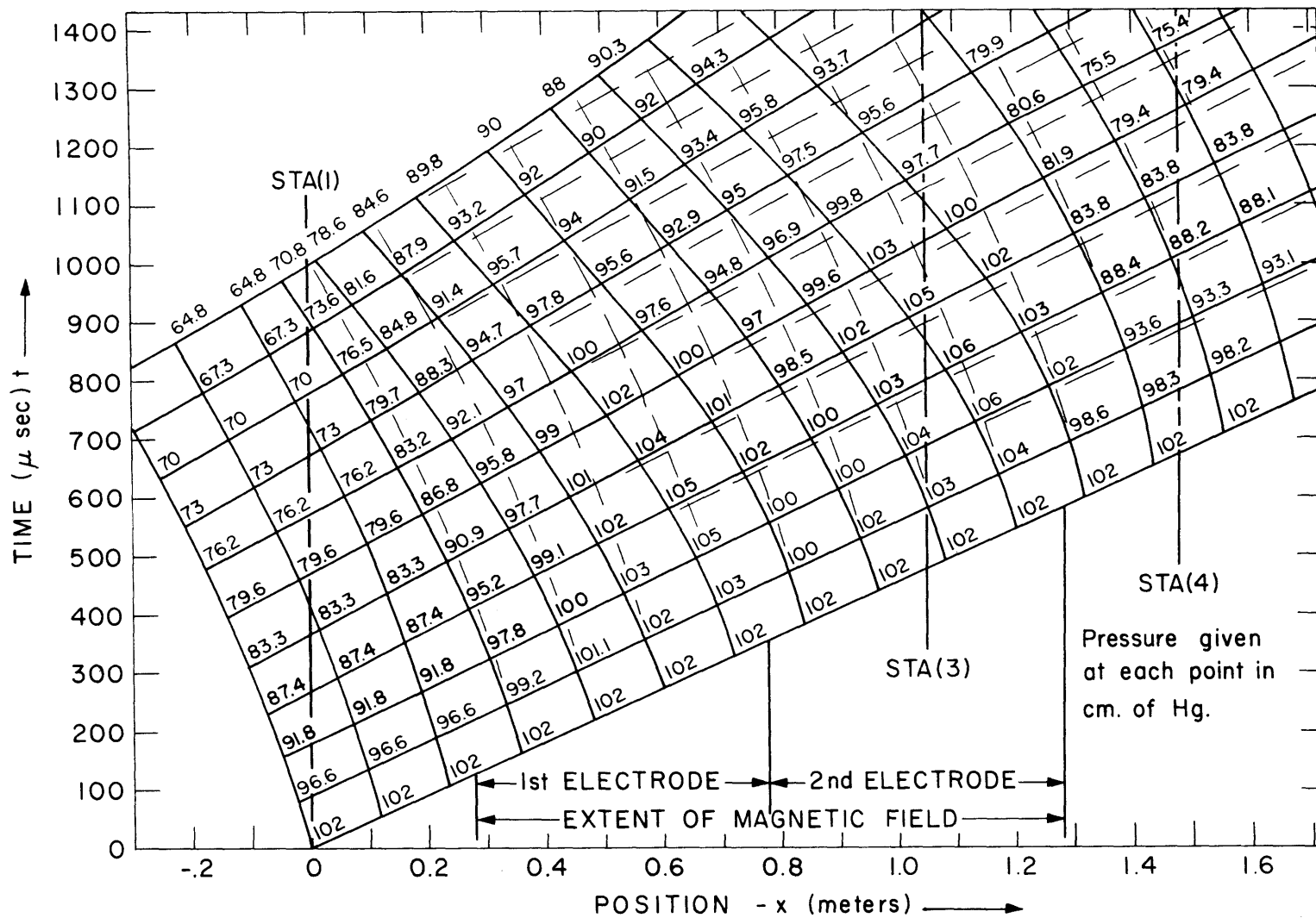


FIGURE 5-25 X-T DIAGRAM FOR CASE II ($J \times B$ RETARDING THE FLOW)

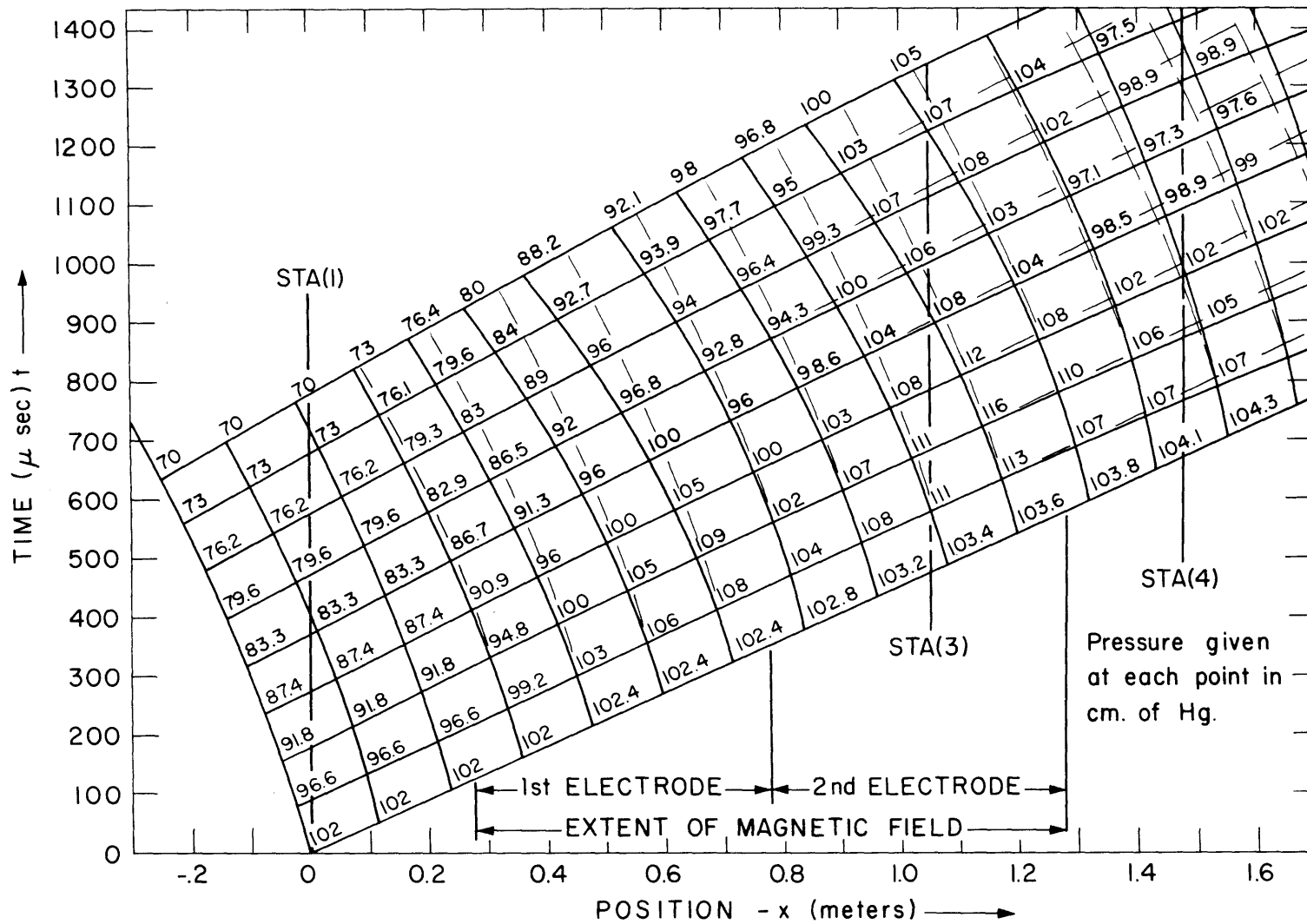


FIGURE 5-26 X-T DIAGRAM FOR CASE III ($J \times B$ PUSHING FLOW)

APPENDIX 1

SAMPLE CALCULATIONS

The values of temperature, pressure, etc. on which these calculations are based are those used in the theoretical calculations to correspond with the experiments. The experiments were done for 40 mm of Hg. initial pressure in stoichiometric $C_2H_2-O_2$ mixtures.

Magnetic Reynolds Number

- $R_m = \mu_o \sigma LU$ (for induced fields)
 $\mu_o = 4\pi \times 10^{-7}$ (magnetic permeability)
 $\sigma \sim 10$ mho/m (electrical conductivity)
 $U \sim 10^3$ m/s (velocity of product gas)
 $L \sim 1$ meter (length of field in test section)

$$R_m \cong 4\pi \times 10^{-3} \cong 10^{-2}$$

To calculate corresponding R_m in terms of applied fields

- $E \sim 2000$ v/m (applied electric field)
 $\sigma \sim 10$
 $L \sim 1$
 $B \sim 1$ web/m² (magnetic field intensity)

$$R_m \cong \frac{\Delta B}{B} \cong \frac{\mu_o j}{B} L = 8\pi \times 10^{-3} \sim 2.5 \times 10^{-2}$$

Ratio of Lorentz Force to Pressure

$$P_{CJ} \sim 100 \text{ cm Hg} \sim 1.33 \times 10^5 \text{ newt/m}^2 \text{ (pressure)}$$

$$j \approx \sigma E \sim 2 \times 10^4 \text{ amps/m}^2 \text{ (current density)}$$

$$B \sim 1 \text{ web/m}^2 \text{ (magnetic field strength)}$$

$$l \sim 1 \text{ meter (characteristic length)}$$

$$\frac{(\bar{j} \times \bar{B})/l}{P_{CJ}} \approx 0.15 \text{ per meter}$$

Ratio of Electrical Energy to Flow Energy

$$u \sim 10^3 \text{ m/sec (particle velocity)}$$

$$p \sim 1.3 \times 10^5 \text{ newt/m}^2 \text{ (pressure)}$$

$$j \sim 2 \times 10^4 \text{ amps/m}^2 \text{ (current density)}$$

$$E \sim 2 \times 10^3 \text{ volts/m}^2 \text{ (electric field)}$$

$$l \sim 1 \text{ meter (characteristic length)}$$

$$\rho = p/RT \text{ (gas density)}$$

$$\frac{(\bar{E} \cdot \bar{j})/l}{\rho u \frac{C}{P} T} = \frac{(\bar{E} \cdot \bar{j})/l}{\frac{kpu}{(k-1)}} \sim \frac{4 \times 10^7 \text{ watts/m}^3}{6.65 \times 10^8 \text{ watts/m}^2} \sim .06 \text{ per meter}$$

Electron Collision Frequency

$$\nu = \pi d^2 n \sqrt{2} \langle v_e \rangle$$

$$\langle v_e \rangle = \sqrt{\frac{8k_B T_e}{\pi m_e}} = 3.7 \times 10^5 \text{ m/sec (electron velocity)}$$

$$\text{for } T_e = 3600^\circ \text{K}$$

$$d^2 = \frac{4}{\pi} \sum X_j Q_j \sim \frac{10}{\pi} \times 10^{-15} \text{ cm}^2 \text{ (diameter of molecules)}^2$$

$$n \sim 2.4 \times 10^{18} / \text{cc (number density)}$$

$$\nu \sim 2.5 \times 10^{12} / \text{sec}$$

Hall Parameter

$$\Omega = \frac{\sigma |\bar{B}|}{n_e e}$$

n_e = n (electron number density)

$$\alpha = \frac{\sigma \sum_j X_j Q_j \sqrt{T}}{3.84 \times 10^{-10}} = \frac{\sigma (2.5 \times 10^{-15}) \sqrt{3600}}{3.84 \times 10^{-10}} = 3.9 \times 10^{-4} \sigma \text{ (mho/m)}$$

(from Saha Eqn.)

σ \approx .1 mho/cm (electrical conductivity)

e = 16×10^{-20} coul. (electron charge)

B \sim 1 web/m² (magnetic field strength)

$$\Omega \sim 0.66$$

Probe Sheath Voltage Drop

At zero current, the space charge on a probe in a plasma

$$= \frac{k_B T_e}{e} \text{ volts}$$

T_e \sim 3600°K (electron Temp.)

k_B = 1.38×10^{-16} erg/°K (Boltzmann constant)

e = 1.6×10^{-19} coulomb (electronic charge)

$$\frac{k_B T_e}{e} \sim .31 \text{ volts}$$

Thermionic Emission

$$j_s = C_E T^2 e^{-e\phi/kT}$$

for example for emission from Tungsten

$$C_E = 60.2 \text{ amp/cm}^2 \text{ deg}^2$$

$$T = 3000^\circ\text{K}$$

$$\phi = 4 \text{ volts}$$

$$j_s = 100 \text{ amp/cm}^2$$

$$= 10^6 \text{ amp/m}^2$$

This current density is higher than observed but the electrodes are not tungsten, nor would they be as hot as the gas - even at the surface.

The author has not been able to find a value of C_E for potassium, but if it is the same as tungsten, then the current emitted at several temperatures is:

$$\phi = 2.2 \text{ volts}$$

$$\epsilon^{-e\phi/kT} = \epsilon^{-25,500/T}$$

i) For $T = 1000^\circ\text{K}$

$$\begin{aligned} j_s &= (60.2) (10^6) (\epsilon^{-25.5}) (10^4) \\ &= 4.9 \text{ amps/m}^2 \end{aligned}$$

ii) For $T = 1500^\circ\text{K}$

$$\begin{aligned} j_s &= (60.2 \times 10^4) (2.25 \times 10^6) (\epsilon^{-17}) \\ &= 5.64 \times 10^4 \text{ amps/m}^2 \end{aligned}$$

$$j \sim 2 \times 10^4 \text{ amps/m}^2 \text{ from experiments}$$

Even for C_E much smaller than used here, the exponential function will quickly increase so thermionic emission could account for the current density for a temperature around 1500°K at the surface of the layer of potassium on the electrode.

APPENDIX 2
COMPUTER PROGRAM (MAD) LISTINGS

DETD A

```

R
R THIS PROGRAM HAS INTERNAL SHIFT
R AND REQUIRES GTUSR,GTPRK,MARCH,AND,LAZY TO OPERATE
R THIS DECK HAS RAREFACTION ON FIRST II CHARACTERISTIC
  INTEGER R,K,Y,Z,PLT,CYCLES,SOLNS,SOLDON,RMAX,KMAX,VHEAD,
1INT,RMIN,YN,READ,PRINT,RMAX,KS,KNXT,RS
  BOOLEAN SW1,SW3
  PROGRAM COMMON U,C,X,T,P
  D'N U(1202,PLT),C(1202,PLT),X(1202,PLT),T(1202,PLT),
1P(1202,PLT),PLT(20),VNOT(400)
  READ BCD TAPE 4,LOUPES,SOLNS
  WRITE BCD TAPE 2,LOPRNT,SOLNS
  THROUGH TY31,FOR SOLDON=1,1,SOLDON.G.SOLNS
  READ BCD TAPE READ,POINTS,RMAX,KMAX
  PLT(2)=14
  PLT(4)=RMAX
  PLT(5)=KMAX
  PLT(11)=13
  PLT(1)=28-PLT(11)
  READ BCD TAPE 4,TR10,XOW,TFF,M1,M2,V1,V2,P1,Q,B,RO,
1E1,E2,E3,E4,E5,E6,S1,S2,S3,S4
  YN=0
  INT=1
  SENDA.(0.,0.,0.,0.,0.,Q,RMAX,YN)
  SENDB.(B,Q,V1,0.,0.,0.,0.,0.,0.,0.)
  WRITE BCD TAPE 2,TR20,XOW,TFF,M1,M2,V1,V2,P1,Q,B,RO,RMAX,KMAX
1,E1,E2,E3,E4,E5,E6,S1,S2,S3,S4
  W'R RMAX .G.85,T'0 TY31
  WRITE BCD TAPE 2,WAVE
  WRITE BCD TAPE2,JOE
  COW=V2/M2
  UOW=V1-V2
  U(0,0)=UOW
  C(0,0)=COW
  X(0,0)=0.
  PNOT=133.3*P1
  CNOT =V1/M1
  VNOT(0)=V1
  POW=PNOT*(1.+Q*M1*M1)/(1.+Q*M2*M2)
  P(0,0)=POW
  ACC=M2*M2*(1.+(Q-1.)*M2*M2*.5)/((1.+Q*M2*M2)*(1.+Q*M2*M2))
  AA=(Q-1.)*.5-Q*Q*ACC
  BE=1.-2*Q*ACC
  CUE=(ACC-AA*(M1).P.4)/(M1*M1)-BE
  PRINT RESULTS CUE
  T(0,0)=X(0,0)/V1

```

```

LX2=XOW
T(1,0)=T(0,0)+TFF
R=1
Y=R-1
RMIN=1
YN=0
K=0
SEDC.(0,XOW,0.,0,0,0,0,0)
PRESS=POW/1333.
WRITE BCD TAPE 2,FORT,0,0,UOW,COW,X(0,0),T(0,0),PRESS
K010 T(R,0)=T(0,0)+R*TFF
      U(R,0)=UOW*(2.22*RO/(RO+(UOW+COW)*T(R,0))-1.22)
      C(R,0)=COW-(Q-1.)*(UOW-U(R,0))*0.5
      P(R,0)=POW*(1.-(Q-1.)*(UOW-U(R,0))/(2.*COW)).P.(2.*Q/(Q-1.))
      UR=(U(R,0)+U(Y,0))*0.5
      CR=(C(R,0)+C(Y,0))*0.5
      X(R,0)=X(Y,0)+(T(R,0)-T(Y,0))*(UR-CR)
      PRESS=P(R,0)/1333.
      WRITE BCD TAPE 2 ,FORT,R,K,U(R,K),C(R,K),X(R,K),T(R,K),PRESS
      WHENEVER R.E.RMAX
      K=K+1
      R=RMIN
      TRANSFER TO TY21
      END OF CONDITIONAL
      R=R+1
      Y=R-1
      TRANSFER TO K010
TY21 Z=K-1
      Y=R-1
      K=1
WA12 CONTINUE
      Z=K-1
      C(YN,K)=C(YN,Z)
      U(YN,K)=U(YN,Z)
      P(YN,K)=P(YN,Z)
      U2=U(YN,Z)
      VNOT(K)=VNOT(Z)
      DUR1=0
WA10 X(YN,K)=X(YN,Z)+LX2
      W'R INT.E.5
      T(YN,K)=T(YN-1,Z)+LX2/((VNOT(K)+VNOT(Z))*0.5)
      O'E
      T(YN,K)=T(YN,Z)+LX2/((VNOT(K)+VNOT(Z))*0.5)
      E'L
      UR=(U(YN,K)+U(YN,Z))*0.5
      CR=(C(YN,K)+C(YN,Z))*0.5
      PR=(P(YN,K)+P(YN,Z))*0.5
      XR=(X(YN,K)+X(YN,Z))*0.5
      W'R M2.GE..99
      UO=U(YN,Z)

```

```

TO=T(YN,Z)
CO=C(YN,Z)
O'R INT.E.5
TO=T(YN,Z)
UO=U(YN,Z)
CO=C(YN,Z)
O'E
UZ=(U(YN,Z)+U(YN+1,Z))*0.5
CZ=(C(YN,Z)+C(YN+1,Z))*0.5
UCZ=UZ-CZ
UCR=UR+CR
TO=(X(YN,K)-X(YN,Z)-T(YN,K)*UCR+T(YN,Z)*UCZ)/(UCZ-UCR)
LL=TO-T(YN,Z)
L=T(YN+1,Z)-T(YN,Z)
UO=U(YN,Z)+(U(YN+1,Z)-U(YN,Z))*LL/L
CO=C(YN,Z)+(C(YN+1,Z)-C(YN,Z))*LL/L
E'L
W'R XR.GE.1.28
SR=0
O'R XR .LE..28
SR=0
O'E
SR=S1
E'L
W'R XR.GE..28 .AND. XR.LE..78
XER=XR-.28
O'E
XER=XR-.78
E'L
ER=E1+E2*XER
UEJR=CR*ER*SR*(ER-UR*B)/PR
UJBR=CR*(1.-Q*UR/CR)*B*CR*SR*(ER-UR*B)/(Q*PR)
R=YN
PRSUR.(USR,USK,X,T,C,P,R,K)
DUR=(USR+UEJR+UJBR+UAR)*(T(YN,K)-TO)
DTT=5+.1*(.ABS.(DUR))
CTT=1
C2=CO+(Q-1.)*.5*(DUR-(U2-UO))
M2=(VNOT-U2)/C2
W'R M2.G.1.0
M2=1.0
C2=COW
E'L
ACC=M2*M2*(1.+(Q-1.)*M2*M2*.5)/((1.+Q*M2*M2)*(1.+Q*M2*M2))
EX=Q*Q*ACC-.5*(Q-1.)
WY=1.+CUE-2*Q*ACC
M1SQ=(WY+SQRT.(WY*WY-4.*EX*ACC))/(2.*EX)
M1A=SQRT.(M1SQ)
V1A=M1A*CNOT
U2A=V1A-C2*M2

```

WA15

```

WHENEVER .ABS. ((V1A-VNOT)/V1) + .ABS. ((U2A-U2)/U2) .LE. .001 .AND.
1CTT.G.DTT,T'O WA20
VNOT=V1A
U2=U2A
CTT=CTT+1
TRANSFER TO WA15
WA20 VNOT(K)=V1A
U(YN,K)=U2
C(YN,K)=C2
P(YN,K)=PNOT*(1.+Q*M1*M1)/(1.+Q*M2*M2)
T(YN,K)=T(YN,Z)+LX2/((VNOT(K)+VNOT(Z))*5)
DUW=1+.ABS.(DUR)
W'R .ABS.((DUR1-DUR)/DUW).LE..01,T'O WA40
DUR1=DUR
TRANSFER TO WA 10
WA40 CONTINUE
M1=M1A
PRESS=P(YN,K)/1333.
WRITE BCD TAPE 2,FORT,0,K,U(YN,K),C(YN,K),X(YN,K),T(YN,K),
1PRESS,VNOT(K),USR,UEJR,UJBR,M1,M2,DUR,ER,SR
W'R INT.E.2
YN=YN+1
RMIN=RMIN+1
SENDA.(0.,0.,0.,0.,0.,Q,RMAX,YN)
INT=5
T'O WA12
O'R INT.E.5
INT=3
LX2=XOW
E'L
LAZY.(U,C,X,T,P,R,K)
R=YN+1
RMIN=R
MARCH.(PLT,B,Q,R,K,RMIN,RMAX,SW3)
TY22 WHENEVER K.E.KMAX, TRANSFER TO TY 23
WHENEVER SW3,T'O TY30
UCW=VNOT(K)
UCRM=U(RMIN,K)+C(RMIN,K)
WHENEVER UCW .GE. UCRM, TRANSFER TO TY23
T(YN,K+1)=T(YN,K)+LX2/VNOT(K)
X(YN,K+1)=X(YN,K)+LX2
W'R .ABS.T(RMIN,K).G..ABS.T(YN,K+1),T'O TY23
XW=(X(YN,K)-UCW*X(RMIN,K)/UCRM+UCW*(T(RMIN,K)-T(YN,K)))/(1.-U
1CW/UCRM)
PRINT FORMAT SCHRK,X(YN,K+1),XW
W'R ((XW-X(YN,K+1))/XOW).GE..1,T'O TY23
LX2=XW-X(YN,K)
PRINT RESULTS XW
INT=2
TY23 CONTINUE

```

```

WHENEVER K.E.KMAX, TRANSFER TO TY30
W'R K.LE.11
K=K+1
R=RMIN
T'O WA12
E'L
W'R (K-(K/PRINT)*PRINT).E.0,T'O TAPE(0)
K=K+1
R=RMIN
T'O WA12
TAPE(0) CONTINUE
PT=PLT(11)-13
PL=PLT(11)-1
T'H SLIP, FOR KS=PT,1,KS.G.PL
KNXT=KS+2
THROUGH SLIP, FOR RS=0,1,RS.G.RMAX
U(RS,KS)=U(RS,KNXT)
C(RS,KS)=C(RS,KNXT)
X(RS,KS)=X(RS,KNXT)
T(RS,KS)=T(RS,KNXT)
P(RS,KS)=P(RS,KNXT)
SLIP CONTINUE
PLT(11)=PLT(11)+2
PLT(1)=28-PLT(11)
K=K+1
R=RMIN
T'O WA12
TY30 CONTINUE
TY31 CONTINUE
EXECUTE EXIT.
VECTOR VALUES PRINT=2
VECTOR VALUES READ=4
VECTOR VALUES PLT(0)=2
VECTOR VALUES POINTS=$(3(I4))$
V'S TR10=$(5(F10.4)/5(F10.4)/6(F10.4)/4(F10.4))*$
VECTOR VALUES SPACE=$(1X)$
VECTOR VALUES LOUPES=$(I3)$
VECTOR VALUES LOPRNT=$(1X,I3,20H SETS OF INPUT DATA. )$
V'S TR20=$(11H INPUT DATA/5X,3HXOW,10X,3HTFF,10X,2HM1,12X,2HM
12,11X,2HV1,11X,2HV2,11X,2HP1,11X,1HQ,12X,1HB/1X,9(1X,1PE12.5)
2/6X,2HRO,12X,9HRMAX KMAX,6X,2HE1,11X,2HE2,11X,2HE3,11X,2HE4,1
31X,2HE5,11X,2HE6/3X,1PE12.5,6X,2(1X,I4),2X,6(1PE12.5,1X)/10X,
42HS1,11X,2HS2,11X,2HS3,11X,2HS4/4X,4(1PE12.5,1X))*$
VECTOR VALUES WAVE=$(15H FOR WAVE FRONT /2X,1H0,2X,1HK,4X,6HU
1(0,K),8X,6HC(0,K),8X,6HX(0,K),8X,6HT(0,K),8X,6HP(0,K),7X,7HVN
20T(K),8X,3HUSR,11X,4HUEJR/5X,4HUJBR,10X,2HM1,12X,2HM2,12X,3HD
3UR,11X,2HER,12X,2HSR/1X/10H OTHERWISE)*$
VECTOR VALUES JOE=$(1H-,2X,1HR,2X,1HK,4X,6HU(R,K),8X,6HC(R,K)
1,8X,6HX(R,K),8X,6HT(R,K),8X,6HP(R,K),9X,3HXPP,11X,3HTPP,11X,3
2HPPP/1X,4X,3HUSR,10X,3HUSK,10X,4HUJBR,9X,4HUJBR,9X,4HUEJR,9X,

```

```

34HUEJK,9X,4HDUR1,9X,4HDUK1/9X,2HER,11X,2HSR)*$
VECTOR VALUES CHECK=$(2X,I4)$
VECTOR VALUES FORT=$(2X,2I4,8(1PE13.6,1X)/1X,6(1PE13.6,1X))*$
VECTOR VALUES SCHRK=$(1X,2(1PE13.6,1X))$
INTEGER CTT,PT,PL
DIMENSION VNOT(400)
END OF PROGRAM

```

PROVA

R

```

EXTERNAL FUNCTION (PLT,BW,QW,RW,KW,RMIN,RMAX,SW3)
ENTRY TO SENDC.

```

```

XOW=BW

```

```

SW3=0B

```

```

READ BCD TAPE 4,PTSPRT,ROW,COL,ROMX,COMX,ROMN,COMN

```

```

READ BCD TAPE 4,FLD,E1,E2,E3,E4,E5,E6,S1,S2,S3,S4

```

```

FUNCTION RETURN

```

```

ENTRY TO MARCH.

```

```

PROGRAM COMMON U,C,X,T,P

```

```

R=RW

```

```

K=KW

```

```

Q=QW

```

```

B=BW

```

```

POT(0)=PLT(0)

```

```

POT(1)=PLT(1)

```

```

POT(2)=PLT(2)

```

```

POT(3)=PLT(3)

```

```

Z=K-1

```

```

N=1

```

TY21

```

CONTINUE

```

```

DUR=0

```

```

DUK=0.

```

```

Y=R-1

```

TY1

```

C(R,K)=(C(R,Z)+C(Y,K))*0.5 +(Q-1.)*0.25*((U(R,Z)+DUR)-(U(Y,K)+D
1UK))

```

```

U(R,K)=(C(R,Z)-C(Y,K))/(Q-1.)+(U(R,Z)+DUR+U(Y,K)+DUK)*0.5

```

```

UR=(U(R,Z)+U(R,K))*0.5

```

```

UK=(U(Y,K)+U(R,K))*0.5

```

```

CR=(C(R,Z)+C(R,K))*0.5

```

```

CK=(C(Y,K)+C(R,K))*0.5

```

```

UCR=1./(UR+CR)

```

```

W'R .ABS.(UK-CK).LE..1

```

```

X(R,K)=X(Y,K)

```

```

T(R,K)=T(R,Z)+UCR*(X(R,K)-X(R,Z))

```

```

O'E

```

```

UCK=1./(UK-CK)

```

```

X(R,K)=(X(R,Z)*UCR-X(Y,K)*UCK+T(Y,K)-T(R,Z))/(UCR-UCK)

```

```

T(R,K)=(X(Y,K)-T(Y,K)/UCK-X(R,Z)+T(R,Z)/UCR)/(1./UCR-1./UCK)

```

```

E'L

```

```

XR=(X(R,K)+X(R,Z))*0.5

```

```

XK=(X(R,K)+X(Y,K))*0.5

```

```

TR=(T(R,K)+T(R,Z))*0.5
TK=(T(R,K)+T(Y,K))*0.5
V1=X(O,K)/T(O,K)
TAUR=(TR-XR/V1)*1.E06
TAUK=(TK-XK/V1)*1.E06
W'R TAUR.G.600.
TAUR=600.
E'L
W'R TAUK .G.600.
TAUK=600.
E'L
W'R XR.GE.1.28
SR=0
SK=0
O'R XR .LE..28
SR=0
SK=0
O'E
SR=S1+S2*TAUR+S3*(TAUR).P.2+S4*(TAUR).P.3
SK=S1+S2*TAUK+S3*(TAUK).P.2+S4*(TAUK).P.3
E'L
PATHP.(U,C,X,T,P,R,K,XPP,PPP,TPP)
PR=(P(R,Z)+P(R,K))*0.5
PK=(P(Y,K)+P(R,K))*0.5
EXECUTE PRSUR.(USR,USK,X,T,C,P,R,K)
W'R XR.GE..28 .AND. XR.LE..78
XER=XR-.28
O'E
XER=XR-.78
E'L
ER=E1+E2*XER+(E3*XER+E5)*TAUR+(E4*XER+E6)*(TAUR).P.2
EK=E1+E2*XEK+(E3*XEK+E5)*TAUK+(E4*XEK+E6)*(TAUK).P.2
UEJR=CR*ER*SR*(ER-UR*B)/PR
UEJK=-CK*EK*SK*(EK-UK*B)/PK
UJBR=CR*(1.-Q*UR/CR)*B*CR*SR*(ER-UR*B)/(Q*PR)
UJBK=CK*(1.+Q*UK/CK)*B*CK*SK*(EK-UK*B)/(Q*PK)
DUR1=(USR+UEJR+UJBR+UAR)*(T(R,K)-T(R,Z))
DUK1=(USK+UEJK+UJBK+UAK)*(T(R,K)-T(Y,K))
WHENEVER .ABS.(DUR1-DUR)+.ABS.(DUK1-DUK).LE.1.0,TRANSFER TO
1PR10
DUR=DUR1
DUK=DUK1
TRANSFER TO TY1
PR10 WHENEVER R.LE.ROMN .AND.K.LE.COMN,TRANSFER TO TY16
WHENEVER R.GE.ROMX,TRANSFER TO TY16
WHENEVER K .GE.COMX,TRANSFER TO TY16
WHENEVER R.E.RMIN,TRANSFER TO TY16
WHENEVER (R-(R/ROW)*ROW).E.0 .AND.(K-(K/COL)*COL).E.0
TRANSFER TO TY16
OTHERWISE

```

```

TRANSFER TO PR20
END OF CONDITIONAL
TY16  PRESS=P(R,K)/1333.
      PRP=PPP/1333.
      WRITEBCD TAPE 2,FORT,R,K,U(R,K),C(R,K),X(R,K),T(R,K),PRESS,X
PR20  1PP,TPP,PRP,USR,USK,UJBR,UJBK,UEJR,UEJK,DUR1,DUK1,ER,SR
      LAZY.(U,C,X,T,P,R,K)
      WHENEVER R.E.RMAX,TRANSFER TO PR22
      WHENEVER (X(R,K)-X(R,Z))/XOW.GE..5,TRANSFER TO TY17
      UCK=U(R,K)-C(R,K)
      UCZ=(U(R,Z)+U(R+1,Z)-C(R+1,Z)-C(R,Z))*..5
      WHENEVER UCZ.E.UCK,TRANSFER TO TY17
      TIN =(T(R,Z)*UCZ-T(R,K)*UCK+X(R,K)-X(R,Z))/(UCZ-UCK)
      WHENEVER TIN .L.T(Y,Z),TRANSFER TO TY17
      W'R (TIN-T(R+1,Z))/(T(R,Z)-T(Y,Z)).GE..2,T'0 TY17
      PRINT RESULTS TIN
      WRITE BCD TAPE 2,FORT,R,K,U(R,K),C(R,K),X(R,K),T(R,K),P(R,K),
      1X(R+1,Z),T(R+1,Z),U(R+1,Z),C(R+1,Z),P(R+1,Z),X(R,Z),T(R,Z),C(
      2R,Z),P(R,Z)
      WRITE BCD TAPE 2,FORT,R,Z-1,U(R,Z-1),C(R,Z-1),X(R,Z-1),T(R,Z-
      1),P(R,Z-1)
      T'H SLIK,FOR VALUES OF KS=K-1,K-2,K-3,K-4,K-5,K-6,K-7,K-8,K-9
      1,K-10,K-11,K-12
      KNXT=KS-1
      T'H SLIK,ROR RS=R,1,RS.G.RMAX
      U(RS,KS)=U(RS,KNXT)
      C(RS,KS)=C(RS,KNXT)
      X(RS,KS)=X(RS,KNXT)
      T(RS,KS)=T(RS,KNXT)
      P(RS,KS)=P(RS,KNXT)
SLIK  CONTINUE
      R=R+1
      T'0 TY21
TY17  W'R (X(R,K)-X(R,Z))/XOW.LE.2.,T'0 TY18
      N=N+1
      UU(N)=U(R,K)
      CC(N)=C(R,K)
      XX(N)=X(R,K)
      PP(N)=P(R,K)
      TT(N)=T(R,K)
      RR(N)=R
      U(R,K)=(U(R,Z)+U(R,K))*..5
      C(R,K)=(C(R,Z)+C(R,K))*..5
      X(R,K)=(X(R,K)+X(R,Z))*..5
      T(R,K)=(T(R,K)+T(R,Z))*..5
      P(R,K)=(P(R,K)+P(R,Z))*..5
TY18  WHENEVER T(R+1,Z).GE.T(R,K),TRANSFER TO TR175
      UCR=(U(R,Z)+U(R,K)+C(R,Z)+C(R,K))*..5
      UCR1=U(R+1,Z)+C(R+1,Z)
      WHENEVER UCR1.LE.UCR,TRANSFER TO TR175

```

```

XIN=((T(R+1,Z)-T(R,K))*UCR1*UCR-X(R+1,Z)*UCR+X(R,K)*UCR1)/(UC
1R1-UCR)
WHENEVER (XIN-X(R,K))/(X(R,K)-X(R,Z)).GE..1,TRANSFER TO TR175
PRINT RESULTS XIN
WRITE BCD TAPE 2,FORT,R,K,U(R,K),C(R,K),X(R,K),T(R,K),P(R,K)
WRITE BCD TAPE 2,FORT,R,Z,U(R,Z),C(R,Z),X(R,Z),T(R,Z),P(R,Z),
1U(R+1,Z),C(R+1,Z),X(R+1,Z),T(R+1,Z),P(R+1,Z),
2U(R+2,Z),C(R+2,Z),X(R+2,Z),T(R+2,Z),P(R+2,Z)
W'R (R+1).GE.RMAX,T'O SLID
T'H SLID,FOR RS=R+1,1,RS.G.RMAX
RNXT=RS+1
T'H SLID,FOR VALUES OF KS=K-12,K-11,K-10,K-9,K-8,K-7,K-6,K-5,
1K-4,K-3,K-2,K-1
U(RS,KS)=U(RNXT,KS)
C(RS,KS)=C(RNXT,KS)
X(RS,KS)=X(RNXT,KS)
T(RS,KS)=T(RNXT,KS)
P(RS,KS)=P(RNXT,KS)
SLID CONTINUE
RMAX=RMAX-1
YN=RMIN-1
SENDA.(0.,0.,0.,0.,0.,Q,RMAX,YN)
TRANSFER TO TY18
TR175 R=R+1
TRANSFER TO TY21
PR22 W'R N.E.1
FUNCTION RETURN
O'E
T'H SLIP,FOR VALUES OF KS=K-13,K-12,K-11,K-10,K-9,K-8,K-7,K-6
1,K-5,K-4,K-3,K-2,K-1
KNXT=KS+1
T'H SLIP,FOR RS=RR(N),1,RS.G.RMAX
U(RS,KS)=U(RS,KNXT)
C(RS,KS)=C(RS,KNXT)
X(RS,KS)=X(RS,KNXT)
T(RS,KS)=T(RS,KNXT)
P(RS,KS)=P(RS,KNXT)
SLIP CONTINUE
R=RR(N)
U(R,K)=UU(N)
C(R,K)=CC(N)
X(R,K)=XX(N)
T(R,K)=TT(N)
P(R,K)=PP(N)
N=N-1
T'O TY21
E'L
D'N UU(10),CC(10),XX(10),TT(10),PP(10),RR(10)
INTEGER N,RR,KS,KNXT,RS,YN,RNXT
INTEGER R,K,RW,KW,ROMN,COMN,ROMX,COMX,RMIN,RMAX,KMAX,Y,Z,ROW,

```

```

1COL,PLT,POT
D'N U(1202,POT),C(1202,POT),X(1202,POT),T(1202,POT),P(1202,PO
1T),POT(8)
BOOLEAN SW3
VECTOR VALUES FORT=$(2X,2I4,8(1PE13.6,1X)/1X,8(1PE13.6,1X)/6X
1,2(1PE13.6,1X))*$
V'S FLD=$(6(F10.4)/4(F10.4))*$
VECTOR VALUES PTSVRT=$(6(I4))$
END OF FUNCTION

```

GTPRKC

```

R
R THIS DECK HAS SIMPLE L AND L1 STATEMENTS AND LOOPS SEVERAL
R TIMES BEFORE EXITING WHEN CALCULATING L AND L1
R AND HAS PRESS. CONV. BY RATIO 6/10/65
EXTERNAL FUNCTION(U,C,X,T,P,RW,KW,XPP,PPP,TPP)
ENTRY TO SENDB.
B=U
Q=C
V1=X
READ BCD TAPE 4,FLD,E1,E2,E3,E4,E5,E6,S1,S2,S3,S4
PRINT RESULTS B,Q,V1
FUNCTION RETURN
ENTRY TO PATHP.
R=RW
K=KW
DPP1=0
Z=K-1
Y=R-1
CTX=1
CTT=1
UAPP=(U(Y,Z)+U(R,Z))*0.5
WHENEVER X(Y,Z).E.0..AND.X(R,Z).E.0
EMZ=0
OTHERWISE
EMZ=(U(Y,Z)+U(R,Z)-C(Y,Z)-C(R,Z))*0.5
END OF CONDITIONAL
UP=(UAPP+U(R,K))*0.5
TPP=(X(R,K)-X(Y,Z)+EMZ*T(Y,Z)-UP*T(R,K))/(EMZ-UP)
XPP=X(Y,Z)+EMZ*(TPP-T(Y,Z))
L=T(R,Z)-T(Y,Z)
L1=.ABS.(TPP-T(Y,Z))
WHENEVER CTT.G.5..AND.L1.G.L,TRANSFER TO TY5
UPP=(U(R,Z)-U(Y,Z))*L1/L+U(Y,Z)
WHENEVER .ABS.(UAPP-UPP).LE.5.,TRANSFER TO TY4
UAPP=UPP
CTT=CTT+1
TRANSFER TO TY3
TY4
WHENEVER .ABS.TPP.L..ABS.T(Y,Z),TRANSFER TO TY5
CPP=(C(R,Z)-C(Y,Z))*L1/L+C(Y,Z)
PPP=(P(R,Z)-P(Y,Z))*L1/L+P(Y,Z)

```

TY3

TY4

```

TRANSFER TO TY9
TY5  UAPP=(U(Y,Z)+U(Y,K))*0.5
      EMY=(U(Y,Z)+U(Y,K)+C(Y,Z)+C(Y,K))*0.5
TY6  UP=(UAPP+U(R,K))*0.5
      TPP=(X(R,K)-X(Y,Z)-UP*T(R,K)+EMY*T(Y,Z))/(EMY-UP)
      XPP=X(Y,Z)+EMY*(TPP-T(Y,Z))
      L=X(Y,K)-X(Y,Z)
      L1=ABS.(XPP-X(Y,Z))
      WHENEVER CTX.G.5.AND.L1.G.L
      PRINT RESULTS L1,L,XPP,TPP,X(R,K)
      EXECUTE EXIT.
      OTHERWISE
      CTX=CTX+1
      UPP=(U(Y,K)-U(Y,Z))*L1/L+U(Y,Z)
      WHENEVER ABS.(UAPP-UPP).LE.5.,TRANSFER TO TY7
      UAPP=UPP
      TRANSFER TO TY6
      END OF CONDITIONAL
TY7  CPP=(C(Y,K)-C(Y,Z))*L1/L+C(Y,Z)
      PPP=(P(Y,K)-P(Y,Z))*L1/L+P(Y,Z)
TY9  PARK=(P(Y,K)+P(R,Z))*0.5
      TR=(TPP+T(R,K))*0.5
      XR=(XPP+X(R,K))*0.5
      TAUR=(TR-XR/V1)*1.E06
      W'R TAUR.G.600.
      TAUR=600.
      END OF CONDITIONAL
      W'R XR.GE..28 .AND. XR.LE..78
      XER=XR-.28
      O'E
      XER=XR-.78
      E'L
      W'R XR.L..28
      SR=0
      ER=0.
      O'R XR.G.1.28
      SR=0
      ER=0.
      O'E
      SR=S1+S2*TAUR+S3*(TAUR).P.2+S4*(TAUR).P.3
      ER=E1+E2*XER+(E3*XER+E5)*TAUR+(E4*XER+E6)*(TAUR).P.2
      E'L
TY11 DPP=((2.*Q/(Q-1.))*C(R,K)-CPP)*(PARK+PPP)/(C(R,K)+CPP) -
1(SR*(ER-UP*B)*(ER-UP*B))*(T(R,K)-TPP)
      P(R,K)=PPP+DPP
      W'R ABS.((DPP-DPP1)/P(R,K)).LE..00005,T'0 GP10
      PARK=P(R,K)
      DPP1=DPP
      T'0 TY11
GP10 FUNCTION RETURN

```

```

INTEGER R,K,RW,KW,Y,Z
INTEGER CTT,CTX
V'S FLD=$(6(F10.4)/4(F10.4))*$
END OF FUNCTION

```

```

GTUSR      R
EXTERNAL FUNCTION (USR,USK,X,T,C,P,RW,KW)
ENTRY TO SENDA.
Q=P
RMAX=RW
YN=KW
FUNCTION RETURN
ENTRY TO PRSUR.
R=RW
K=KW
Z=K-1
W'R R.E.YN,T'O PY25
Y=R-1
LEG1=(T(Y,K)-T(Y,Z))/(T(R,Z)-T(Y,Z))
WHENEVER LEG1.GE.1, TRANSFER TO PY10
PG1=P(Y,Z)+LEG1*(P(R,Z)-P(Y,Z))
CG1=C(Y,Z)+LEG1*(C(R,Z)-C(Y,Z))
XG1=X(Y,Z)+LEG1*(X(R,Z)-X(Y,Z))
TRANSFER TO PY11
PY10      LEG1=(T(Y,K)-T(R,Z))/(T(R,K)-T(R,Z))
PG1=P(R,Z)+LEG1*(P(R,K)-P(R,Z))
CG1=C(R,Z)+LEG1*(C(R,K)-C(R,Z))
XG1=X(R,Z)+LEG1*(X(R,K)-X(R,Z))
PY11      LEG3=(T(R,K)-T(R,Z))/(T(R,K)-T(Y,K))
WHENEVER LEG3.GE.1, TRANSFER TO PY20
PG3=P(R,K)+LEG3*(P(Y,K)-P(R,K))
CG3=C(R,K)+LEG3*(C(Y,K)-C(R,K))
XG3=X(R,K)+LEG3*(X(Y,K)-X(R,K))
TRANSFER TO PY21
PY20      LEG3=(T(R,Z)-T(Y,Z))/(T(Y,K)-T(Y,Z))
PG3=P(Y,Z)+LEG3*(P(Y,K)-P(Y,Z))
CG3=C(Y,Z)+LEG3*(C(Y,K)-C(Y,Z))
XG3=X(Y,Z)+LEG3*(X(Y,K)-X(Y,Z))
PY21      CS1=.5*(CG1+C(Y,K))
PS1=.5*(PG1+P(Y,K))
CS3=.5*(CG3+C(R,Z))
PS3=.5*(PG3+P(R,Z))
DPX1=((P(Y,K)-PG1)/(X(Y,K)-XG1))*CS1*CS1/(Q*PS1)
DPX3=((PG3-P(R,Z))/(XG3-X(R,Z)))*CS3*CS3/(Q*PS3)
DCX1=((C(Y,K)-CG1)/(X(Y,K)-XG1))*2.*CS1/(Q-1.)
DCX3=((CG3-C(R,Z))/(XG3-X(R,Z)))*2.*CS3/(Q-1.)
PY25      WHENEVER R.E.RMAX.AND.T(R,Z).LE.T(Y,K)
DPX2=DPX1
DCX2=DCX1
OR WHENEVER R.E.RMAX.AND.T(R,Z).GT(Y,K)

```

```

DPX2=DPX3
DCX2=DCX3
O'R R.E.YN.AND.T(R,K).G.T(R+1,Z)
N=R+1
M=R+2
LEG=(T(R,K)-T(N,Z))/(T(M,Z)-T(N,Z))
PG2=P(N,Z)+LEG*(P(M,Z)-P(N,Z))
CG2=C(N,Z)+LEG*(C(M,Z)-C(N,Z))
XG2=X(N,Z)+LEG*(X(M,Z)-X(N,Z))
CS2=.5*(CG2+C(R,K))
PS2=.5*(PG2+P(R,K))
DPX2=((P(R,K)-PG2)/(X(R,K)-XG2))*CS2*CS2/(Q*PS2)
DCX2=((C(R,K)-CG2)/(X(R,K)-XG2))*2.*CS2/(Q-1.)
OTHERWISE
LEG2=(T(R,K)-T(R,Z))/(T(R+1,Z)-T(R,Z))
PG2=P(R,Z)+LEG2*(P(R+1,Z)-P(R,Z))
CG2=C(R,Z)+LEG2*(C(R+1,Z)-C(R,Z))
XG2=X(R,Z)+LEG2*(X(R+1,Z)-X(R,Z))
CS2=.5*(CG2+C(R,K))
PS2=.5*(PG2+P(R,K))
DPX2=((P(R,K)-PG2)/(X(R,K)-XG2))*CS2*CS2/(Q*PS2)
DCX2=((C(R,K)-CG2)/(X(R,K)-XG2))*2.*CS2/(Q-1.)
END OF CONDITIONAL
W'R R.E.YN
DPXR=DPX2
DCXR=DCX2
USR=DCXR-DPXR
FUNCTION RETURN
E'L
DPXR=.5*(DPX3+DPX2)
DPXK=.5*(DPX1+DPX2)
DCXR=.5*(DCX3+DCX2)
DCXK=.5*(DCX1+DCX2)
USR=DCXR-DPXR
USK=DCXK-DPXK
FUNCTION RETURN
INTEGER R,K,RW,KW,Y,Z,RMAX,YN
INTEGER M,N
END OF FUNCTION

```

LAZYL

R

```

EXTERNAL FUNCTION (U,C,X,T,P,RW,KW)
ENTRY TO LAZY.
R=RW
K=KW
N=1
Z=K-1
STAX(1)=0.
STAX(2)=0.125
STAX(3)=1.05

```

```

STAX(4)=1.48
THROUGH LA20, FOR N=1,1,N,G,NMAX
WHENEVER X(R,K).GE.STAX(N).AND.X(R,Z).LE.STAX(N)
RAXN=(STAX(N)-X(R,Z))/(X(R,K)-X(R,Z))
STAP(N)=(P(R,Z)+RAXN*(P(R,K)-P(R,Z)))/1333.
UP(N)=U(R,Z)+RAXN*(U(R,K)-U(R,Z))
CP(N)=C(R,Z)+RAXN*(C(R,K)-C(R,Z))
TP(N)=T(R,Z)+RAXN*(T(R,K)-T(R,Z))
WRITE BCD TAPE PRINT,GOO,R,N,STAP(N),N,TP(N),N,UP(N),N,CP(N)
END OF CONDITIONAL
CONTINUE
FUNCTION RETURN
VECTOR VALUES NMAX=4
VECTOR VALUES GOO=$5H R = 14.6H STAP(I1,4H) = 1PE13.6,
15H TP(I1,4H) = 1PE13.6,5H UP(I1,4H) = 1PE13.6,5H CP(I1,4H)
2 = 1PE13.6/1X*$
VECTOR VALUES PRINT=2
INTEGER Y,Z
INTEGER R,K,RW,KW,N
DIMENSION STAP(5),XP(5),STAX(5),TP(5),UP(5),CP(5)
END OF FUNCTION

```

LA20

APPENDIX 3

EXPERIMENTAL PROCEDURES AND DATA REDUCTION

A3.1 Experimental Procedures

Certain important experimental procedures were followed, some to insure good results and others to insure safety of equipment and experimenter.

Before beginning a series of experiments the following was done:

- 1) Pump was allowed to pump down tube for at least an hour.
- 2) Equipment was allowed to warm up at least 30 minutes.
- 3) Oscilloscopes were recalibrated. Vertical sensitivity was checked each time, sweep rates from time to time.
- 4) If magnetic field to be used, check to see that it "crowbars" at low voltage before going to higher test voltages.
- 5) The transducers were usually calibrated somewhere during the series of runs, sometimes before and after. No difference in results was noted if they had warmed up for 30 minutes to an hour prior to calibration.

During a series of runs, a good sequence of events to follow was:

- 1) Check to see that pressure in the tube was low enough.
300 microns of Hg was a good mark since the continuous purging was used.
- 2) Check all scope settings and set up trigger.
- 3) Charge up magnetic field bank, if using.
- 4) Clamp off pump filter bypass and allow some mixture to begin

purging tube. (Enough gas is needed to ensure that electric field will not break down the gas.)

- 5) Charge up electric field bank, if using.
- 6) Open shutters of camera.
- 7) Make final adjustment to desired test pressure and fire.
- 8) Close camera shutter.
- 9) Open pump filter by-pass to allow tube to pump down for next run.
- 10) Develop pictures and label them.

For the final data reported in this thesis, the pressure, electric field, current and wave speed measurements were taken simultaneously. The magnetic field was monitored from time to time to insure that it was behaving correctly. Usually its influence on the other measurements, especially the total current, were indicative of its performance.

A3.2 Data Reduction

Fig. 4-2 shows some typical oscilloscope traces representing pressure measurements made. Close examination of these traces will convince the reader that there are, indeed, differences in the pressure profile between the various cases. Before a thorough study of these results can be made, this raw data must be reduced to a form which allows comparisons to be made readily. Several steps were used by the author in reducing the data to the form presented in Chapter 5. A brief account of how this was done is presented here.

In all the experiments for which results are reported, two pressure transducers were used, one at sta (1), the other at sta (3) or sta (4). Since sta (1) is 0.28 meters upstream of the field, the wave arrives at

the beginning of the electromagnetic field about 125 μsec after crossing the transducer face at sta (1). It would take any finite disturbance generated in the field region several hundred microseconds to reach sta (1) due to the gas flow in the opposite direction. This leaves at least 400 μsec of pressure history at sta (1) which can act as a control pressure, to give an accurate measure of the detonation pressure for any given run. To be on the safe side, only the first 200 μsec were used as an indication of the pressure level.

In any set of experiments, control runs were made regularly, with one before and after each cycle of four to six experiments. In reducing this set of runs, the control runs before and after were used as a basis for comparison.

Since a difference of 1 mm of Hg in the initial pressure from one experiment to another could result in a difference of about 27 times as much in the flow field at the C-J point, with proportionately less elsewhere, this control information at sta (1) was very necessary. The reduction procedure was as follows:

- 1) The pressures at points 0, 50 μsec , 100 μsec , 200 μsec and thereafter in intervals of 100 μsec after passage of the wave front were recorded. If any noticeable deviation from the general trend was seen between these points, intermediate measurements were made as well. These measurements could be made to an accuracy of ± 1 cm of Hg using a pair of precision dividers and stepping off the measurements on the scale of the picture.

- 2) The master control at sta (1) was obtained by first averaging the point by point pressure measurement for the control run made before

and after the cycle under consideration. Due to the slight uncertainty in the initial pressure, these two runs may be in slight disagreement, but this type of discrepancy was indicated by an almost constant difference in pressure at corresponding points behind the wave. The averaging had the effect of reducing random errors incurred while taking data from the picture.

3) To determine whether runs with fields had any changes in pressure at sta (1), it was first necessary to correct for changes in initial pressure. The pressure, for the trace under consideration, at the two points, 100 μ sec and 200 μ sec behind the wave front was compared with the master control at these two points. The average deviation at these two points was then used as a correction factor for all points along this trace. Strictly speaking, some graduated scale may have been more correct, but the system used appeared to give accuracy within 1 cm of Hg which was within the limits of possible measuring accuracy anyway. This estimate is obtained by comparing runs with slightly different initial pressure and noting their point by point difference in pressure up to around 600 μ sec behind the wave front.

To illustrate error ranges to be expected as a result of this reduction, the method was applied to five control runs taken on several different days. The master control was obtained by averaging two runs from one day, and the deviations from this shown as "error flags" on Fig. A3-1. It can be seen that the error flags at sta (1) are very small except perhaps right at the wave front. The accuracy obtained within a cycle, as described previously, would be even better than shown

on this figure. Any deviations of more than two or three cm of Hg from the master control would be outside the possible error range, and was considered as a change in pressure.

To correlate results at sta (3) or (4) an additional comparison was necessary. As mentioned in Chapter 4, the point by point pressure at sta (4) (and sta (3) for that matter) was lower than at sta (1). The same procedure was used at sta (4) as at sta (3) so it will only be described once.

- 1) The point by point pressures were recorded as at sta (1). At sta (3) many intermediate points were found due to the oscillations on the signal.

- 2) The master control was again obtained by averaging measurements from the control runs at that station for the runs at the beginning and end of the cycle. This average at any point was then subtracted from the corresponding point of the master control at sta (1). Since each point on the trace at these downstream stations could possibly have been altered by the fields, the deviation of the measured pressure from the pressure at sta (1) was the critical measurement. To illustrate, let us suppose the pressure at time t_a behind the wave at sta (4) is to be compared to the control pressure at that point.

For this illustrative case, the pressure at points 100 μ sec and 200 μ sec behind the wave as measured at sta (1) is found to be Δp below the master control on the average for these two times. The pressure p_a' at sta (4) is obtained from the oscilloscope trace at time t_a . The pressure p_a , to be used in comparison with the master

control at t_a is obtained by adding the correction Δp

$$p_a = p_a' + \Delta p$$

This was done for the five control runs to illustrate possible uncertainty in measurements at each point at this station. Fig. A3-1 shows that these error flags are a little bigger than at sta (1) but are still reasonably small. Again, accuracy within a cycle was even better than shown here.

A final correction is needed before comparing results with theory. The pressure transducers measure the difference in pressure, $p_2 - p_1$, whereas theory deals with the actual pressure p_2 . This correction simply consists of adding p_1 to all the measurements made by the transducer to get p_2 .

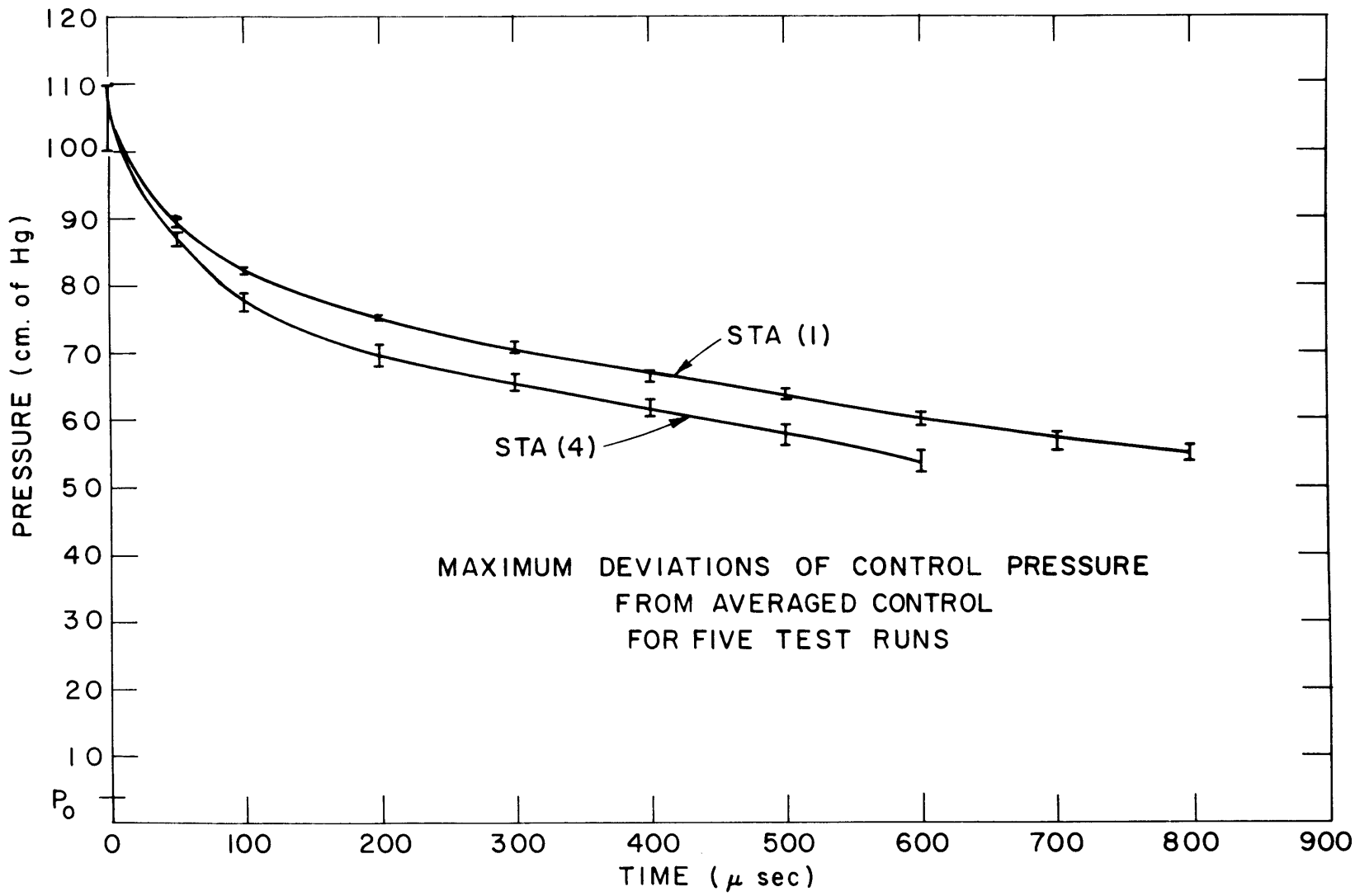


FIGURE A3-1

APPENDIX 4

COMPARISON OF PRESSURE PROFILE MEASURED IN
EXPERIMENTS WITH THEORY - NO E-M FIELDS

Results of W. E. Gordon 1 atm. initial pressure

Time μ sec	Theoretical Pressure (Atm.)	Experimental Pressure (Atm.)		
Behind wave front	P_T	P_E	$\frac{P_T - P_E}{P_T}$	$\frac{P_T - P_E}{P_E}$
0	18.6	18.2	0.0215	0.022
50	17.5	14.0	0.20	0.25
100	16.4	12.0	0.268	0.367
200	14.5	11.2	0.227	0.295
300	13.2	10.0	0.242	0.32
400	12.0	9.0	0.25	0.33
500	11.0	8.5	0.227	0.294
600	10.0	8.5	0.20	0.25

Results of the author at sta (1) in $C_2H_2 + 5/2 O_2$

40 mm Hg initial pressure

Time μ sec	p_T (cm of Hg)	p_E (cm of Hg)	$\frac{p_T - p_E}{p_T}$	$\frac{p_T - p_E}{p_E}$
0	101.8	114.	-0.120	-0.087
50	98.	91.	0.0715	0.077
100	95.	84.	0.116	0.131
200	90.	77.	0.145	0.169
300	86.	73.	0.152	0.178
400	82.	69.2	0.156	0.185
500	78.	67.5	0.135	0.155
600	74.	65.2	0.119	0.135

Results of the author at sta (4) in $C_2H_2 + 5/2 O_2$

40 mm Hg initial pressure

Time μ sec	Theoretical Pressure	Experimental Pressure		
	p_T (cm of Hg)	p_E (cm of Hg)	$\frac{p_T - p_E}{p_T}$	$\frac{p_T - p_E}{p_E}$
0	101.8	112.	-0.10	-0.091
50	99.	88.	0.111	0.125
100	97.	79.	0.185	0.228
200	92.5	71.	0.233	0.302
300	88.	67.5	0.232	0.303
400	85.	64.	0.247	0.328
500	83.	61.8	0.255	0.343
600	78.	59.1	0.242	0.32

Explanation of Results in Terms of Heat Loss

$$(dp)_{\text{path}} = \frac{k}{k-1} \frac{p}{T} (dT)_{\text{path}} - \rho \dot{q} (dt)_{\text{path}} \quad (\text{A4-1})$$

Equation A4-1 gives the pressure drop due to a temperature drop and heat loss along a path line. Following a particle of fixed identity then, the time of travel behind the wave is 180 μ sec. to come to the point which is 100 μ sec. after passage of a wave by a fixed observer. It is now of interest to compare measured heat transfer rates with what would be needed to explain the observed pressure drop near the wave front.

Heat transfer measurements by Cutting³⁷ to a thin wire suspended in the free stream of H_2-O_2 detonation waves show high rates of heat transfer. Extrapolating his results, which fall on a straight line on a log plot, to an initial pressure of .05 atm. predicts a heat transfer

rate of 2600 Btu/sec ft². Cutting's measurements were in the free stream and the author wishes to compare this with a rate of transfer to tube walls. Since the boundary layer this near the detonation wave would be relatively thin, it is not unreasonable to make such a comparison.

Since heat loss has helped establish the flow field as it is, a complete solution of the flow field would be needed to show the exact result of a given heat loss rate. An estimate can be made however, by use of equation A4-1 and by assuming a simple model. Equation A4-1 can be solved in closed form for this case if it is assumed that the internal energy of the gas, given by $C_v T$, represents the energy content of the gas. Then writing

$$\dot{q} = \frac{d}{dt} (C_v T) \quad (A4-2)$$

$$\dot{q}(dt)_{\text{path}} = d(C_v T)_{\text{path}} = C_v (dT)_{\text{path}} \quad (A4-3)$$

for C_v a constant equal to $\frac{p}{(k-1)\rho T}$. Using this in A4-3 then

$$\rho \dot{q}(dt)_{\text{path}} = \frac{1}{k-1} \frac{p}{T} (dT)_{\text{path}} \quad (A4-4)$$

Placing this in eqn. A4-1, after reduction yields

$$\left(\frac{dp}{p}\right)_{\text{path}} = \left(\frac{dT}{T}\right)_{\text{path}} \quad (A4-5)$$

The percentage temperature drop needed is directly proportional to the percentage pressure drop.

The heat transfer rate, equation A4-4, needed to account for this pressure drop is 6200 Btu/sec ft³ or only 258 Btu/sec ft² for the surface

area of the author's detonation tube. This rate is well below the rate measured by Cutting, so it is in the right range, as one would expect a lower rate of transfer to the wall. What is more, the rates measured by Cutting increased linearly with pressure on a log plot so that this effect could still be prominent at higher pressures. This would seem to qualitatively explain Gordon's results as well.

Explanation of Results in Terms of Nozzle Effect

Fay³⁸ has proposed a two-dimensional model with the boundary layer displacement effect within the reaction zone producing a uniform flow divergence throughout the detonation front. The velocity deficit calculated on the basis of this two dimensional flow agrees within a factor of two with experimentally observed deficits for the cases compared. Since a divergence of this nature behind the front would cause a decrease in pressure, the model may explain the sudden drop behind the detonation front.

Using the relation given by Fay for turbulent displacement thickness:

$$\delta^* = 0.22 l^{0.8} (\mu_e / \rho_1 v_1)^{0.2}$$

where l is distance behind wave

μ_e is viscosity of gas in combustion zone

v_1 is the detonation velocity

ρ_1 is the density upstream

a value of $\delta^* = .33$ cm is obtained after 100 μ sec from the time the wave passes a given point, for a Reynolds number/ft of 10^6 . For the author's tube, the effective area is increased by a factor of 1.26.

Using this area ratio with isentropic expansion tables⁴¹, for a value of $k = 1.4$, this would give a pressure, at 100 μsec after the wave front passes, of 0.43 the pressure at the C-J plane, or a deficit of approximately 53% below the value calculated for the simple rarefaction wave. This model therefore predicts a much greater deficit than is observed, which would indicate that the model may not be applicable in the flow field downstream of the C-J plane.

APPENDIX 5

TABULATED ELECTRIC FIELD AND CONDUCTIVITY DISTRIBUTION

Electric Field Distribution

CASE	volts/m e_1	volts/m ² e_2	volts/m ² μsec e_3	volts/m ² (μsec) ² e_4	volts/m μsec e_5	volts/m (μsec) ² e_6
I	3520	-6540	22	-.0218	-8.37	.0069
II	5727	-7600	12.15	-	-6.32	-
III	8800	-15,200	69	-.0815	-20.1	.0203
V	7070	-11,400	32	-.0227	-18	.0144
VI	9000	-9850	-1.32	.0296	-17.2	.0105

$$E(\tau, x') = e_1 + e_2 x' + e_3 \tau x' + e_4 \tau^2 x' + e_5 \tau + e_6 \tau^2$$

Electrical Conductivity

CASE	mho/m s_1	mho/m μsec s_2	mho/m(μsec) ² s_3	mho/m(μsec) ³ s_4
I	3.78	9.86×10^{-2}	$-6.26(10^{-5})$	$-5.97(10^{-9})$
II	1.63	4.51×10^{-2}	$-1.26(10^{-4})$	$1.3(10^{-7})$
III	1.113	6.60×10^{-2}	$-2.11(10^{-4})$	$2.6(10^{-7})$
V	.096	.288	$-1.13(10^{-3})$	$1.36(10^{-6})$
VI	5.53	.146	$-5.46(10^{-5})$	$-3.12(10^{-7})$

$$\sigma = s_1 + s_2 \tau + s_3 \tau^2 + s_4 \tau^3$$

Units

τ - μsec

x' - meters

σ - mho/m

E - volts/m

APPENDIX 6

ELECTROMAGNETIC SHOCK INTERACTION WITH DETONATION WAVE

A series of experiments were performed which consisted of creating a shock wave, by means of an electromagnetic interaction behind the detonation front, and observing the effect on the wave front when the shock overtook the wave. These results are reported separately since a modified theoretical model would be needed to describe the electromagnetic interactions, but are included since it acts as a useful supplement illustrating the type of effects obtainable when a regime of localized arc interaction with a magnetic field is introduced to the flow field. Once the shock wave is formed, the problem is very similar to the piston problem and could be used to further understanding of problems of that nature. The development of the shock is similar to initiation of an electromagnetic shock and could be analyzed by the same techniques. The individual parts of this picture are not new, their combination is novel.

A6.1 Apparatus and Procedure

The shock tube used for these experiments is the one described earlier with a few minor modifications, as shown in Fig. A6-1. The magnetic field coil was moved ahead to straddle the first two electrodes. Two short, 6" long, electrodes were inserted inside the main electrodes. These electrodes had an inverted V at one end projecting $3/8$ inch into the tube over the center 1 inch of the tube width. They were higher

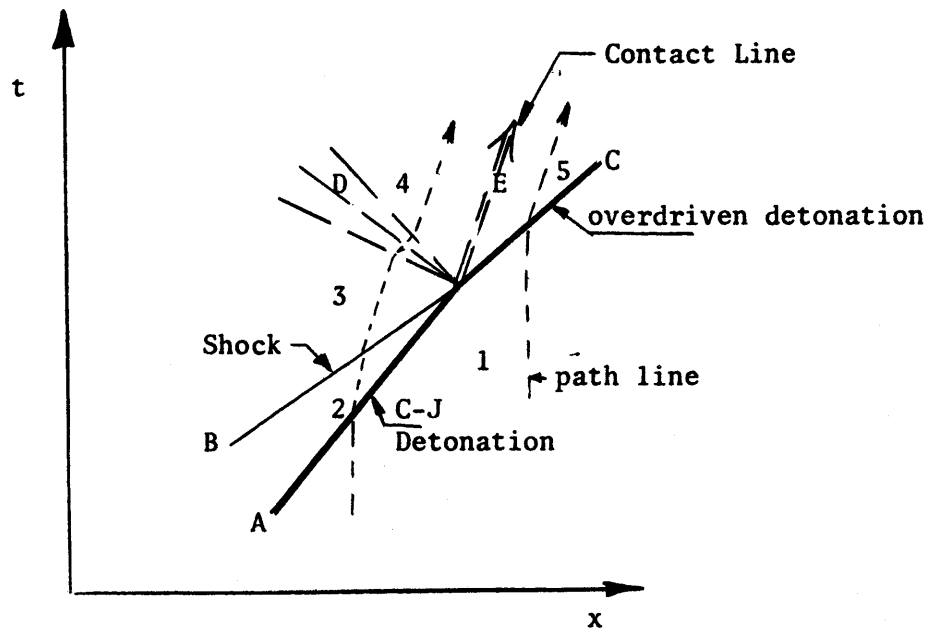
in the center of the tube than at the walls all along their length to encourage the arc to remain near the tube center to better influence the free stream. A capacitor bank was connected to these electrodes through an ignitron circuit which was triggered by a signal after the wave had passed the electrodes. The resulting discharge of current, as large as 36,000 amps, interacted with the magnetic field which was pulsed as before, and oriented to push the gas, forming a strong shock in the product gases. The single pressure transducer was placed near the beginning of the third electrode, just downstream of the magnetic field. Ion gaps connected to a circuit such as used by Knight and Duff²⁹ were spaced throughout the last meter of the test section to measure the wave speed.

Quantitative pressure measurements were not perfected to the degree of later work reported in earlier sections, when this work was done. Later additions of filters and heat shielding improved results considerably. The pressure measurements left no doubt about the presence of strong shock waves behind the front however, and velocity measurements qualitatively agreed with what one would expect as a result of one dimensional theory using the pressure data.

A6.2 Theoretical Model

The theoretical model to describe the interaction of the shock overtaking the detonation is a slight modification of shock overtaking shock as suggested by Shapiro¹⁹ (p. 1023). The accompanying schematic illustrates the model used. A C-J detonation, A, is intersected by a shock, B, resulting in an overdriven detonation C, a contact line E and

an expansion fan D. The usual jump conditions apply across the detonation with $M_2 = 1$ in region 2 but M_5 is not equal to one. The conditions in regions 4 and 5 are matched by equating particle velocity and pressure and finding the temperature difference across the contact line. From region 2 to 3, shock jump conditions hold; from 3 to 4 is an isentropic expansion. Following are tabulated results for one example worked out.



Shock Overtakes Detonation

A6.3 Sample Calculations

C-J Detonation, perfect gas model, $k = 1.4$ throughout.

$$\begin{array}{ll}
 M_1 & = 6.73 & P_1 & = .033 \text{ atm} \\
 V_1 & = 2200 \text{ m/s} & T_1 & = 298^\circ\text{K} \\
 T_2/T_1 & = 15.6 & C_1 & = 327 \text{ m/s} \\
 C_2 & = 1290 \text{ m/s} \\
 P_2 & = 0.88 \text{ atm}
 \end{array}$$

Shock B, strength $M_B = 1.5$

$$\begin{array}{ll}
 P_3/P_2 & = 2.4583 & P_3 & = 2.17 \text{ atm} \\
 u_3 & = 1804 \text{ m/s} \\
 T_3 & = 6150^\circ\text{K} \\
 c_3 & = 1480 \text{ m/s}
 \end{array}$$

Final Conditions

$$\begin{array}{ll}
 T_4 & = 6070^\circ\text{K} & T_5 & = 6470^\circ\text{K} \\
 P_4 & = 2.07 \text{ atm} & P_5 & = 2.07 \text{ atm} \\
 u_4 & = 1796 \text{ m/s} & u_5 & = 1760 \text{ m/s}
 \end{array}$$

$\xrightarrow{\text{should be same}}$

A6.4 x-t Diagram

Figure A6-2 shows an x-t plot with a C-J detonation wave and shock waves of various strength overtaking it. Each shock locus is considered individually, not showing how the detonation is modified by the interaction. The purpose of this figure is to illustrate the length of time it takes shocks of several strengths to overtake a steady state C-J detonation. No rarefaction has been considered in plotting these lines.

A rarefaction behind the detonation would weaken the shocks in time, so a shock initially at $M_1 = 2.5$ would be weaker when it intersects the detonation, and it would take it longer than 340 μsec from this starting point to overtake the detonation.

A6.5 Experimental Results

The position of the shock with respect to the wave front when the wave system passed the transducer depended on the shock strength as well as how near the front the shock was initiated. Fig. A6-3 illustrates the pressure profile for three cases. Case A is the control data with no shock following. Case B is a shock passing just 20 μsec after the detonation front. Case C illustrates an overdriven detonation which resulted from a shock overtaking it prior to reaching the transducer.

Fig. A6-4 shows the wave speed for these cases. Case A shows the trend of detonation velocity for these ion gaps. The trend is probably due to inaccurate spacing of the ion gaps rather than a changing velocity so the best comparison at any point is with the control data. Case B begins at a velocity consistent with control data in the region opposite the transducer, which is before the shock interacts with the front. A sharp rise in wave speed occurs for this case about the time one would expect the shock to overtake the wave front producing an overdriven wave. Case C is overdriven and has a correspondingly higher velocity when it enters the region of measurement. Its velocity decays slowly as one would expect of an overdriven wave.

No attempt will be made here to draw quantitative comparison between theory and experiment since these experiments do not yield sufficient

data for a rigorous comparison. This would be an interesting problem to pursue further using several transducers properly shielded against heat sensitivity and using filters on the output to clean up the signal.

A6.6 Conclusions

Qualitative results indicate that one dimensional theory can predict the wave speed changes brought about by shocks overtaking detonations. Further, from observing case B, one can deduce that the shock only changes the wave speed when it actually overtakes the wave or crosses the C-J plane, as one would expect from the Chapman-Jouguet hypothesis.

The observations made, that the one dimensional theory is qualitatively correct for these large changes in wave speed and pressure, support the main thesis. There the changes at the wave front were too small to measure, but were not inconsistent with theory. Here the speed change was detected and qualitatively, at least, agreed with the same theory used to calculate wave speed changes.

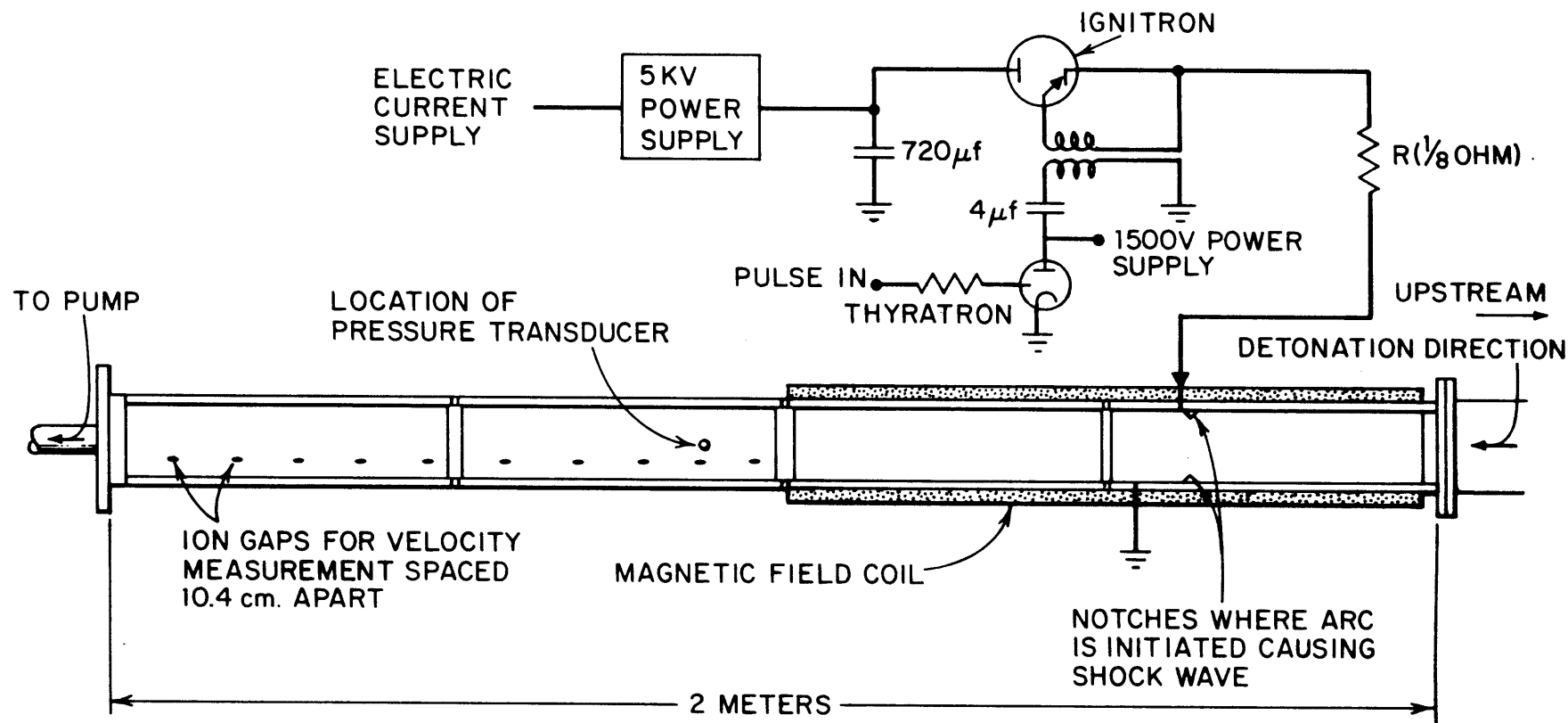


FIGURE A6-1 SCHEMATIC OF TEST SECTION USED TO GENERATE SHOCK WAVES BEHIND DETONATION WAVES.

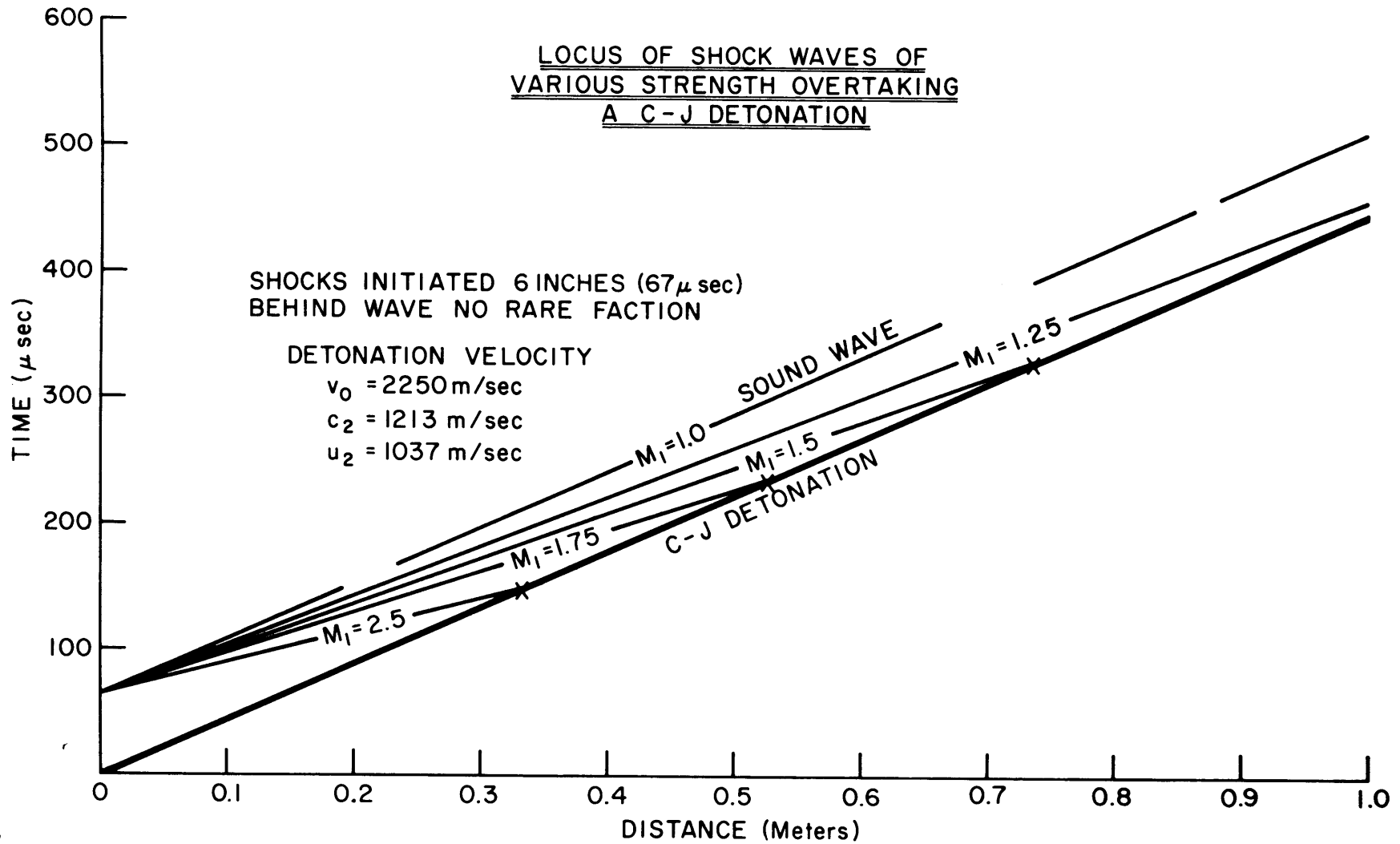


FIGURE A6-2

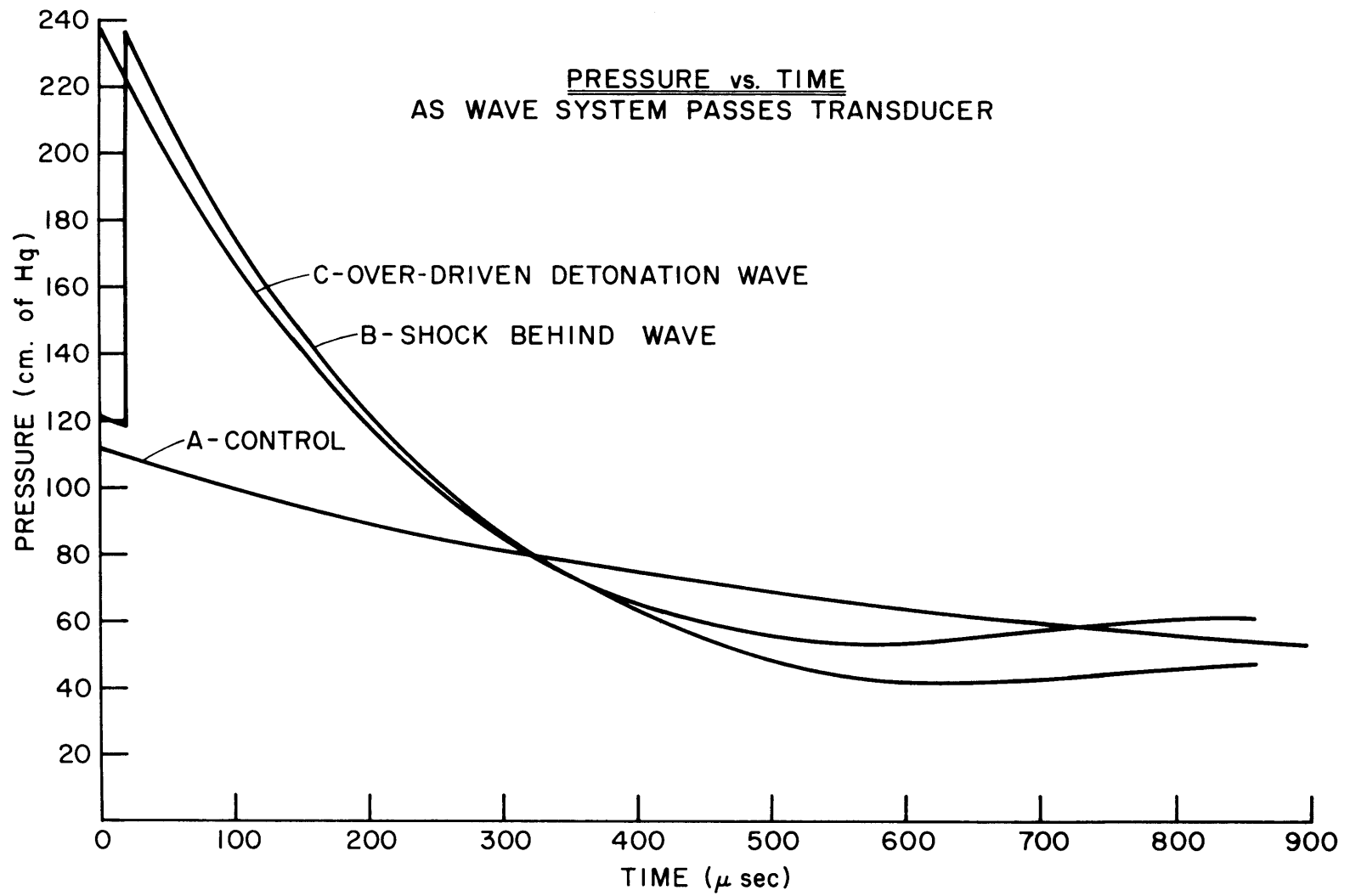


FIGURE A6-3

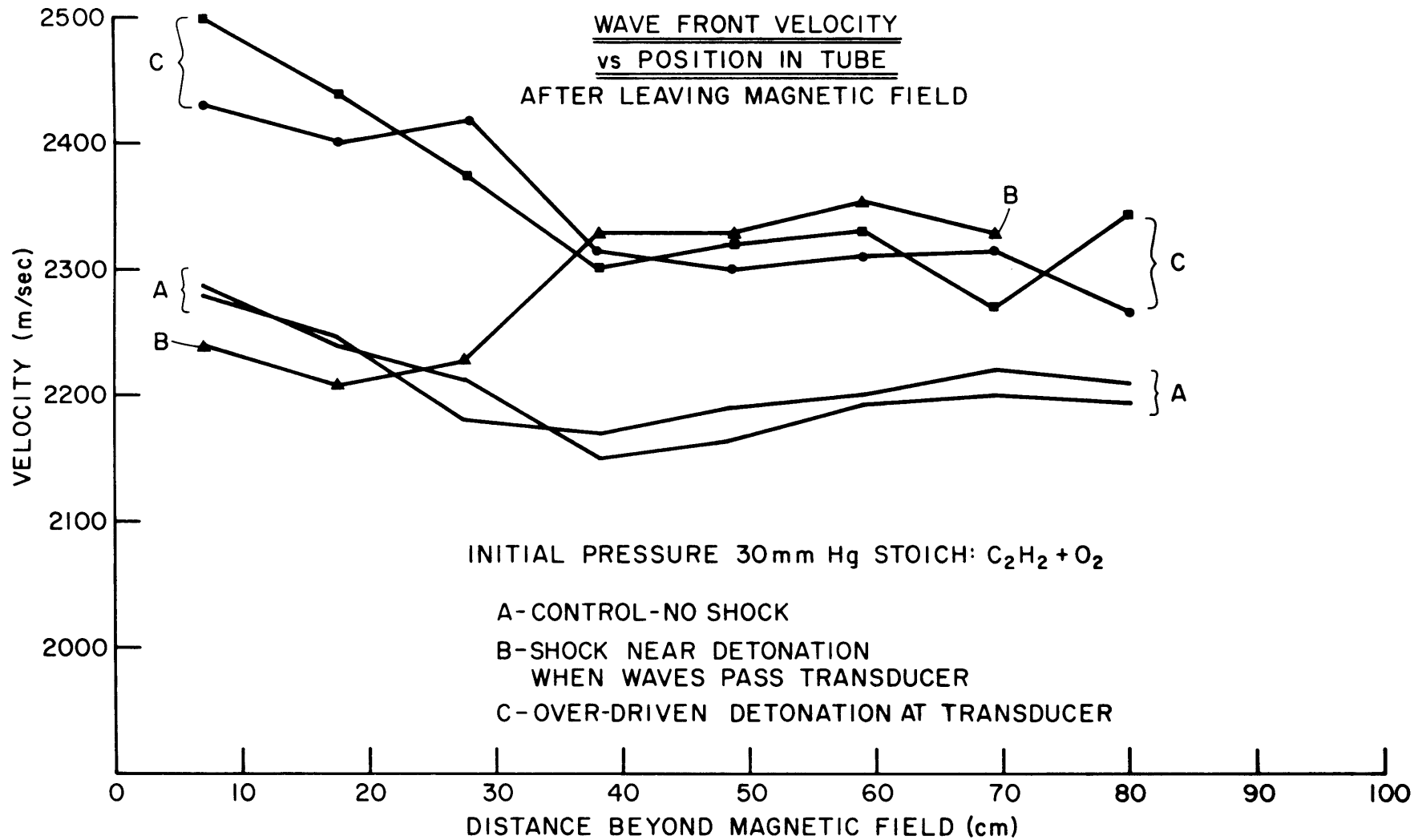


FIGURE A6-4

APPENDIX 7

ENERGY LOSS IN THE PLASMA

The problem of evaluating possible heat loss for the conditions of the experiments described in this thesis is not a simple one. Some of the mechanisms which may be involved are:

- a) convective-conduction losses in a turbulent boundary layer
- b) radiative losses (black body type)
- c) recombination at the cold wall
- d) Bremsstrahlung

a) Convection-conduction:

Heat transfer in fully developed turbulent flow can be treated reliably by empirical or semiempirical relations obtained by correlating heat transfer data taken for the type of situations under study.⁴² The problem here is one concerning heat transfer to a tube wall from detonation products which are "contaminated" by potassium chloride. The flow field is nonsteady and being acted upon by electromagnetic fields. The heat transfer rate of such a system has not, to the authors knowledge, been measured.

A simple-minded model could be useful in gaining insight into the situation, however. Fig. A7-1a shows the growth rate of the turbulent boundary layer behind the detonation wave as given by Fay.³⁸ This boundary layer will build up on all four walls, so the free stream area is rapidly reduced, as shown in Fig. A7-1b. At a point 200 μ sec behind the wave, 40% of the electromagnetic interaction would take place in

the boundary layer where gradients in temperature as well as turbulence would allow heat transfer to the wall to dissipate much of the added energy. After 600 μsec , 80% of the tube cross-section is in the boundary layer.

Fig. A7-1c shows the radial temperature distribution for turbulent flow in a tube for Prandtl number unity. This type of temperature distribution may be expected in the boundary layer of the shock tube. Qualitatively it seems obvious that the heat transfer rate to the wall will increase as the gas temperature rises. Whether this can account for the apparent heat loss in the experiments would take careful analytical or experimental work, or both.

b) Radiation:

Radiation of the type associated with black bodies can account for large rates of energy transfer. A few simplified calculations may illustrate this point.

A measure of the flow energy at the C-J plane can be evaluated from

$$\rho C_p T \sim 5 \times 10^5 \text{ watt sec/m}^3$$

Since there is energy associated with the $\rho \frac{u^2}{2}$ term, the total energy may be of the order of $10^6 \text{ watt sec/m}^3$. The rate of loss by black body radiation is given by

$$S_B = a T^4$$

where $a = 5.67 \times 10^{-8} \text{ watt/m}^2 \text{ } ^\circ\text{K}^4$

If the effective mean temperature of the products is 3000°K over the first 1000 μsec , and the gas was losing energy by black body radiation

at all surfaces, for the author's tube, 3.6×10^5 watt sec/m³ would be lost during this 1000 μ sec. This estimate of energy loss is about 30% above what was needed in Chapter 4 to explain the pressure drop below normal. (The gas is therefore probably not a black body.)

Now suppose the electromagnetic effects raise the temperature slightly, so that the new temperature is $(1+m) T$. The black body radiation is now

$$S_B = a(T(1+m))^4$$

and the additional radiation, above what it was for the "no fields" case would be

$$\Delta S_B = a((T(1+m))^4 - T^4) \sim 4 a m T^3$$

For a fractional increase in temperature of 0.0166, which corresponds to 50°K for $T = 3000^\circ\text{K}$, this additional radiation loss in a tube with the geometry as used here amounts to 2.45×10^7 watt/m³. The rate of electrical energy addition is about 5×10^7 watt/m³. Noting that the excess loss rate is directly proportional to the fractional increase in temperature, m , it appears as though this mechanism could easily dissipate the added energy with a small increase in temperature even if it was not quite as good a radiator as a black body. An increase in temperature of 50°K corresponds to an increase in sound speed of only about 10 m/sec. All the cases reported in Chapter 5 which retained the $\overline{\mathbf{E} \cdot \mathbf{j}}$ term had increases of sound speed much greater than 10 m/sec, so the numbers used here are realistic.

The one condition upon which this argument rests is that the gas surface acts as a black body, a condition which may not be realized.

Rose and Clark⁴³ (p 229) assert that a "plasma appears as a black body at low frequency". Whether or not this argument can apply here has not been ascertained by the author.

Even if the plasma does act as a black body, some mechanism must exist to cause the effects of heat loss at the boundary to be felt throughout the flow. Usual boundary layer concepts involving temperature gradients and radiative thermal conductivity⁴⁴ may provide the needed mechanism. Rarefactions originating at tube walls and propagating across the tube may assist in equalizing effects.

Rohsenow⁴² states (p 333) that "the part of the radiant energy which is absorbed or emitted by materials which are electric conductors is all completely absorbed or emitted in a layer of approximately 0.00005 in. below the surface. In electric nonconductors this layer is of the order of 0.05 in. thick."

The side walls of the author's tube are made of plexiglass, which would presumably not get as warm at the surface as a conductor would, since its absorption layer is thicker. Since the absorbtivity is high the reflectivity would be low (since it could be considered opaque). Perhaps the side walls could also approximate a black body which absorbs all the radiation incident upon it. The electrodes had a layer of oxide as well as KCl, so they too would be relatively good absorbers of radiation.

c) Recombination at the cold wall:

The heat transfer measurements made by Cutting³⁷ in the flow field of H_2-O_2 detonations correlated closely with estimates of heat exchange due to recombination of the dissociated gases coming in contact with the

wire. But the dominant mechanism of heat exchange at the wall may be altered by the thick, turbulent boundary layer. It is possible that dissociated products would diffuse to the cooler region of the boundary layer and recombine before reaching the wall. Some other mechanism may be required to transport the recombination energy to the wall. Further study of this mechanism would be required to determine if it would to any degree account for the additional losses which apparently dissipate much of the electrical energy added.

d) Bremsstrahlung:

This form of radiation is closely related to the degree of ionization so deserves consideration as the mechanism of additional loss. The relation predicting rates of loss⁴³ by Bremsstrahlung is

$$w = \sqrt{\frac{3}{2}} \frac{q_i^2 q_e^4 n_i n_e}{24\pi\epsilon_0^3 c^3 m_e h} \sqrt{\frac{8K_B T_e}{\pi m_e}} \quad \text{watts/m}^3$$

where the symbols are defined in the usual way.

For a singly ionized plasma, $q_i = q_e$ and $n_i = n_e$. This can be simplified to give

$$w = 1.49 \times 10^{-49} n_e^2 \sqrt{T_e} \quad \text{watts/m}^3$$

Some numerical examples can give a better indication of the magnitude of this effect.

i) $n_0 = 2 \times 10^{24} / \text{m}^3$

1% ionization — $n_e = 2 \times 10^{22} / \text{m}^3$

$T_e \sim 3600^\circ\text{K}$

$$w = 3.58 \times 10^7 \text{ watt/m}^3$$

For these same conditions and a collision cross-section of $2.5 \times 10^{-15} \text{ cm}^2$, this degree of ionization corresponds to an electrical conductivity of $\sim 2560 \text{ mho/m}$ which is several orders of magnitude larger than obtained in experiments.

$$\text{ii) } n_0 = 2 \times 10^{24} / \text{m}^3$$

$$.1\% \text{ ionization} - n_e = 2 \times 10^{21} / \text{m}^3$$

$$T_e \sim 3600^\circ\text{K}$$

$$w = 3.58 \times 10^5 \text{ watt/m}^3$$

equivalent $\sigma \sim 256 \text{ mho/m}$

$$\text{iii) } n_0 = 2 \times 10^{24} / \text{m}^3$$

$$.01\% \text{ ionization} - n_e = 2 \times 10^{20} / \text{m}^3$$

$$T_e \sim 3600^\circ\text{K}$$

$$w = 3.58 \times 10^3 \text{ watt/m}^3$$

equivalent $\sigma \sim 25.6 \text{ mho/m}$

The first example has a dissipation rate approximately equivalent to the rate of energy input, but the electrical conductivity in experiments is much lower than that corresponding to 1% ionization. The third example has a conductivity level which corresponds more closely with experiments, but now the energy dissipation rate is much lower than the rate of electrical energy addition. It can be concluded that Bremsstrahlung do not account for the apparent loss of energy experienced in experiments.

With the information now available, it is difficult to assess which mechanism, if any, of the ones considered here is actually responsible

for the loss of the electrical energy contributed by the electric fields. Boundary layer effects most certainly will be an important factor but whether convection-conduction, radiation, recombination or a combination of these are important would have to be verified by more careful experimental and theoretical study.

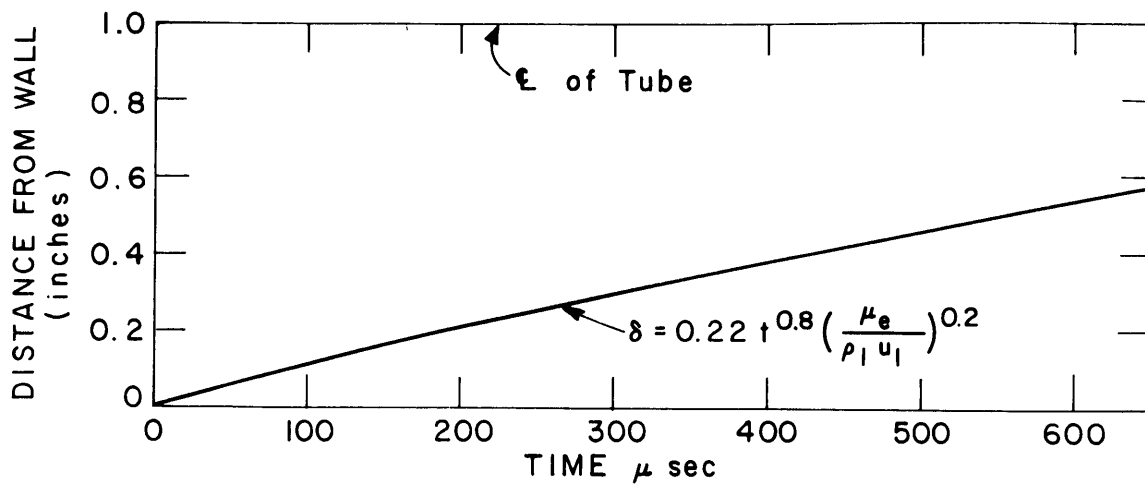


FIGURE A7-1a BOUNDARY LAYER GROWTH BEHIND DETONATION

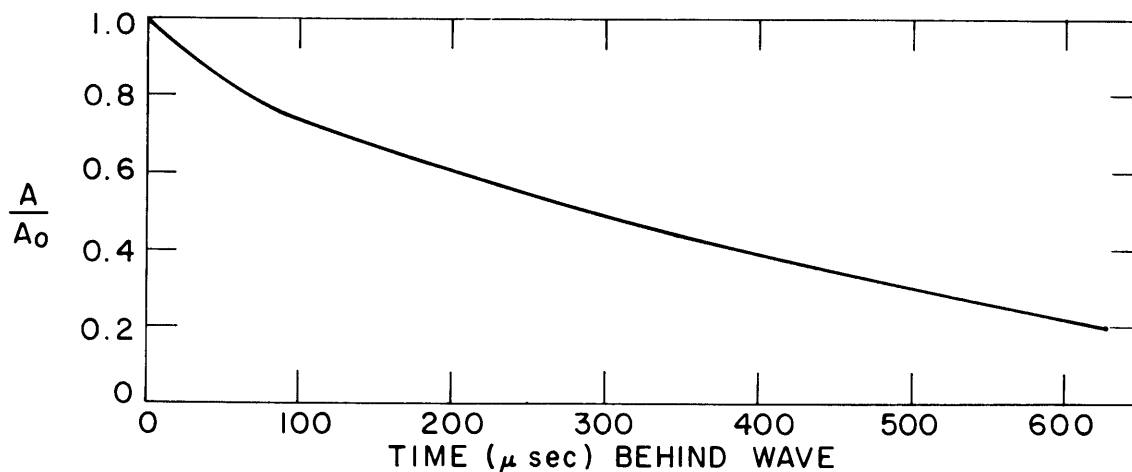


FIGURE A7-1b FREE-STREAM AREA AS A FRACTION OF TUBE AREA

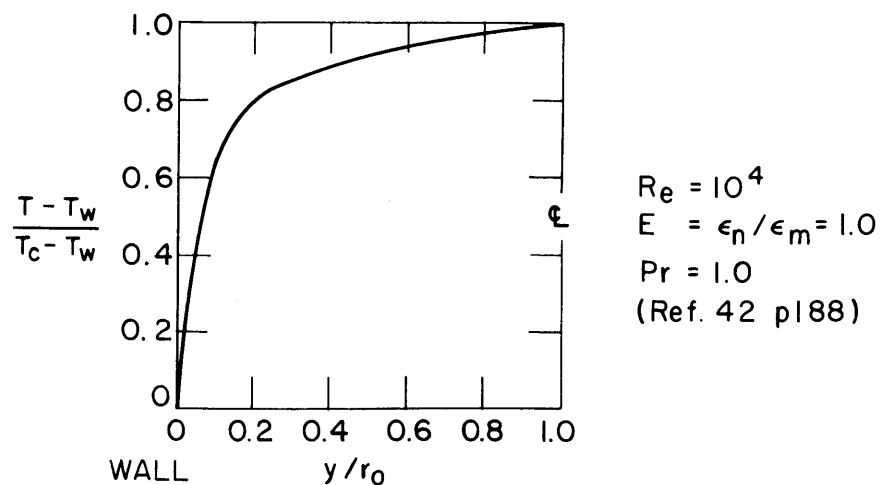


FIGURE A7-1c TEMPERATURE DISTRIBUTION FOR TURBULENT FULLY DEVELOPED PIPE FLOW

REFERENCES

1. Lewis, B. and von Elbe, G., "Combustion, Flames and Explosion of Gases", 2nd Ed., Academic Press, 1961.
2. Courant, R. and Friedrichs, K.O., "Supersonic Flow and Shock Waves," Interscience Publ., N.Y. 1948.
3. Helliwell, J. B., "Gas-ionizing Shock and Combustion Waves in Magnetogasdynamics", J. Fl. M. v. 14, p. 405, 1962.
4. Helliwell, J. B., "Magnetogasdynamic Deflagration and Detonation Waves with Ionization", J. Fl. M., v. 16, p. 243, 1963.
5. Larish, E., and Shekhtman, I., "Propagation of Detonation Waves in the Presence of a Magnetic Field", Soviet Phys. Jetp, (8), pp 139-143 1959.
6. Lyubimov, G. A., "The Effect of an Electromagnetic Field on the Detonation Regime," Soviet Physics, Doklady, vol 4, 1960, pp 526-528.
7. Kemp, N. H., and Petschek, H. E., "Theory of the Flow in Magnetic Annular Shock Tubes", Phy Fl 2, p 599 (1959).
8. Patrick, R. M., "High Speed Shock Waves in Magnetic Annular Shock Tube", Phy. Fl. 2, 589 (1959)
9. Plett, E., "Electro-magnetic Effects in Detonation Waves", S.M. Thesis, M.E. Dept., M.I.T., 1964.
10. Kelly, J. R., "Electromagnetic Effects on the Propagation and Structure of Gaseous Detonations," Sc.D. Thesis, M.E. Dept. M.I.T. 1965.
11. Taylor, G. I., "The Dynamics of the Combustion Products Behind Plane and Spherical Detonation Fronts in Explosives", Proc. Roy. Soc. (London) A200, 234 (1950).
12. Kistiakowsky, G. B., and Kydd, P. H., "Gaseous Detonations. VI The Rarefaction Wave," J. Chem. Phys. v 23, no 2, 1955.
13. Gordon, W. E., "Pressure Measurements in Gaseous Detonation by Means of Piezoelectric Gages", Third Symposium on Combustion and Flame and Explosion Phenomena, p 579, Williams and Wilkins (Baltimore) (1949).
14. Edwards, D. H., Williams, G. T., and Breeze, J. C., "Pressure and Velocity Measurements on Detonation Waves in Hydrogen-Oxygen Mixtures", J. Fl. M. v 6, p 497 (1959)

15. Toong, T. Y., "Ionization in Gaseous Detonation Waves", Progr. in Astro. and Aero., AIAA, vol 12, Ionization in High Temperature Gases, pp 285-298, 1963.
16. Basu, S., and Fay, J. A., "Ionization in Detonation Waves", Seventh Symposium (Int.) on Combustion, Butterworths Sci. Publ., London, pp 277-282, 1959.
17. Basu, S., "Ionization in Seeded Detonation Waves", Phys. Fl. v 3, 1960, pp 456-463.
18. Chinitz, W., Eisen, C. L., and Gross, R. A., "Aerothermodynamic and Electrical Properties of Some Gas Mixtures to Mach 20", A.R.S. Journal, vol 29, pp 573-579, 1959.
19. Shapiro, A. H., "The Dynamics and Thermodynamics of Compressible Fluid Flow," Vol II, Ronald Press, New York, 1954.
20. Whitman, G. B., "On the Propagation of Shock Waves through Regions of Non-Uniform Area or Flow", J. Fl. M. v 4, p 337, 1958.
21. Rosciszewski, J., "Calculations of the Motion of Non-Uniform Shock Waves", J. Fl. M., v 8, p 337, (1960).
22. Rosciszewski, J. and Oppenheim, A. K., "Shock Interaction with an Electromagnetic Field", Phys. Fl., v 6, p 689, (1963).
23. Mirels, H., and Braun, W. H., "Perturbed One-Dimensional Unsteady Flows Including Transverse Magnetic Field Effects", Phy. Fl., v 5, p 259, (1962).
24. Wilson, G. L., "Magnetic Reflection of a Shock-Produced Plasma", S.B. Thesis, E.E. Dept., M.I.T., 1961.
25. Thomas, R. H., "Crowbar Timing Circuit", Project done for G. L. Wilson, E.E. Dept., M.I.T., January 1965.
26. Silverstein, R. L., "Design of a Schlieren System for the Examination of Detonation Waves in Electric and Magnetic Fields," S.B. Thesis, Dept. of Aero/Astro., M.I.T., 1965.
27. Cobine, J.D., "Gaseous Conductors Theory and Engineering Applications," 1st Ed., McGraw Hill, p 134 ff, (1941).
28. Durgin, F., M.I.T. (DSR staff) Private Communication.
29. Knight, H. T., and Duff, R. E., "Precision Measurements of Detonation and Strong Shock Velocities in Gases", Rev. Sci. Instr., Vol 26, p. 257, 1957.

30. Louis, J. F., "An Alkali Metal Vapor Shock Tube and the Measurements of the Conductivity and Electron Concentrations of Cesium in Argon", Avco-Everett Research Lab., Research Note 567, July 1965.
31. Toong, T. Y., numerous private communications.
32. Barak, E., private communications.
33. Lee, J. H., "The Propagation of Shocks and Blast Waves in a Detonating Gas", McGill University, Gasdynamics Research Lab. Rept. 65-1, March 1965.
34. Berets, D. J., Greene, E. F., and Kistiakowsky, G. B., "Gaseous Detonations. I Stationary Waves in Hydrogen-Oxygen Mixtures", Amer. Chem. Soc. J. 72, p 1080, 1950.
35. Edwards, D. H., and Williams, G. T., "Effect of Tube Diameter on the Pressures in Gaseous Detonation Waves", Nature, v 180, p 1117, Nov. 1957.
36. Wolfson, B. T., "The Effect of Additives on the Mechanism of Detonation in Gaseous Systems", Ph.D. Thesis, Ohio State Univ. 1963.
37. Cutting, J. C., "Heat Transfer in Dissociated Combustion Gases", M.S. Thesis, M.E. Dept. M.I.T., 1960.
38. Fay, J. A., "Two-Dimensional Gaseous Detonations: Velocity Deficit", Phy. of Fl., v 2, p 283, 1959.
39. von Engel, A., "Ionized Gases", 2nd Edition, Clarendon Press, 1965.
40. Turcotte, D. L. and Friedman, W., "Electrode Interactions in Seeded Combustion Products", Tenth Symposium (Int.) on Combustion, pp 673-683, 1965.
41. Shapiro, A. H., "The Dynamics and Thermodynamics of Compressible Fluid Flow", Vol. 1, Ronald Press, New York, 1953.
42. Rohsenow, W. M. and Choi, H. Y., "Heat, Mass, and Momentum Transfer", Prentice-Hall, N.J., 1961, Chap. 8.
43. Rose, D. J., and Clark, M. C. Jr., "Plasmas and Controlled Fusion", M.I.T. Press, Cambridge, Mass., 1961.
44. Fay, J. A., "Energy Transfer in a Dense Plasma", Fluid Mech. Lab. Publ. No. 63-1, M.E. Dept. M.I.T., 1963.

NOMENCLATURE

A_o	- tube area (eqn. 2.1)
A/A_o	- ratio of free stream area to tube area (Fig. A7-1b)
a	- defined in Appendix 7
B, \vec{B}	- scalar and vector magnetic field
C_p	- specific heat at constant pressure
C_v	- specific heat at constant volume
c	- sound speed in gas = $\sqrt{k RT}$
C-J	- of or pertaining to the Chapman-Jouguet criteria which determines the steady state detonation wave speed
E, \vec{E}	- scalar and vector electric fields
F	- friction term in momentum eqn. (2.2)
$f_i (V)$	- voltage drop across the two outer probes of electric field probes at point (i) along the electrode
$f_{ii} (V)$	- as f_i but at point (ii) along the electrode
h	- Planck's constant
j, \vec{j}	- scalar and vector electric current density
K_B	- Boltzmann constant
k	- C_p/C_v - ratio of specific heats
L	- characteristic length (section 2.4 and App. 1)
$M_{(1),(2)}$	- Mach number used in co-ordinate system attached to wave front
M	- defined in section 2.5
m	- fractional increase in temperature used in App. 7
m_e	- electron mass
N	- defined in section 2.5

n_o, n_i, n_e	- number density of neutrals, ions and electrons
p	- static pressure in gas
$Q/C_p T_1$	- non-dimensional stagnation enthalpy addition in wave front
q_i, q_e	- charge on ions and electrons
R_o	- distance of wave front from ignition point
Re	- Reynolds number ($\rho u L / \mu$)
Rm	- Magnetic Reynolds number (App. 1)
r	- distance of observer from ignition point
S_B	- radiant energy transfer rate (App. 7)
T	- static temperature of gas
T_e	- electron temperature
T_w	- wall temperature of tube (Fig. A7-1c)
T_c	- temperature at center of tube (Fig. A7-1c)
t	- time measured relative to origin at sta (1)
u	- particle velocity in laboratory co-ordinates
V_{NOT}, V_1, V_o	- detonation wave front speed
V	- particle velocity in co-ordinates attached to wave front
w	- energy density of Bremsstrahlung radiation
x, y, z	- three co-ordinate directions (Fig. 2-1a)
y/r_o	- fractional distance from center of tube (Fig. A7-1c)
α	- fraction ionized
δ	- boundary layer thickness
δ^+	- boundary layer displacement thickness
ϵ_o	- permittivity of free space

- ϵ_h, ϵ_m - eddy diffusivity pertaining to enthalpy and mass
 e - base of natural logarithm
 μ_e - coefficient of viscosity at free stream conditions
 μ_o - (4×10^{-7}) magnetic permeability
 ρ - gas density
 σ - electrical conductivity of gas
 τ - time with respect to the wave front
 $\tau = t - x V_{NOT}$ for constant V_{NOT} at position (x,t)

Subscripts

- 1 - pertaining to conditions upstream of wave front
 2 - pertaining to conditions at the hot boundary of the wave front
 I - pertaining to changes along the type I characteristic
 II - pertaining to changes along the type II characteristic
 path - pertaining to changes following a fluid particle on its path line
 i - pertaining to the position of the first point along the electrode at which electric field measurements are made
 ii - pertaining to the second point of electric field measurements

Other subscripts used in Chapter 2 may be identified from Fig. 2-1.

BIOGRAPHICAL SKETCH

Edelbert Gregory Plett was born in Bassano, Alberta, Canada, on January 17, 1939. He moved to Chilliwack, British Columbia with his family in 1945, where he then received his primary and secondary education. After receiving a B.A.Sc. degree in Mechanical Engineering from the University of British Columbia in 1962, he entered M.I.T., where he received an S.M. degree in Mechanical Engineering in 1964.

He has been a Research Assistant in the Mechanical Engineering Department since entering M.I.T. in 1962. He was the recipient of the M.I.T. Canadian Alumni Scholarship for the academic year 1963-64 and again in 1964-65.